# Event Classification at HERA and The Development of the Resistive Plate Chamber for LHC

Alison E. Wright

December 1994

A thesis submitted to the University of Manchester for the degree of Doctor of Philosophy in the Department of Physics in the Faculty of Science.

# Event Classification at HERA
# and
# The Development of the Resistive Plate Chamber for LHC

Alison E. Wright

December 1994

A thesis submitted to the University of Manchester for the degree of Doctor of Philosophy in the Department of Physics in the Faculty of Science.

# Contents

## Abstract

A method of event classification for the H1 experiment at HERA (Hamburg) is presented. From Monte Carlo studies, a set of variables are chosen such that the moments of their distributions offer good discrimination between physics processes. The data are fitted to this information, to calculate what fraction of the sample is due to a particular interaction. The method is used here for the separation of charged current interactions from the deep inelastic scattering sample of the H1 experiment.

A preliminary study of the Resistive Plate Chamber is also presented: this muon detector offers excellent time resolution ($\sim 1ns$) and is intended as a trigger for the experiments at CERN's Large Hadron Collider.

No portion of the work referred to in this thesis has been submitted in support of an application for another degree or qualification of this or any other institute of learning.



This work was supported financially by the Science and Engineering Research Council (S.E.R.C.), latterly the Particle Physics and Astronomy Research Council (P.P.A.R.C.) between October 1991 and October 1994.

# Introduction

HERA, the first high energy electron-proton collider, came into operation at the DESY laboratory (Hamburg, Germany) in May 1992. The machine accelerates electrons and protons to $30\,GeV$ and $820\,GeV$ respectively, and the subsequent collisions at $314\,GeV$ centre of mass energy allow the study of proton structure in an entirely new kinematic region: the possible range of the four-momentum transfer squared ($Q^2$) between electron and proton reaches $10^5\,GeV^2$, whereas proton constituents with a momentum fraction as small as $10^{-5}$ may be probed. This is a considerable extension of the kinematic range accessible to earlier fixed target experiments (typically $Q^2 < 10^2\,GeV^2$ and momentum fractions $> 10^{-2}$). In particular, the wide $Q^2$ range at HERA allows precision tests of perturbative Quantum Chromodynamics; but, as ever smaller proton momentum fractions are probed, soft physics processes not described by perturbation theory become more important: this transition to the non-perturbative region is, at present, poorly understood.

The HERA ring is of $6.3\,km$ circumference. Protons, then electrons are injected and accelerated in bunch formation, before being brought to collision at four points in the ring [1]. The detectors H1 and ZEUS [2] are in two of these interaction regions (North and South respectively), and a third experiment, HERMES [3], has recently been commissioned in the East area for the study of polarised structure functions.

The HERA machine has a design luminosity of $1.5 \times 10^{31}\,cm^{-2}s^{-1}$, giving an annual integrated luminosity of $100\,pb^{-1}$. H1 began taking data in 1992, and of the $32\,nb^{-1}$ delivered by HERA, $25\,nb^{-1}$ were collected for physics analysis. In 1993, with more colliding bunches and higher currents, instantaneous luminosities of $10^{30}\,cm^{-2}s^{-1}$ were achieved, and $500\,nb^{-1}$ of useful data were collected by H1.

For the data-taking periods of 1992 and 1993, while the proton beam operated at its design value of $820\,GeV$, the electron beam reached $26.7\,GeV$. For 1994 the electron energy is $27.52\,GeV$, approaching design value and optimising polarisation.

A great variety of physics processes may be observed at H1, as a wide kinematic range is available and the nature of the particles entering the scattering process from either the electron or the proton side can vary. It is then important to be able to recognise an event as the result of a particular type of interaction, *ie.* to *classify* the event. An analytic method for the determination of the fraction of events of a given process is presented here. In particular, the charged current interaction has been studied.

A review of particle physics at HERA is presented in chapter 1 of this thesis, while chapter 2 covers the experimental details of the H1 detector. In chapter 3 the method for event classification is introduced and then its application to the separation of the charged current process is discussed in chapters 4 and 5.

Chapter 6 gives a brief account of some early development work performed by the author on the Resistive Plate Chamber (RPC), a muon detector with very fast time resolution that is favoured as a triggering device for the Large Hadron Collider (LHC), the next major accelerator experiment planned at CERN.

# Chapter 1

# Physics at HERA

The current understanding of particles and their interactions is embodied in the Standard Model of particle physics. This is a renormalisable gauge theory with a broken $SU(2) \times U(1)$ symmetry describing electromagnetic and weak interactions (Electroweak theory) and an $SU(3)$ symmetry describing strong interactions (Quantum Chromodynamics or QCD) [4]. Electroweak theory has been extensively tested in the last few years, particular successes being the discovery of the $W$ and $Z$ bosons [5], the mediators of weak interactions whose existence was predicted by the theory. Many predictions of QCD remain to be tested at HERA.

QCD describes the strong interactions of particles via the exchange of gluons, which couple to themselves and to quarks. The coupling strength, $\alpha_s$, however has no single value but is a function of the distance scale in the process: $\alpha_s$ is large for long range interactions, but small at small distances. This gives rise to two important properties of QCD, asymptotic freedom and confinement.

A typical electron–proton scattering process is shown in figure 1.1: the incoming electron emits a boson of sufficient virtuality (*ie.* $Q^2 > 1\,GeV^2$) to probe the internal structure of the proton. Asymptotic freedom means that for such an interaction $\alpha_s$ is very small – the coupling between the quarks and gluons inside the proton is very weak and they can be considered as effectively free "partons". The scattering process can then be modelled as a boson-parton interaction, and very precise calculations can be made in terms of a perturbative expansion in $\alpha_s$. Hence this is the region of perturbative QCD [6].

Conversely, for $Q^2 \ll 1\,GeV^2$, the boson probe cannot resolve the proton structure: the coupling between quarks and gluons is so strong that they can no longer be

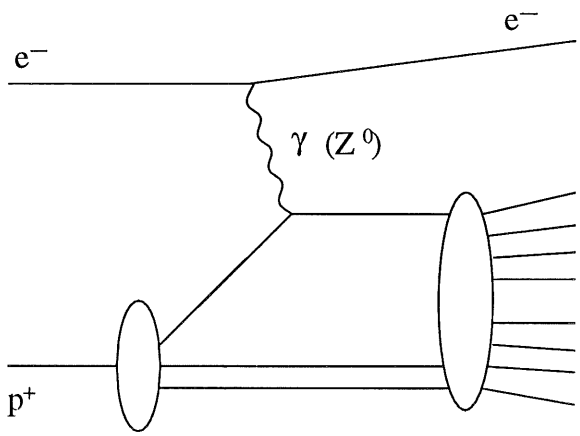


Figure 1.1: The neutral current process.

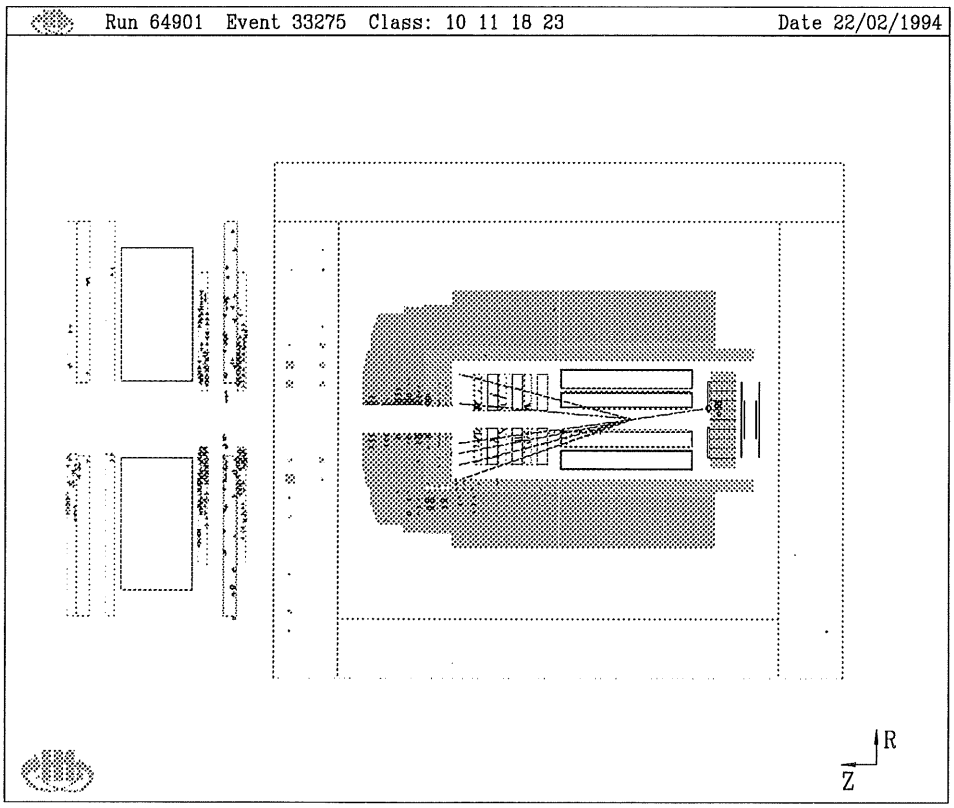


Figure 1.2: Deep inelastic scattering event (neutral current) seen in the H1 detector.

considered as individual partons – this is confinement. Perturbative expansions in $\alpha_s$ diverge, and so very little can be predicted about this region of non-perturbative QCD that is now open to study at HERA.

On the even larger distance scales of laboratory observation, confinement forbids the detection of free quarks and gluons. Small–scale interactions may be visualised in terms of parton scattering, but the quarks and gluons emerging then undergo a process of *hadronisation*, where further quark pairs are produced from the vacuum to form a final state of hadrons [7]. Figure 1.2 shows a typical neutral current interaction in the H1 detector: the single scattered electron is visible on the right, while the hadronised remnants of the proton appear to the left.

The kinematic variables for $ep$ scattering are calculated in terms of the four–vectors $k^\mu$ and $P^\mu$, for the incoming electron and proton respectively, and $q^\mu$ for the exchanged boson ($k'^\mu$ and $P'^\mu$ describe the scattered system). Interactions are usually parameterised in terms of four Lorentz–invariant kinematic variables:

$$Q^2 = -q^\mu q_\mu,$$

the four-momentum transfer squared or virtuality of the exchanged boson;

$$y = \frac{P^\mu q_\mu}{P^\nu k_\nu},$$

which, in the proton rest frame, is equivalent to the fraction of its energy lost by the electron to the exchanged boson;

$$x = \frac{Q^2}{2P^\mu q_\mu},$$

which, in the proton infinite momentum frame at high $Q^2$, is the fraction of the proton's momentum carried by the struck quark; and

$$W^2 = P'^\mu P'_\mu,$$

the invariant mass squared of the hadronic final state.

However, these four variables are not independent:

$$x = \frac{Q^2}{Q^2 + W^2}$$

(neglecting the proton rest mass), and

$$Q^2 = x\,y\,s,$$

where $s$ is the centre of mass energy squared of the electron-proton system. The kinematics of a process are most often quoted just in terms of $x$ and $Q^2$.

A new kinematic region is available at HERA: the extension of the region far beyond that accessible to previous fixed target experiments (*eg.* EMC [8], BCDMS [9]) is demonstrated in figure 1.3.

A review of some HERA physics processes, including first results to emerge from H1 follows.

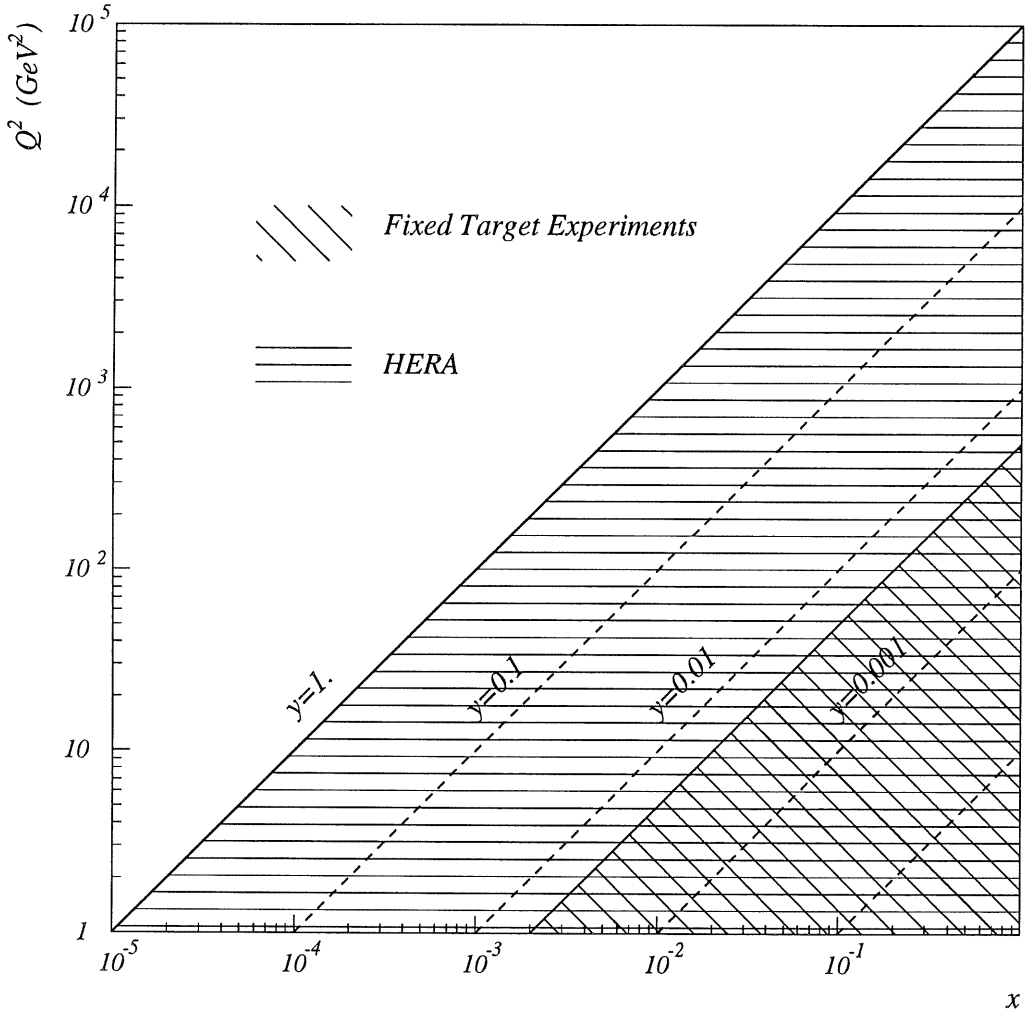


Figure 1.3: Kinematic region accessible at HERA compared to previous fixed target experiments.

## 1.1 Photoproduction

Photoproduction is $ep$ scattering in the low $Q^2$ regime ($Q^2 < 1\,GeV^2$): the photon is of such low virtuality that the physics of the scattering process can be well described in terms of collisions between a proton and a real photon. Photoproduction, as a low $Q^2$ process, dominates the cross-section for $ep$ collisions.

Photoproduction may be "soft" with low tranverse momentum in the final state, or "hard" with higher average transverse momentum in the final state. The soft component is described by the vector meson dominance model (VMD), where the photon couples to a vector meson ($\rho, \omega, \phi, ...$) which then scatters elastically or inelastically off the proton. Hard scattering may be divided into two further subprocesses, *direct* and *resolved* photoproduction (see figure 1.4).

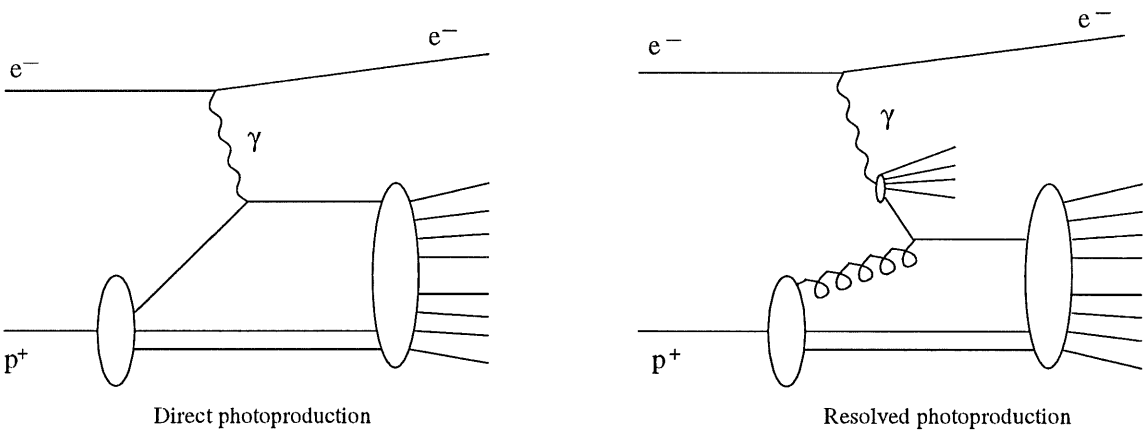


Figure 1.4: Direct and resolved photoproduction.

In the direct process, the photon couples directly to a parton from the proton.

Alternatively, a prediction of QCD is that the photon has hadronic structure which can be resolved when a parton from the photon couples to a parton from the proton in the scattering process: hence this is resolved photoproduction. Jet studies in the photoproduction region have demonstrated the existence of this component in the H1 data [10]. Also, the total cross section for $\gamma p$ collisions can be measured at HERA at centre of mass energies of up to $314\,GeV$, well beyond the energies available to previous experiments. No sharp rise in the cross section with energy is observed [11], consistent with the hadronic model of the photon.

## 1.2 Deep Inelastic Scattering

For $Q^2 > 1\,GeV^2$, $ep$ collisions occur in the deep inelastic scattering (DIS) regime, and the proton structure is probed by the exchanged virtual boson.

The differential cross-section for the DIS neutral current interaction ($\gamma/Z^0$ exchange) is

$$\frac{d^2\sigma}{dx\,dy} = \frac{4\pi\alpha^2}{sx^2y^2}[(1-y+\frac{y^2}{2})F_2(x,Q^2) - \frac{y^2}{2}F_L(x,Q^2) \pm (y-\frac{y^2}{2})xF_3(x,Q^2)],$$

where $\alpha$ is the fine structure constant, and $F_L$, $F_2$ and $F_3$ are the structure functions of the proton. In DIS, for $x$ not too small, the term in $F_L$ (the longitudinal structure function) is small, suppressed by the $y^2$ factor, and can be neglected; $F_3$, describing parity violating contributions becomes significant only when $Q$ approaches the $Z^0$ resonance.

The structure function $F_2$ has been measured at H1 [12] and the results from the 1993 data are shown in figure 1.5. A strong rise in $F_2$ with decreasing $x$ (at fixed $Q^2$) is clearly seen, consistent with the resolution of QCD fluctuations within the proton. The sea quarks and gluons in the proton can radiate gluons, which in turn can produce quark pairs, each successive branching carrying a smaller fraction of the proton's momentum; the virtual boson may scatter these low $x$ partons and the rise of $F_2$ reflects the increase in sea quark and gluon densities as $x$ decreases. The behaviour of $F_2$ in the region of very low $x$ ($< 10^{-4}$) is of great interest : the parton densities may increase to such an extent that the partons overlap, forming "hot spots" within the proton and leading to saturation of the structure functions that may be observable at HERA [2].

$F_2$ is also studied as a function of $Q^2$ at fixed $x$, where the scaling violations of QCD are observed. In the parton model of proton structure where scattering occurs off point-like partons, $F_2$ should have no $Q^2$ dependence. However $F_2$ is seen to have a mild logarithmic $Q^2$ dependence, as demonstrated in [13] and figure 1.6, showing H1 1993 data. This is evidence of asymptotic freedom in QCD: the proton does not consist of free, point-like partons, but partons that only become asymptotically free. Hence the appearance of scaling violations lends powerful support to the theory of perturbative QCD.

The jet structure of deep inelastic events is also of great interest. In general,

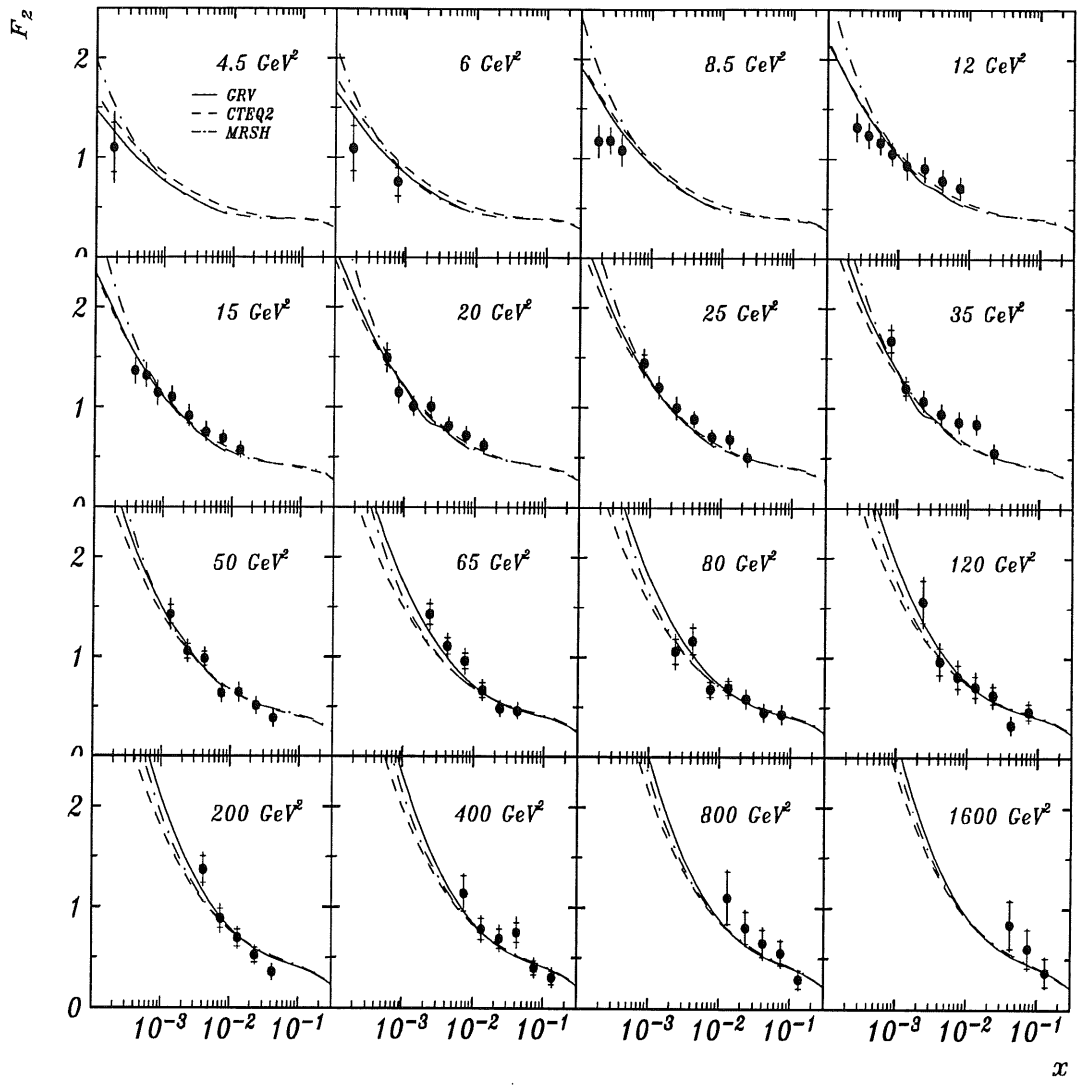


Figure 1.5: The proton structure function $F_2$ measured by H1 and compared to the GRV, CTEQ2 and MRSH parametrisations.

the data is dominated by 1+1 jet events, where the scattered quark forms one jet and the hadronised proton remnant the other (the "+1" jet). 2+1 jet events can be generated by the boson gluon fusion process, where the photon interacts with a gluon from the proton, via a quark loop: the quark-antiquark pair forms two jets alongside the proton remnant (hence 2+1 jets). The isolation of this process allows the study of the gluon content of the proton with the unfolding of the gluon structure function [14], although a substantial background of QCD Compton events (where a gluon radiated from the scattered quark can form a second jet) must be removed.

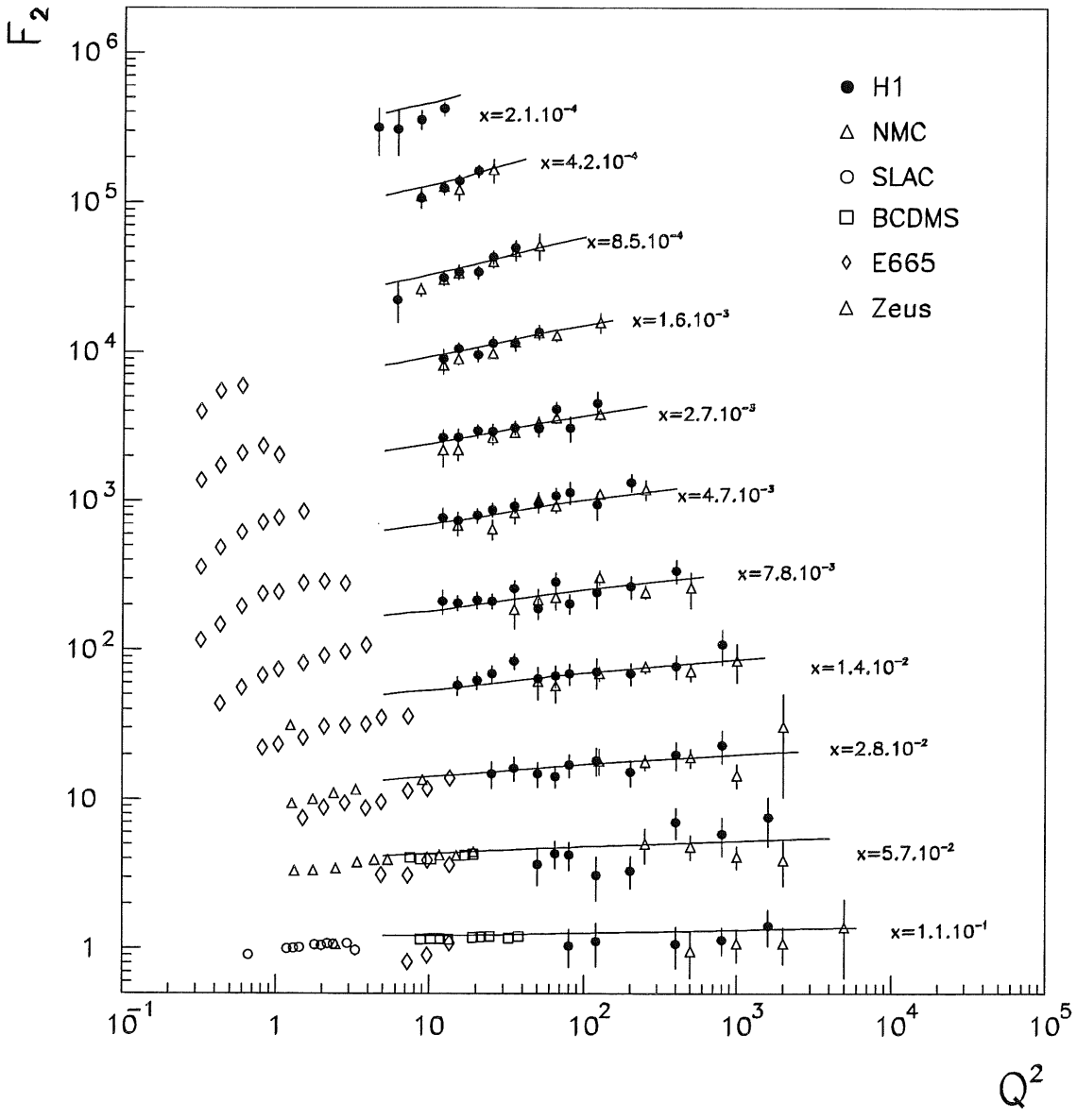


Figure 1.6: The $Q^2$ dependence of the proton structure function $F_2$ for constant $x$.

The fractional 2+1 jet rate can be used to measure the strong coupling constant, $\alpha_s$: at HERA, with the variable $Q^2$ probe, the running of $\alpha_s$ with $Q^2$ can be demonstrated in a single DIS experiment [15].

And the search for exotic physics continues: excited electrons, leptoquarks, leptogluons and supersymmetric particles may all be observed at HERA; null results so far have placed new bounds on the masses and couplings of these particles [16].

## 1.3 Diffractive Physics

In the 1993 HERA data sample, a class of events with a large rapidity [1] gap was observed by the ZEUS experiment [17]. Such an event, as seen in the H1 detector, is shown in figure 1.7: in the forward region of the detector where the hadronised proton remnant is usually seen, there is actually no activity *ie.* there is a large gap in rapidity in the event.

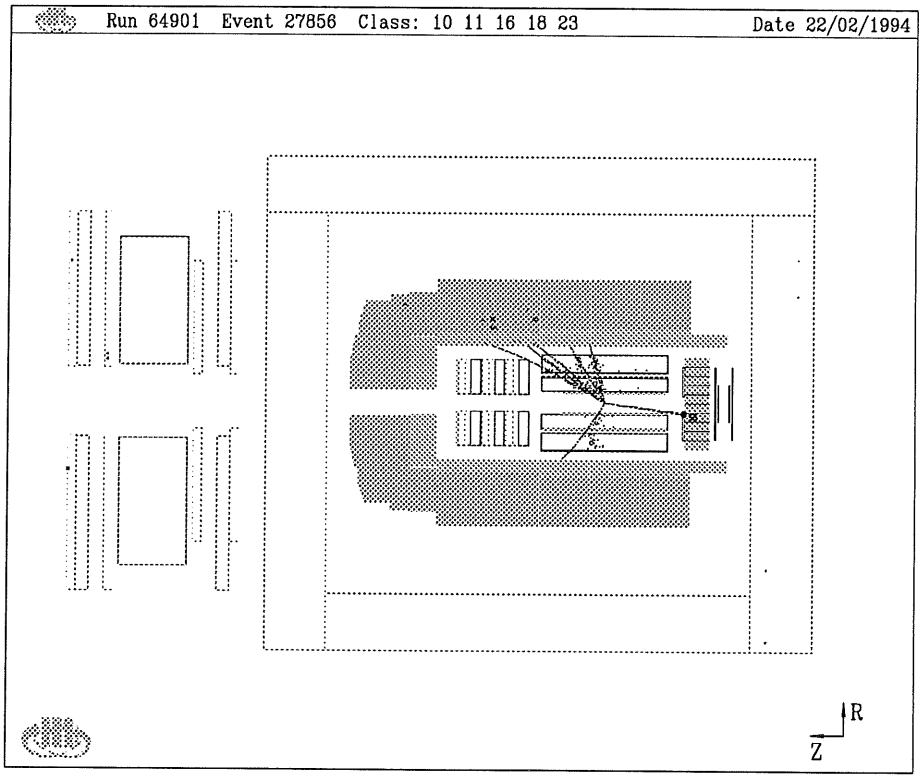


Figure 1.7: Rapidity gap event in the H1 detector.

[1] Rapidity is a Lorentz invariant quantity equivalent to the polar angle $\theta$.

The structure of these events is consistent with hard diffractive scattering off a colourless object within the proton. This colourless object is known as the "pomeron" - although the name is purely generic, and does not necessarily imply that the scattered object is the pomeron of Regge Theory [4]. In fact, very little is yet known about this "pomeron".

The diffractive scattering process is characterised by small momentum loss of the proton, which remains intact (or may undergo soft dissociation) inside the beampipe. As there is no colour connection between the proton and the products of the hard scattering process, the distinctive rapidity gap is formed.

Figure 1.8 shows typical diffractive processes. In the first picture, the photon couples to, for example, a $\rho$ meson, according to the vector meson dominance model, which scatters elastically off the pomeron [18]. The distinctive "two prong" signature of rho decay to two pions is then observed in the detector. Alternatively the photon may probe the structure of the pomeron by scattering off partons within it (second picture). The pomeron remnant hadronises to be seen as one or more jets in the detector. Jet studies of diffractive events can offer vital information on the quark and gluon content of the pomeron.

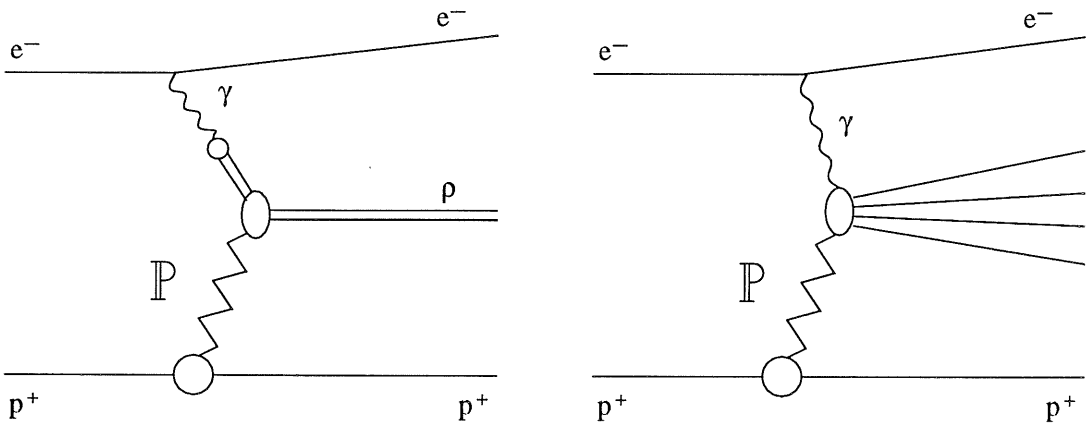


Figure 1.8: Elastic rho production (left) and the photon as a probe of pomeron structure.

## 1.4 Charged Current Interaction

Although the electroweak sector of particle interactions has been widely studied and is reasonably well understood, there are still interesting results that may emerge in the new kinematic regime of HERA.

In the weak charged current process, the electron exchanges a $W^-$ boson with the proton to become a neutrino (see figure 1.9). This escapes the detector, unobserved, but leaving an energy and momentum imbalance in the event characteristic of the process.

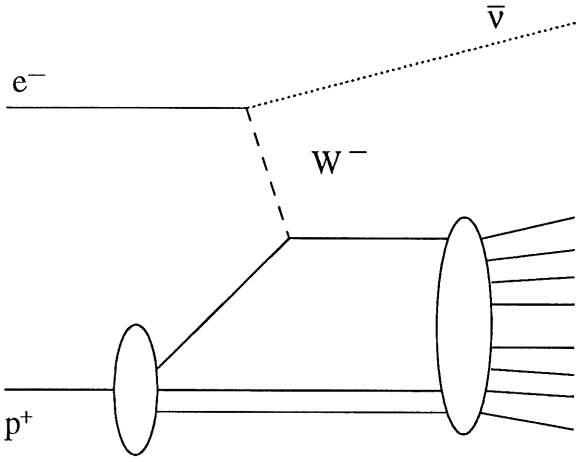


Figure 1.9: The charged current process.

Of particular interest in HERA physics is the effect of the $W$ propagator on the cross-section for charged current interactions. The cross-section contains the term $1/(1 + \frac{Q^2}{M_W^2})^2$ to allow for the mass of the propagating boson. The cross-section increases with $Q^2$, but as $Q^2$ approaches and exceeds the square of the $W$ mass ($M_W = 80.22\,GeV$ [23]) the propagator term will cause the cross-section to be suppressed.

Previous neutrino experiments with beam energies $< 1\,TeV$ have seen no such effect [19], but now HERA (by considering the charged current process "backwards") can measure the $\nu$-nucleon scattering cross-section in conditions equivalent to a $50\,TeV$ beam energy in a fixed target experiment. Fourteen charged current events were observed at H1 in 1993, from which a $\nu N$ cross-section has been calculated [20]. The measurement is compared to low energy data in figure 1.10 and the supression of the charged current cross-section is clearly seen. Figure 1.11 shows the H1 result

compared to the predicted value as a function of propagator mass: within errors, the result is consistent with a propagator mass for charged current equal to the $W$ mass and excludes an asymptotic value.

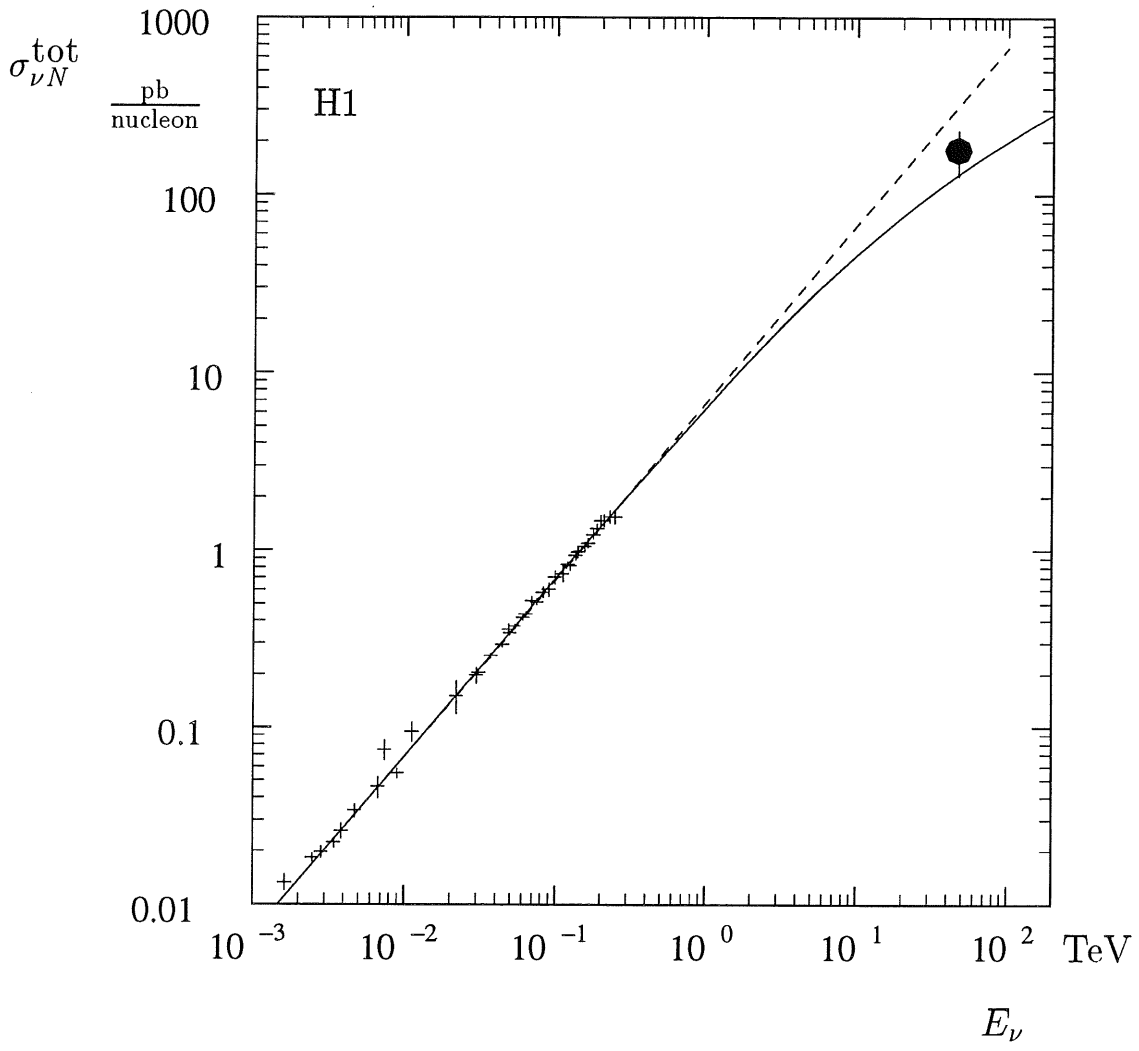


Figure 1.10: The energy dependence of the $\nu N$ cross-section. The crosses represent the low energy neutrino data, while the full circle shows the result for H1 1993 data, converted to a $\nu N$ cross-section for the purpose of comparison. The full line represents the predicted cross-section including the $W$ propagator; the dashed line is the linear extrapolation from low energies.

During the 1994 data-taking period, HERA will replace the electron beam with a positron beam for the study of $e^+p$ collisions. In this scenario, the charged current interaction is mediated by exchange of a $W^+$ boson between photon and quark. Although the rate of charged current events will be reduced, the comparison of electron and positron scattering via $W$ exchange will reveal information on the

quark flavours within the proton.

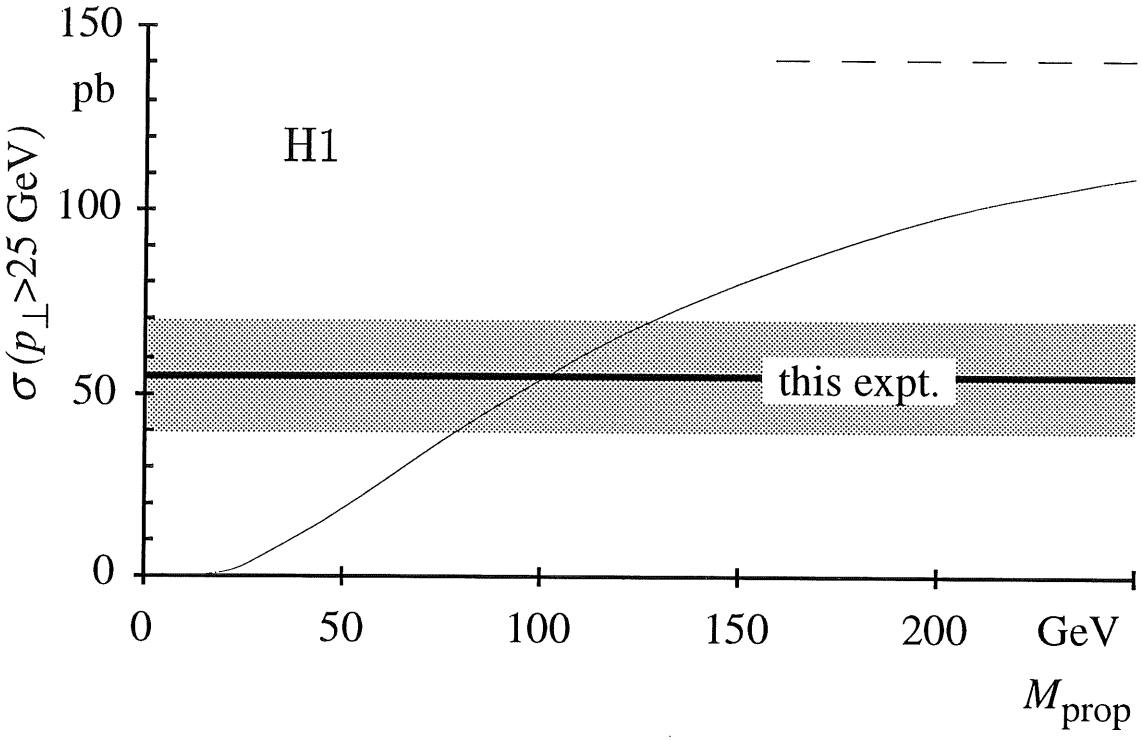


Figure 1.11: Prediction for the CC cross-section as a function of propagator mass (thin solid line) compared to the H1 measured cross-section (thick solid line). The shaded region represents the $1\sigma$ band of the measurement, and the dashed line indicates the asymptotic case $M_{prop} = \infty$.

# Chapter 2

# The H1 Detector

## 2.1 Introduction

The H1 detector programme began in 1984 and the successful collaboration of 36 institutes from 11 countries culminated in the first detected $ep$ collisions in May 1992. H1 utilises many well-established techniques for particle detection, but a particular consideration is the asymmetric nature of $ep$ collisions: the final state is boosted along the proton direction (the "forward" direction), so additional instrumentation is necessary for good resolution and accurate measurement in this region. A cross-section of the H1 detector is shown in figure 2.1.

Tracking and calorimetry are the important tools for any particle detector. The H1 calorimeters are hermetic for good energy measurements, especially of any energy imbalance that is characteristic of charged current processes. They also have fine granularity for resolution of the high-density jets produced in $ep$ collisions. Tracking detectors inside a magnetic field resolve charged particles within these jets, and allow the reconstruction of the primary event vertex. Lepton identification is also important, particularly of the scattered electron from which the kinematics of the event can be calculated.

Although HERA bunch crossings occur every $96\,ns$, the probability of an $ep$ collision in any given bunch crossing is $\sim 10^{-3}$. An effective trigger is needed to reject background events, for example beamwall interactions (between a proton and the wall of the HERA beampipe) and beamgas interactions (between a proton and particles in the imperfect vacuum of the beampipe). This still leaves an event rate of $\sim 100\,Hz$, and so very fast data-processing electronics are implemented.

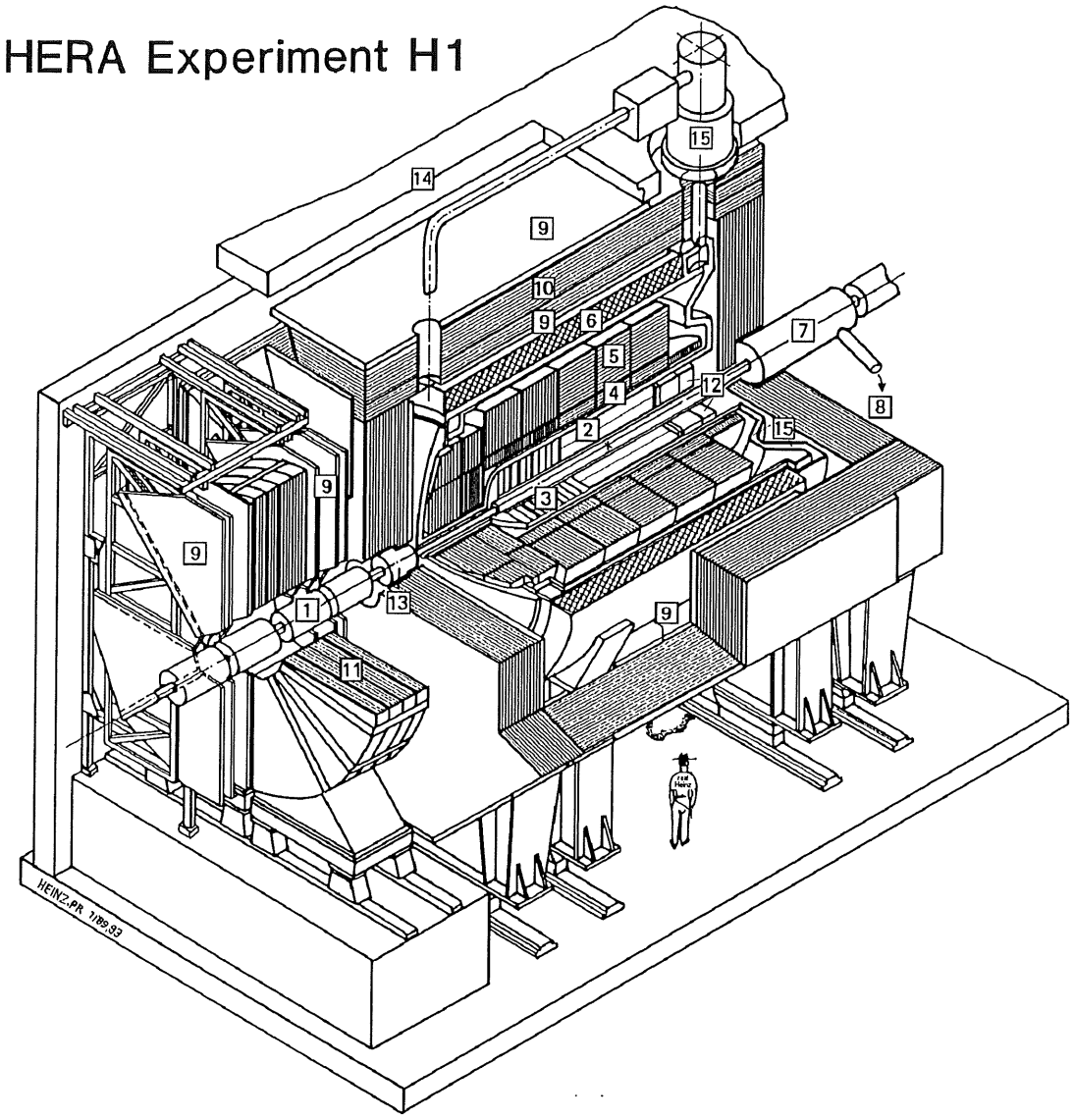


[1] Beam pipe and beam magnets
[2] Central track detector
[3] Forward track detector
[4] Electromagnetic calorimeter
[5] Hadronic calorimeter
[6] Super conducting coil ($1.2T$)
[7] Compensating magnet
[8] Helium cryogenics
[9] Forward muon chambers
[10] Instrumented iron
[11] Forward muon toroid magnet
[12] Backward electromagnetic calorimeter
[13] Plug calorimeter
[14] Concrete shielding
[15] Liquid argon cryostat

Figure 2.1: A cut away view of the H1 detector.

The H1 detector covers as much of the solid angle around the interaction point as possible - the range is restricted by the beampipe of outer radius $192\,mm$ passing horizontally through the centre of the apparatus. Surrounding the beampipe are tracking detectors, in the central interaction region and also in the forward direction. Moving outwards (with reference to figure 2.1), the next component is the calorimeter, divided into two layers for the detection of electromagnetic and hadronic particle showers. The superconducting magnetic coil is placed outside the calorimeter, minimising the amount of dead material in front of this component. The coil has a radius of $3\,m$, and produces a solenoidal field of strength $1.15\ T$ in the centre of H1; the variation in field strength is less than 2% over the whole volume of the tracking detectors. The magnetic field is contained by an iron return yoke, which is also instrumented with streamer tubes to act as a "tail-catcher" for the hadronic calorimeter. The acceptance of the calorimetric system is extended by a hadronic (plug) calorimeter in the forward direction, and a backward electromagnetic calorimeter.

Penetrating muons can be detected in the instrumented iron yoke. In addition muons produced in the forward direction are found by the forward muon spectrometer, positioned outside the main body of the detector. Also outside the detector, in the backward region, are the electron tagger and photon detector, positioned at small angles to the interaction point. These are used for luminosity measurements and measurement of small angle scattered electrons and radiative photons. Similarly in the forward region is a proton tagger. Additional scintillators behind the detector give important timing information useful for background rejection.

A right-handed coordinate system for the detector is defined such that the positive $z$ axis is along the proton direction (i.e. "forward"), with the $y$ axis vertical, and the origin at the nominal interaction point. Cylindrical coordinates $\theta$ and $\phi$ are also defined, such that the polar angle $\theta = 0°$ is the proton direction, through to $\theta = 180°$ in the electron direction. The azimuthal angle $\phi = 0°$ is the positive $x$ axis, and the $xy$ plane is often referred to as the $r - \phi$ plane, where $r$ is the radius in cylindrical coordinates.

Details of the H1 detector can be found in [21]. Brief accounts of the principal components are given in the following subsections.

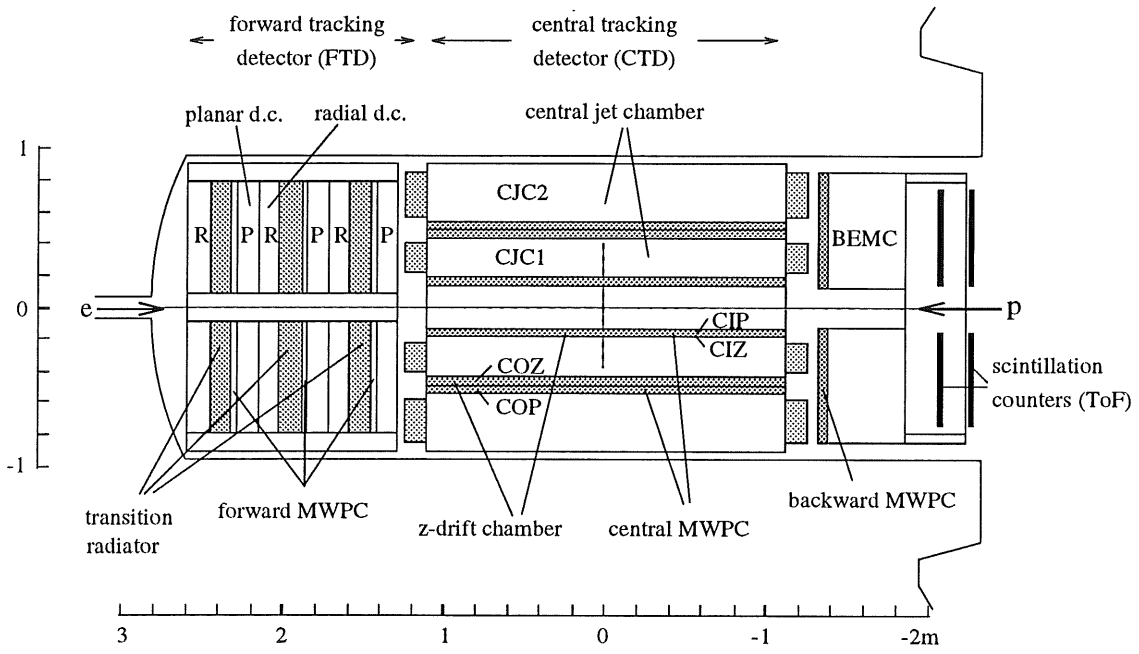


Figure 2.2: An $r$–$z$ projection of the H1 tracking detectors.

## 2.2 Tracking

The tracking system of H1 (figure 2.2) is divided into two sections, the central tracking detector (CTD) and the forward tracking detector (FTD), each combining proportional chambers for fast detection and drift chambers for accurate tracking of charged particles.

Drift chambers are gas-filled with a drift field formed between a cathode and an anode wire. When a charged particle passes through the chamber it causes ionisation of the gas and the electrons released move towards the anode. As the field strength increases around the anode, the drifting electrons multiply to form an avalanche, which, on reaching the wire generates a signal from the chamber. The time at which the signal arrives depends on how far the electrons had to drift through the gas, and so from this the transverse distance of the original charged particle from the wire can be calculated with a typical resolution of a few hundred microns. By taking the signal from both ends of the anode and comparing the proportions of charge collected, the point along the wire at which the charged particle passed can be found. Using an array of drift chambers where the anode wires are staggered allows very accurate reconstruction of charged particle tracks. In addition, in the presence of a magnetic field the particle momenta can be determined, and the specific energy

loss $dE/dx$ can be used for particle identification.

Proportional chambers are very similar in construction to drift chambers but have many closely-spaced anode wires: electrons produced by ionising particles have a very short drift distance, and so, although the position resolution is quite poor, the anode signals arrive very quickly (within $\sim 50ns$) and can be used for triggering purposes.

The main body of the CTD is formed by the central jet chamber (CJC), consisting of two large concentric drift chambers (CJC1 and CJC2). The anode wires are strung in planes parallel to the beam axis, alternating with planes of cathode wires. Each anode plane with a cathode plane either side constitutes a cell. The cells are tilted at 30° azimuthally, optimising track resolution, even for very hard, high-momentum tracks, and removing left-right ambiguities (ie. on which side of the wire the signal originated). The chambers have resolutions $170\,\mu m$ in $r\phi$, $2.2\,cm$ in $z$ by charge division, and 10% in $dE/dx$ [21].

On the inside edge of CJC1, as shown in figure 2.3, are the inner multiwire proportional chamber (CIP) and the inner $z$ chamber (CIZ); sandwiched between CJC1 and CJC2 is a similar layer comprising the outer $z$ chamber (COZ) and the outer multiwire proportional chamber (COP). In the $z$ chambers, the anode wires run perpendicular to the beam direction, looping right round the beampipe region. Four anode wires strung concentrically form a cell; the CIZ has 15 cells along the $z$ direction and the COZ 23. These chambers complement the CJC by providing a $z$ coordinate with a resolution of $300\,\mu m$, while a $\phi$ measurement is possible from charge division.

The CIP and COP each consist of two layers of proportional chambers. Both have pad readout: the CIP has 60-fold segmentation in $z$ and the COP has 18-fold segmentation. In $\phi$, both chambers have 8-fold segmentation, but the layers are rotated half a cell width with respect to each other, so demanding coincidence of signals from the layers doubles the effective segmentation.

The FTD consists of three "supermodules", each comprising, in order of increasing $z$, layers of planar drift chambers, multiwire proportional chambers, transition radiation detectors and radial drift chambers.

In the planar layers the anode wires run parallel to each other, perpendicular to the beam direction. Each layer is rotated through 60° with respect to the other two,

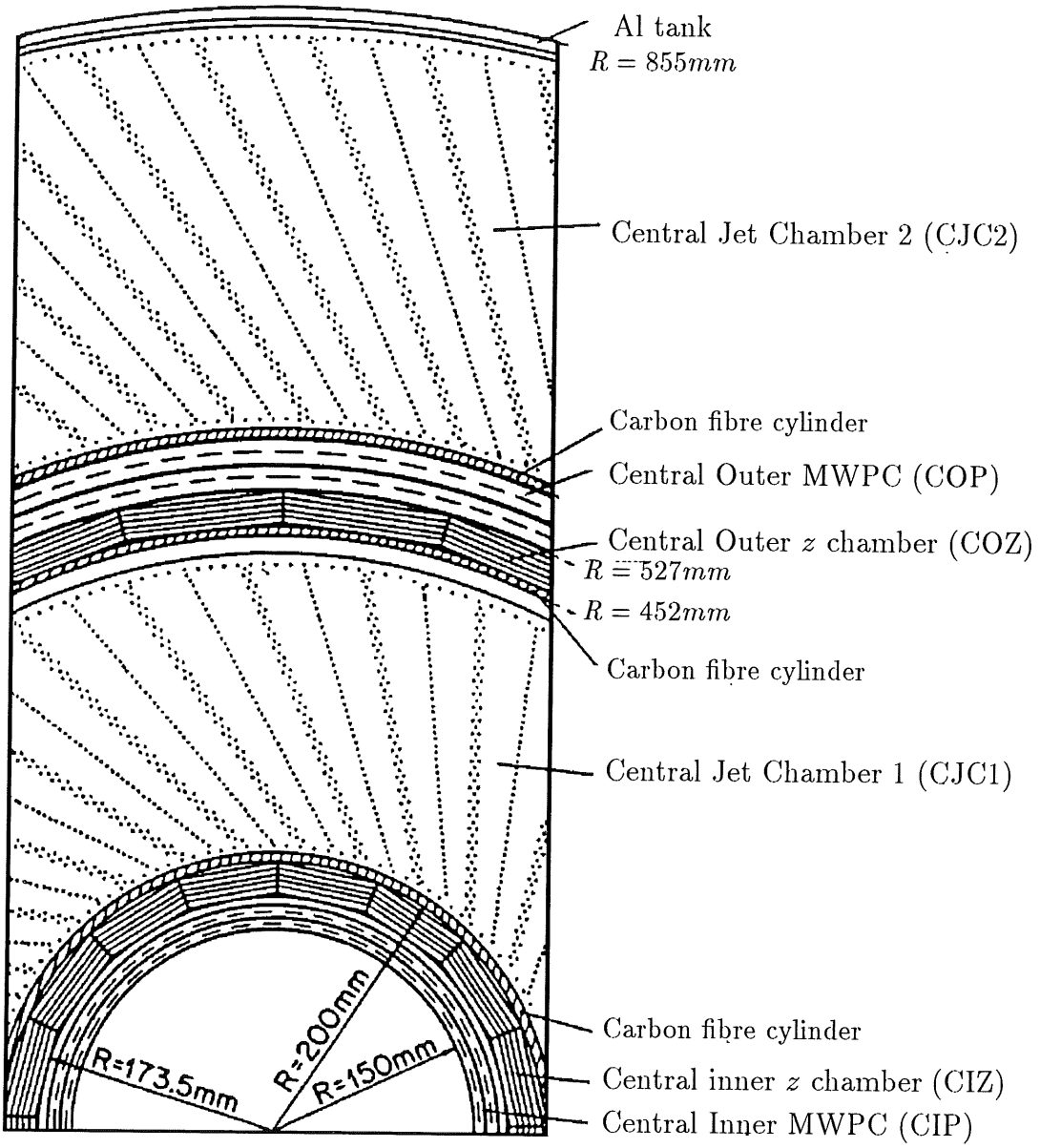


Figure 2.3: A section through the central track detector, perpendicular to the beam.

then combining information from all three layers gives accurate $xy$ measurement. Each proportional chamber has two layers of drift cells with pad readout producing fast signals for timing and triggering. The transition radiation detectors consist of polypropylene foils in a gas-filled volume; when a particle passes through the detector it emits photons in the X-ray region. The detector parameters are such that X-rays from electrons pass through into the radial chamber layer, and a larger pulse is registered at the wire. Hence electron tracks can be recognised. The radial chambers have cells with wires radiating out from the beampipe. The individual layers are staggered by 2.5° and 3.75°, and combined information from the planar and radial chambers gives optimum momentum measurement.

Covering the angular region $155.5° \leq \theta \leq 174.5°$, inaccessible to the central tracking system, is the backward proportional chamber (BPC). This has four layers of anode wires, staggered at 45° to each other and read out directly to achieve an angular resolution of about $0.5\,mrad$ [21].

The tracking system as a whole is designed to achieve a momentum resolution $\sigma_p/p^2 \sim 0.003\,(GeV/c)^{-1}$ and an angular resolution $\sigma_\theta \sim 1\,mrad$ [21].

## 2.3 Calorimetry

H1 has sampling calorimetry with alternate layers of absorber and active material: when a particle is incident upon the absorber (lead or steel) a particle shower is induced, the development of which is detected by layers of active material, giving a measure of the incident particle energy.

The induced particle shower may be of electromagnetic or hadronic nature. An electromagnetic shower is initiated by incident electrons or photons. Here the dominant processes of energy loss are bremsstrahlung $eA \rightarrow eA\gamma$ and pair production $\gamma \rightarrow e^+e^-$ [22]. The longitudinal development of the shower is characterised by the radiation length, $X_0$, the mean distance over which an electron loses all but $e^{-1}$ of its energy. Shower development continues until particle energies are of order $100\,MeV$, where dissipative processes such as ionisation take over. If the shower is completely contained in the calorimeter, the amount of ionisation in the active layers determines the energy of the initial particle.

Hadronic particles lose energy predominantly via inelastic nuclear collisions, pro-

ducing secondary particles that can take part in further collisions. A shower of this nature develops more slowly, as it is characterised by the nuclear interaction length, $\lambda_I$, which is typically much longer than $X_0$ for the absorber material (for lead $\lambda_I \sim 30X_0$) [23]. However, $\pi^0$ mesons produced in these collisions can decay to two photons and thus initiate electromagnetic showers. So hadronic showers are characterised by an initial large energy deposit due to such electromagnetic showers, followed by slow shower development via nuclear collisions. Software compensation [24] is used to correct the energy measurement for the unknown $\pi^0$ content of the shower. Further significant energy loss in hadron showers occurs by break-up or excitation of nuclei which remain undetected in the calorimeter: the response of a hadronic calorimeter is thus worse than that of an electromagnetic calorimeter.

Calorimeter resolution $\sigma_E/E$ is dominated by statistical fluctuations in the number of particles produced in a shower, giving a term proportional to $1/\sqrt{E}$. Other factors in the resolution are noise and leakage of showers outside the calorimeter.

The H1 calorimeter system is shown in figure 2.4. In the central region ($4° \leq \theta \leq 153°$) is the liquid argon calorimeter (LAC), while the backward electromagnetic calorimeter (BEMC) covers the region $151° < \theta < 177°$ and the hadronic plug calorimeter covers the very forward region of $\theta < 4°$. The instrumented iron ($6° < \theta < 172°$) acts as a tail catcher for hadronic showers escaping from the LAC or the BEMC.

The LAC is divided into two layers - the hadronic calorimeter (HAC) and the electromagnetic calorimeter (EMC), the latter being nearest the beampipe. The EMC has lead absorber plates of $2.4\,mm$ depth, the $2.35\,mm$ gaps between them being filled with liquid argon. In each gap is a high-voltage plane and a plane of copper readout pads. The HAC has $19\,mm$ stainless steel absorber plates with a $2.4\,mm$ double gap of liquid argon, divided by a plastic board with readout pads on either side. The thickness of the EMC varies between 20 and 30 radiation lengths, while the LAC as a whole has depth between $5\lambda_I$ and $7\lambda_I$. The fine granularity of the readout cells allows good separation of electromagnetic and hadronic showers by their topologies, and a series of weighting functions can be calculated for the compensation procedure.

The electromagnetic energy resolution of the LAC is approximately $\sigma_E/E = 12\%/\sqrt{E} \oplus 1\%$ [21], for $E$ in $GeV$, with a present calibration uncertainty of 3% [25]. Hadronic energy measurements have resolution $\sigma_E/E = 50\%/\sqrt{E} \oplus 2\%$ [21], with a

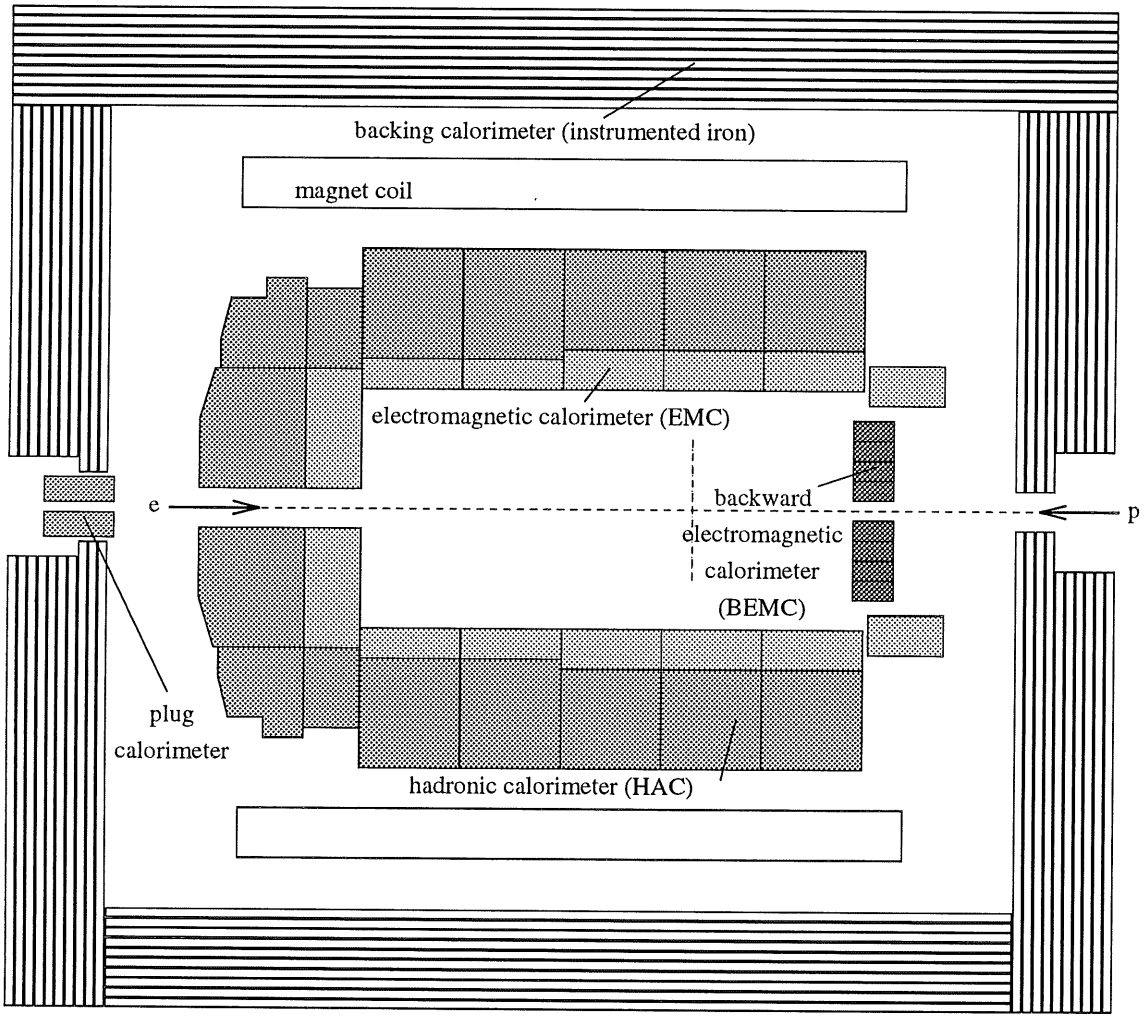


Figure 2.4: An $r$–$z$ view of the calorimeters.

5% calibration uncertainty [25].

The BEMC is mounted in an aluminium barrel of diameter $162\,cm$, positioned at $z = -144\,cm$. The calorimeter has 50 active layers of plastic scintillator of $4\,mm$ thickness interleaved with 49 $2.5\,mm$ layers of lead. For granularity, it is segmented into 88 stacks aligned parallel to the beam axis. Signals are read out via wavelength-shifters along the sides of the stacks. The BEMC is of depth $22.5X_0$, equivalent to 0.97 hadronic absorption lengths: only about 30% of the energy of interacting hadrons is contained in the BEMC, and about 30% of incident hadrons do not register any signal.

The BEMC plays an important rôle in the identification of scattered electrons from low-$Q^2$ deep inelastic scattering events (ie. $Q^2 < 100\,GeV^2$). The electron energy can be measured with resolution $\sigma_E/E = 10\%/\sqrt{E} \oplus 2\%$ [21] (calibration uncertainty 2% [26]), while a position resolution of $1.3\,cm$ is possible. If the BEMC is used in conjunction with the iron tail catcher, a combined resolution of $\sigma_E/E = 80\%/\sqrt{E}$ is achieved [21].

The iron tail catcher utilises 11 of the 16 limited streamer tube layers that have pad readout. Signals from the first 5 or the last 6 layers are summed to give a two-fold segmentation in the hadronic energy measurement. The tail catcher has depth $4.5\lambda_I$ and resolution $\sigma_E/E = 100\%/\sqrt{E}$ [21].

The final calorimetric component is the plug, which closes the gap in acceptance between the beampipe and the forward part of the LAC ($0.6° \leq \theta \leq 3°$), thus minimising the amount of transverse momentum lost from the detector due to hadrons being emitted close to the beampipe, usually in the proton remnant jet. The plug is necessarily a very compact detector, having outer radius $25\,cm$. It consists of nine layers of copper absorber plates interleaved by eight layers of silicon. However the energy resolution is quite poor ($\sigma_E/E = 150\%/\sqrt{E}$ [21]) due to coarse sampling and energy leakage from the detector.

## 2.4 Muon Detectors

Muons of energy greater than $1.2\,GeV$ can penetrate the calorimeter system to reach the iron return yoke, which, in addition to its rôle as a hadronic tail catcher, is also instrumented for muon detection. The yoke offers good angular coverage in the

barrel and endcap regions and is supplemented in the forward region by the forward muon spectrometer. The spectrometer can reconstruct tracks of muons with energies in excess of $5\,GeV$. But for both the iron and the spectrometer, poor measurements of lower energy muons are still useful as pointers to muon tracks in the forward or central tracking systems.

The instrumented iron is formed by 103000 limited streamer tubes (LST's) placed between the laminations of the return yoke. Each LST has a cross-sectional area of $1\,cm^2$; the silver-coated copper-beryllium wire at the centre of the cell has a diameter of $100\mu m$ and is at ground potential. Eight LST's together in a row form a profile. Each profile is coated in low-resistivity graphite paint, to which high voltage is applied. The top of each profile has a high-resistivity cover of Luranyl (a new plastic compound [21]) and to this are attached pads or strips (perpendicluar to the cell wire) for signal readout. The profiles are sealed in pairs in gas-tight boxes and then wrapped in non-conducting foil to insulate the cells from the iron layers of the return yoke.

A non-flammable gas mixture of carbon dioxide, argon and isobutane (88%, 2.5%, 9.5% respectively) is circulated in the cells at a constant overpressure with respect to the atmosphere. The normal operating voltage is $4500\,V$, but as charge gain depends on gas pressure the voltage is adjusted to compensate for fluctuations in atmospheric pressure.

The LST's are arranged in sixteen layers in the iron. The first three layers form a "muon box" in front of the iron. Two layers have strip readout and the other pads. Inside the iron laminations are three layers with pad readout, then a double layer (one pad readout, one strip readout) and finally five layers with pad readout. Behind the iron is another muon box. The cell wires are read out for all sixteen layers, and give a spatial resolution of $3-4\,mm$ with a single layer efficiency of 80%, whereas the five layers with strip readout give $10-15\,mm$ resolution [21]. In addition to their calorimetric measurements, the layers with pad readout also allow the reconstruction of space points, but with a precision of $10\,cm$ [21]. Three-dimensional tracks through the iron are reconstructed by matching the signals from wires and strips and any ambiguities can be resolved by pad information.

The forward muon spectrometer comprises planes of drift chambers positioned either side of a toroidal magnet, and covers the polar angle range $3° < \theta < 17°$. There are in total 1520 drift cells, each of depth $2\,cm$, width $12\,cm$ and length $40-240\,cm$,

with a central nichrome wire of diameter $50\,\mu m$ ($40\,\mu m$ for the smaller chambers). The cell body is formed by two printed circuit board sheets, copper-coated on both sides, with aluminium profiles between each cell. The outer copper layer is earthed to screen the cells, while the inner layer is etched into $4\,mm$ wide strips which act as drift electrodes when high voltage is applied. The sense wires of adjacent cells are connected together at one end to form a U-shaped wire: this reduces the readout electronics necessary, but still allows determination of the track position transverse to the wire, while the coordinate along the wire can be determined by charge division.

Again a non-flammable gas is used, chosen so that the drift velocity remains constant for the voltage range used, while the drift is fast enough to keep the system in time with the central trigger of the experiment. The gas mixture is argon (92.5%), carbon dioxide (5%) and methane (2.5%). The applied field is $480\,V/cm$, producing a drift velocity $\sim 5\,cm/\mu s$, while the sense wire voltage is $4.26\,kV$ ($4.21\,kV$ for $40\,\mu m$ wires). The iron toroid has a field strength of $1.75\ T$ at its outer radius ($2.9\,m$), and $1.5\ T$ at its inner radius ($0.65\,m$).

The arrangement of the drift chamber planes is shown in figure 2.5. Each plane is divided into octants. Four planes have cells positioned tangentially around the beam pipe to measure the polar angle $\theta$ of the traversing muon - the variation in this angle in the magnetic field of the spectrometer allows measurement of the particle's momentum. The remaining two planes with cells positioned radially to the beampipe measure the azimuthal angle $\phi$.

Each plane has two layers of cells, staggered by the width of half a cell to resolve left-right ambiguities. Hits in these double layers form pairs which are then combined into track segments. Tracks before and after the toroid are linked, taking into account energy losses and Multiple Coulomb Scattering that may occur in the iron of the magnet. The chambers have a spatial resolution of $310\,\mu m$ at $\theta = 3°$ deteriorating to $450\,\mu m$ at $\theta = 17°$ [27]. Muon momenta can be measured accurately in the range $5 - 200\,GeV/c$: the lower limit is determined by the amount of material to be penetrated before reaching the spectrometer, while the magnetic field strength of the toroid and the spatial resolution of the drift chambers determine the upper bound.

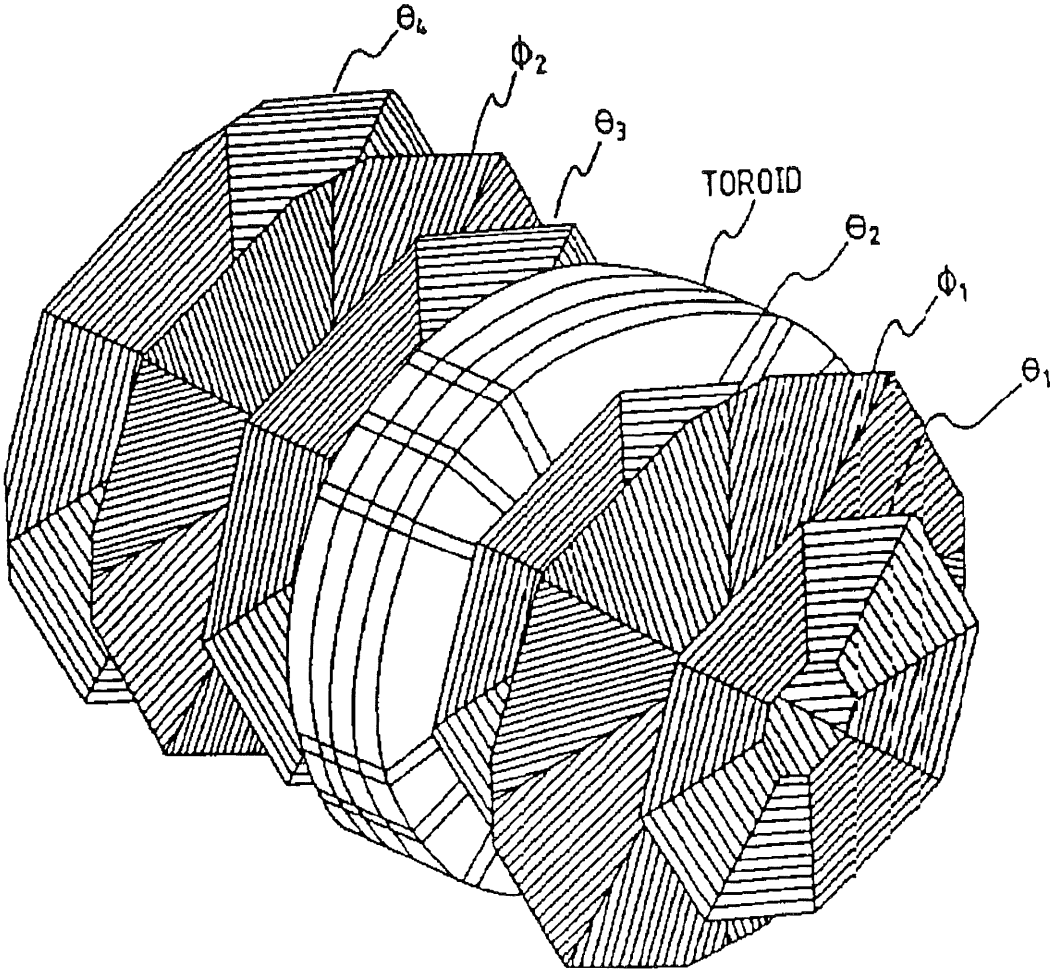


Figure 2.5: Arrangement of the drift planes in the Forward Muon System.

## 2.5 Scintillators

Proton-beamwall and proton-beamgas interactions around the HERA ring produce showers of energetic hadrons and halo muons that are a major source of background events in the H1 detector. Scintillator arrays are installed outside the apparatus to use timing measurements for the rejection of this background.

The time-of-flight device (TOF) is located at $z \approx -2m$, upstream from the BEMC. The two planes of the TOF, perpendicular to the beampipe, are of plastic scintillator/lead sandwich counters, mounted on a steel plate for support and to protect against synchrotron radiation. The inner counters of each plane can be

moved away from the beampipe to minimise damage during beam injection.

Particles from proton background events, usually travelling with a proton bunch, reach the TOF on average $13ns$ before particles coming back from the $ep$ collision. Separation is done on the basis of this timing difference, although the exact interval varies slightly as the proton bunch length of $2-3\,ns$ means many collisions occur away from the nominal interaction point. Time signals from the TOF (with resolution $\sim 4\,ns$) are divided into three windows, defined with respect to the bunch-crossing time. The "global" window extends from one bunch crossing almost to the next ($\sim 96\,ns$) to keep the TOF information with the correct proton bunch. Inside this window is the "background" window of width $25\,ns$, followed by the "interaction" window within which signals from $ep$ collisions occur, with a background of signals from synchrotron radiation. The width of this window is $13.1\,ns$.

Background signals are sent to the central trigger system where triggers from other subdetectors are then suppressed - this causes a 99% decrease in the overall trigger rate and significantly reduces the deadtime of the detector. Interaction and global signals are combined with other detector information to form physics and cosmic ray subtriggers.

Additional scintillator arrays - the inner and outer veto walls, are positioned further upstream of the TOF device, at $z = -8.1\,m$ and $z = -6.5\,m$ respectively. The smaller inner veto wall covers an area of $100 \times 90\,cm^2$ down to a radius of $11\,cm$ around the beampipe. The double layers of scintillator are shielded from electromagnetic showers by lead walls, and give a time resolution of $3\,ns$. The area of the outer veto wall is $5 \times 4\,m^2$ and overlaps the area of the inner veto wall, the liquid argon calorimeter and the endcaps of the iron tailcatcher. The time resolution of this component is $8\,ns$. In a similar way to the TOF device, timing information from the veto walls is used for background rejection, and for the observation of background conditions in HERA.

## 2.6 Particle Taggers

H1 has three devices for the tagging of specific particles: the electron tagger, the proton tagger, and the photon detector.

The electron tagger and photon detector are situated behind the detector and

form the luminosity monitoring system of H1. As the cross-section for the Bethe-Heitler process $ep \rightarrow ep\gamma$ is large and precisely calculable, the rate of these events can be used to calculate the luminosity seen in the detector. The background to this process is bremsstrahlung from residual beam gas $eA \rightarrow eA\gamma$, but this rate can be determined from electron bunches that have no proton bunch partner, known as "pilot" bunches.

The luminosity system must then detect the coincidence of outgoing electrons and photons. Electrons deflected through very small angles can escape through a window in the beampipe to reach the electron tagger at $z = -33.4\,m$. At $z = -92.3\,m$ the beampipe bends upwards and here photons can escape into the photon detector, placed at $z = -102.9\,m$. The photon detector is shielded in front by a layer of lead of width $2X_0$ and a water Čerenkov counter of width $1X_0$ for protection against synchrotron radiation, while a $2\,m$-thick iron shield behind the detector protects against proton beam halo.

Both taggers are total absorption crystal Čerenkov counters (depth $\approx 22X_0$), giving energy resolution $\sigma_E/E = 10\%/\sqrt{E} \oplus 1\%$ and spatial resolution better than $1mm$ [21]. The absolute luminosity at the interaction point can be determined with an accuracy of 5%. The system is also used to tag photoproduction events, by requiring energy in the electron tagger but no signal from the photon detector.

The proton tagger consists of two planes of lead-scintillator sandwich, positioned close to the beampipe at $z = 24\,m$. The tagger covers an area of $60 \times 60\,cm^2$, and detects particles emerging in the proton remnant jet. In fact, there is a considerable amount of dead material in front of this detector, so the tagger sees mainly particles produced in secondary scatters. But this information is still useful as a veto for quasi-elastic proton scattering (such as diffractive processes), where the proton will emerge with low transverse momentum and remain unseen in the beampipe.

## 2.7 Trigger

At HERA, high-current particle bunches cross once every $96\,ns$ ($1\,BC = 96\,ns$) and although the probability of an $ep$ collision in any bunch crossing is low, significant backgrounds arise from synchrotron radiation, proton-beamwall and proton-beamgas interactions. The maximum logging rate of the data acquisition system (DAQ) is $\sim 50\,Hz$, compared to the event rate of almost $10\,MHz$: an effective trig-

ger for $ep$ collisions, rejecting background, is therefore essential for the reduction of the data volume to be processed.

Efficient trigger decisions cannot be made within the bunch-crossing interval – time must be allowed for the response of the calorimetry and tracking systems, as well as cable delays in the readout. H1 therefore has a pipelined readout system: information from each subdetector is fed into a pipeline and stored until all detector information is available for that event and a trigger decision can be made. The system is synchronised with the HERA clock so that all information for a particular bunch crossing remains together.

The trigger is divided into four levels, gradually making more sophisticated decisions. Signatures of $ep$ collisions that are distinct from background processes are an interaction vertex within the fiducial volume of H1 and a higher total transverse energy, due to the hard scattering process. This information forms the basis of the Level 1 trigger. L1 makes a decision on an event 24 $BC$ after its occurrence and if it is a candidate $ep$ collision an "L1KEEP" signal is sent to the central DAQ system. At this point, deadtime begins (*ie.* the detector readout is disabled) as the pipeline is stopped and the accepted event is read into the next trigger level.

Level 2 and level 3 make more complicated decisions using the topology of the event. The design event rate at L2 is 200 $Hz$, reducing to 50 $Hz$ at L3 (in line with the data logging limit). These trigger levels are not yet implemented. At present the events passed at L1 go straight to the L4 trigger.

The L4 trigger has access to all detector information to fully reconstruct the event. It operates asynchronously, so deadtime ends when this level is reached. L4 filter algorithms discard events considered to be of no interest, in particular a three-dimensional vertex reconstruction is very effective against beamwall and beamgas backgrounds that have survived previous trigger levels. The final event rate at L4 is 5 $Hz$, and the data are then written to tape in the DESY computer centre.

# Chapter 3

# Method of Event Classification

## 3.1 Introduction

To study rates and cross-sections for different interactions in $ep$ collisions, it is first necessary to identify the physics process in an event. Basic classification occurs at trigger level, where certain characteristics of physics processes are recognised. More complicated algorithms applied offline ("Level 5") allow more precise determination of the interaction involved. For example, a large imbalance in the total transverse momentum measured in the detector can be a signature of a charged current event, where the neutrino escapes unseen. However, as can be seen in figure 3.1, other processes may also have significant missing transverse momentum ($P_\perp$), such as neutral current, photoproduction, beamgas and cosmic events.

Requiring a missing $P_\perp$ in excess of $25\,GeV$ will eliminate neutral current and photoproduction events, but the charged current sample will still be contaminated with a background from beamgas and cosmic events. Many genuine charged current events will also have been lost in applying this cut. A better approach would be the statistical separation of the event sample into different processes. Such a method, devised by Marshall [29], is presented here.

The distribution of a given variable can be reasonably described by its mean, variance and further higher moments. The distribution for the data is simply a superposition of the distributions of each physics class, in a combination that reflects the rate of each process. If the distribution for each class is determined from Monte Carlo generated data, and its moments calculated, the H1 data can be fitted to this information to calculate the number of events of a given process present in the

sample.

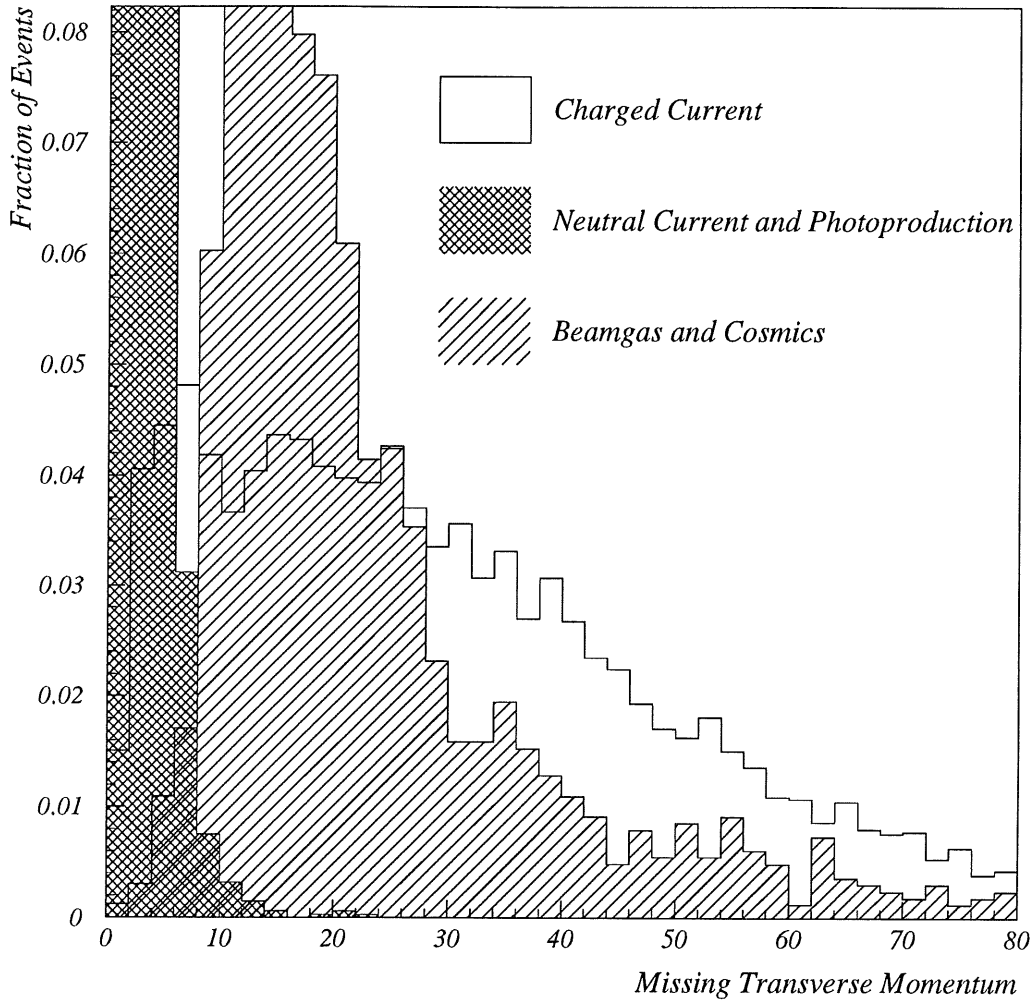


Figure 3.1: Missing transverse momentum distribution for charged current processes, with neutral current, photoproduction, beamgas and cosmic backgrounds. The distribution for beamgas and cosmic events is taken from "pilot" bunch information, all others are from Monte Carlo generated data.

Several variables that discriminate between physics classes can be used in conjunction to improve the accuracy of the fit. Here, this method has a distinct advantage over conventional fitting techniques, which, when using many variables, encounter problems in trying to populate the phase space with enough Monte Carlo statistics: in this separation the variable distributions are handled individually, but correlations between variables are also taken into account. The fitting method reduces to a single matrix equation which can be solved quickly and easily.

## 3.2 Principle of the Method

Consider a data sample known to contain events from two physics processes – $x_1$ events of one process and $x_2$ events of the other, with a total of $N$ events in the sample. Then, choosing a variable whose mean is different for each process ($\mu_1$ and $\mu_2$) and utilising the Central Limit Theorem [28],

$$x_1\mu_1 + x_2\mu_2 = m_1,$$

where

$$m_1 = \sum_{j=1}^{N} \xi_j$$

and $\xi_j$ are the measured values of the chosen variable from the data. To improve discrimination between processes, more variables can be introduced. For $k$ variables there are then $k$ constraint equations:

$$\begin{aligned} x_1\mu_{11} + x_2\mu_{21} &= m_1 \\ x_1\mu_{12} + x_2\mu_{22} &= m_2 \\ &\vdots \\ x_1\mu_{1k} + x_2\mu_{2k} &= m_k. \end{aligned}$$

An additional constraint exists in that the number of events for each class summed together must equal the total number of events in the sample, ie.

$$x_1 + x_2 = N = m_{k+1}.$$

Rearranging the constraint equations, and using the Einstein summation convention for indices

$$x_i\mu_{ij} - m_j = F_j$$

with $i = 1, .., c$ for $c$ classes to be separated, $j = 1, .., k+1$ and defining $\mu_{i(k+1)} = 1$ for all $i$. The solution is then found by requiring $F_j = 0$. However, using more variables (and hence constraint equations) than there are classes to be separated means that the system is over-constrained, and so no simultaneous solution to the equations can be found. This problem is solved by allowing the measured quantities $m_j$ to vary within their errors , *ie.* $m_j \to m_j + \Delta m_j$, where $\Delta m_j$ is the adjustment made to each $m_j$. The constraint equations are now written

$$x_i\mu_{ij} - m_j - \Delta m_j = F_j$$

or, in matrix notation,

$$\mathbf{x}\mu - \mathbf{m} - \mathbf{\Delta m} = \mathbf{F}. \tag{3.1}$$

## 3.3 Single Matrix Equation

The solutions to $\mathbf{F} = \mathbf{0}$ are found by minimising $\chi^2$, which is defined for this situation as:

$$\chi^2 = \mathbf{\Delta m^T V^{-1} \Delta m + 2a.F}. \tag{3.2}$$

$\mathbf{V}$ is the covariance matrix for all variables used in the fit, so the degree of correlation between variables can easily be seen and is included in the fit. Varying the Lagrange multipliers $\mathbf{a}$ allows the $\mathbf{F} = \mathbf{0}$ condition to be satisfied (the factor 2 will cancel later).

As the total number of events $N$ is included as a constraint in the fit, it too should appear in the covariance matrix. The off-diagonal elements in the rows and columns corresponding to $N$ should be zero since every measurement of the number of events is equal to one, and should therefore be independent of all other variables. But if the covariance matrix is calculated in the normal way, the diagonal element corresponding to the square of the error on the measurement of $N$ will also be zero – a complete row and column of zeroes appear in the covariance matrix and attempts to invert the matrix to perform the fit will fail. Instead the diagonal element is forced to be $N$, *ie.* $\sigma_N = \sqrt{N}$, breaking up the rows of zeroes and making it possible to invert the covariance matrix. Putting a $\sqrt{N}$ error on the number of events in the sample is not inappropriate: if $N$ events are observed in one data-taking period, the number of events expected to be observed in a similar running period is $N \pm \sqrt{N}$.

The solution to the fit is defined by the conditions

$$\frac{\partial \chi^2}{\partial \mathbf{\Delta m}} = 0, \quad \frac{\partial \chi^2}{\partial \mathbf{x}} = 0, \quad \frac{\partial \chi^2}{\partial \mathbf{a}} = 0.$$

From equation 3.2,

$$\frac{\partial \chi^2}{\partial \mathbf{\Delta m}} = 2\mathbf{V^{-1}\Delta m} + 2\frac{\partial \mathbf{F}}{\partial \mathbf{\Delta m}}\mathbf{a}$$

$$\frac{\partial \chi^2}{\partial \mathbf{x}} = 2\frac{\partial \mathbf{F}}{\partial \mathbf{x}}\mathbf{a}$$

$$\frac{\partial \chi^2}{\partial \mathbf{a}} = \mathbf{F}.$$

To construct a single matrix equation in a suitable form, the last equation above is adapted by defining (with reference to equation 3.1),

$$\mathbf{F'} = \mathbf{x}\mu - \mathbf{\Delta m} = \mathbf{m}.$$

So the solution is now given by

$$\mathbf{V^{-1}\Delta m} + \frac{\partial \mathbf{F}}{\partial \mathbf{\Delta m}}\mathbf{a} = 0$$

$$\frac{\partial \mathbf{F}}{\partial \mathbf{x}}\mathbf{a} = 0$$

$$\mathbf{F'} = \mathbf{m}.$$

These conditions are combined to form the equation

$$\mathbf{S\,f} = \mathbf{g}, \tag{3.3}$$

where

$$\mathbf{S} = \begin{pmatrix} \mathbf{V^{-1}} & \frac{\partial \mathbf{F}}{\partial \mathbf{\Delta m}} & \mathbf{0} \\ \mathbf{0} & \frac{\partial \mathbf{F}}{\partial \mathbf{x}} & \mathbf{0} \\ \mathbf{-I} & \mathbf{0} & \mu \end{pmatrix},$$

$$\mathbf{g} = \begin{pmatrix} \mathbf{0} \\ \mathbf{m} \end{pmatrix},$$

and

$$\mathbf{f} = \begin{pmatrix} \mathbf{\Delta m} \\ \mathbf{a} \\ \mathbf{x} \end{pmatrix}.$$

$\frac{\partial \mathbf{F}}{\partial \mathbf{\Delta m}}$ and $\frac{\partial \mathbf{F}}{\partial \mathbf{x}}$ are found from equation 3.1: $\frac{\partial \mathbf{F}}{\partial \mathbf{\Delta m}} = \mathbf{-I}$, the negative unit matrix, and $\frac{\partial \mathbf{F}}{\partial \mathbf{x}} = \mu$, the matrix of mean values. With $\mu$ calculated from Monte Carlo generated data, all components of $\mathbf{S}$ are known, and the vector of measured values, $\mathbf{m}$ can be inserted in $\mathbf{g}$.

The solution $\mathbf{x}$ appears at the bottom of the matrix $\mathbf{f}$. A standard library routine can be used to solve $\mathbf{f} = \mathbf{S^{-1}g}$, using all matrices in double precision. The vectors $\mathbf{a}$ and $\mathbf{\Delta m}$ are returned in $\mathbf{f}$ too, and so do not need to be known outside the program, although the size of the $\Delta m$ adjustments gives some indication of how well the fit has been performed.

It is perhaps worth noting again the importance of the Central Limit Theorem in this fit. The method is valid (*ie.*$\chi^2$ follows the $\chi^2$ distribution) if all $m_k$ have a gaussian distribution: although a variable may be described by a non-gaussian

distribution, repeated sampling of the distribution and then summation to calculate $m_k$ means that, by the Central Limit Theorem, $m_k$ will have a gaussian distribution.

For this reason too, the separation technique is not directly applicable to the classification of individual events, where a fit to single measurements would be required to give the probability of the event belonging to a particular class. Here there is no summation of measured values, the Central Limit Theorem cannot be applied and the method becomes invalid.

## 3.4 Extension to Higher Moments

Higher moments of the variable distributions can be included in the fit by constructing similar constraint equations, *eg.* for the second moment, or variance $v_{il}$,

$$x_i v_{il} = m_l, \qquad l = k+1, 2k,$$

with the sum of events $N = m_{2k+1}$ for simplicity. These equations can be handled in exactly the same way as the equations using the mean value of each sample, provided their linearity in $x$ is preserved – each measured value of the variance must be defined with respect to the mean of the *whole* data sample for that variable, $\mu_{s_l}$:

$$m_l = \sum_{j=1}^{N} (\xi_j - \mu_{s_l})^2,$$

where $\xi_j$ are the measured values, as before.

The number of constraint equations can be extended to include as many moments as required, with the $n\,th$ moment given by

$$m_l = \sum_{j=1}^{N} (\xi_j - \mu_{s_l})^n.$$

The total number of constraint equations used in the fit for $k$ variables and $n$ moments is then $n * k + 1$.

## 3.5 $\chi^2$ for the Fit

From the information returned by the matrix inversion routine, the $\chi^2$ value for the fit can be calculated. This should be compared to the number of degrees of freedom of the fit to decide how well the separation of event classes has been performed.

To determine the number of degrees of freedom it is easier to consider $\chi^2$ in the form

$$\chi^2 = \sum_{j=1}^{n*k+1} \frac{(m_j - < m_j >)^2}{\sigma_{m_j}^2},$$

where $< m_j >$ is the expectation value of $m_j$ and $\sigma_{m_j}$ is the error on $m_j$ (the term in $\mathbf{F}$ included in the fit in equation 3.2 can be neglected in this discussion, as the $F_j$ are forced to be zero and do not affect the degrees of freedom). As the sum is over $n * k + 1$ terms, $\chi^2$ has $n * k + 1$ degrees of freedom. Then if the $m_j$ are well measured and the errors, $\sigma_{m_j}$, correctly estimated, each term in the sum is $\sim 1$, so $\chi^2 \sim n * k + 1$ and $\chi^2$ per degree of freedom $\sim 1$.

However, there is an additional consideration: $< m_j >$ depends on the amount of each process present in the sample, so varying the $x_i$ affects $< m_j >$. If there are $c$ classes to be separated (*ie.* $x_i$ with $i = 1, .., c$), then $c$ degrees of freedom in $\chi^2$ are lost — $\chi^2$ has $(n * k + 1) - c$ degrees of freedom.

Alternatively, consider the vectors $\mathbf{m}$ and $< \mathbf{m} >$ in $(n*k+1)$-dimensional space. The separation of the two vectors is described by $\mathbf{\Delta m}$, and $|\mathbf{\Delta m}| \equiv \chi^2$. But $< \mathbf{m} >$ is not fixed: the values $x_i$ define a manifold in $c$-dimensional space on which $< \mathbf{m} >$ must lie. The solution is found where the separation of $\mathbf{m}$ and $< \mathbf{m} >$ is least, *ie.* $\chi^2$ is minimised. $\chi^2$ has $(n * k + 1)$ degrees of freedom from the components of $\mathbf{\Delta m}$, but also $c$ constraints to the manifold of $< \mathbf{m} >$, leaving $(n * k + 1) - c$ degrees of freedom for the fit.

## 3.6 Error Calculation

An error matrix $\mathbf{V_x}$ giving the statistical errors on $\mathbf{x}$ can be calculated. By the propagation of errors,

$$\mathbf{V_x} = \frac{\partial \mathbf{x}}{\partial \mathbf{m}} \mathbf{V} \frac{\partial \mathbf{x}}{\partial \mathbf{m}}^T,$$

where $\mathbf{V}$ is the covariance matrix, as before. To find $\frac{\partial \mathbf{x}}{\partial \mathbf{m}}$, it is necessary to return to equation 3.3, and differentiate this with respect to $\mathbf{m}$:

$$\mathbf{S} \frac{\partial \mathbf{f}}{\partial \mathbf{m}} = \frac{\partial \mathbf{g}}{\partial \mathbf{m}},$$

or

$$\frac{\partial \mathbf{f}}{\partial \mathbf{m}} = \mathbf{S}^{-1} \frac{\partial \mathbf{g}}{\partial \mathbf{m}}.$$

$\frac{\partial \mathbf{x}}{\partial \mathbf{m}}$ appears as the last elements of $\frac{\partial \mathbf{f}}{\partial \mathbf{m}}$. $\mathbf{S}^{-1}$ has already been returned by the matrix inversion routine and since all elements of $\frac{\partial \mathbf{g}}{\partial \mathbf{m}}$ are 0 or 1, $\frac{\partial \mathbf{x}}{\partial \mathbf{m}}$ can simply be taken from the relevant elements of $\mathbf{S}^{-1}$. $\mathbf{V_x}$ can then be calculated, and the square roots of its diagonal terms are the statistical errors on $\mathbf{x}$.

# Chapter 4

# Testing the Algorithm

## 4.1 Introduction

The charged current process at HERA and the difficulty in isolating a pure sample of such events have been considered previously (chapters 1 and 3). Identification of charged current processes presently relies on high missing $P_\perp$ cuts ($\sim 25\,GeV$), cuts against beamgas and cosmic muon events and then visual scanning of event pictures to remove the remaining background. The matrix fitting routine outlined in the previous chapter has been applied to the identification of the charged current process, in the hope of improving the ease and efficiency of selection for these events.

In the H1 1993 data sample fourteen charged current events have been identified [20]. This pure sample of events has been "doped" with a known sample of neutral current events and then used to test the power of the matrix fitting algorithm.

To use this method it is essential that each process included in the separation routine can be well described by a Monte Carlo simulation. Several Monte Carlo programs exist for $ep$ physics, the principal ones are reviewed below.

## 4.2 Monte Carlo Generators

Monte Carlo generators [30] model $ep$ interactions as a hard scattering process involving two partons, each of which is part of a parton shower evolved from the incoming proton and photon. The generator begins (for efficiency) with the hard

subprocess described by the relevant element of the scattering matrix. Then the initial state and final state parton showers are added and evolved (the initial state parton shower is actually evolved backwards to the incoming particle, with the evolution governed by the structure function of that particle). Successive branchings within the shower produce partons of ever decreasing virtuality ($Q^2$) down to some minimum scale ($Q_0^2 \sim 1GeV$), beyond which perturbative QCD is invalid. At this point the final state partons and final state remnants of the incoming particles undergo a non-perturbative hadronisation process and are allowed to decay.

The generation chain is completed by the simulation process [31], where the detector response to the event is included, *ie.* the generated information is adapted to what would actually be observed in the H1 detector by allowing for (*eg.*) calorimeter response, secondary scattering, dead material, *etc.* Monte Carlo data should then be directly comparable with real H1 data, if the model of the physics process is accurate.

Of the many Monte Carlo programs for *ep* physics a couple are particularly favoured for their more accurate description of H1 data. The LEPTO program [32] models lepton-nucleon scattering via matrix elements and parton showers (ME+PS) as discussed above, with hadronisation performed by the JETSET program [33], according to the Lund String Model [7]. Alternatively LEPTO can be interfaced to ARIADNE [34] which, while using the LEPTO description of hard scattering, then generates a parton cascade via colour dipole emission: two partons emerging from the hard scattering process form a colour dipole that can radiate a gluon to form two colour dipoles, between each parton and the gluon, and these in turn radiate to form further dipoles. Thus the shower develops and QCD coherence effects can be correctly included.

The DJANGO [35] program provides an interface between LEPTO and HERACLES [36], the latter program including first order radiative corrections to the deep inelastic scattering process. Parton cascades are created by ARIADNE and hadronisation is done by JETSET.

Additional input to the Monte Carlo programs are the structure functions of the incoming particles. For the proton, many structure functions have been calculated from existing low-energy data ( in particular the MRSD0 and MRSD– [38] parametrisations) and extrapolated to describe the low $x$ region. Inaccuracies have been revealed by comparison of these extrapolations to HERA $F_2$ measurements at

low $x$ (see figure 1.5) and new refined structure functions have been developed to fit the HERA data (*eg.* the MRSH parametrisation [39]).

Of all the programs, the colour dipole model of ARIADNE best describes the energy flow observed in the H1 detector [37]. This program, within the DJANGO framework, is preferentially used, in conjunction with the MRSH structure function derived from HERA data.

## 4.3 Variables Used for Separation

First, suitable variables for the discrimination of charged and neutral current events are needed. The momentum imbalance of charged current interactions due to loss of the final state neutrino can be clearly seen in figure 4.1: compare this to the neutral current picture (figure 1.2) where only a small imbalance occurs due to loss of particles in the beampipe.

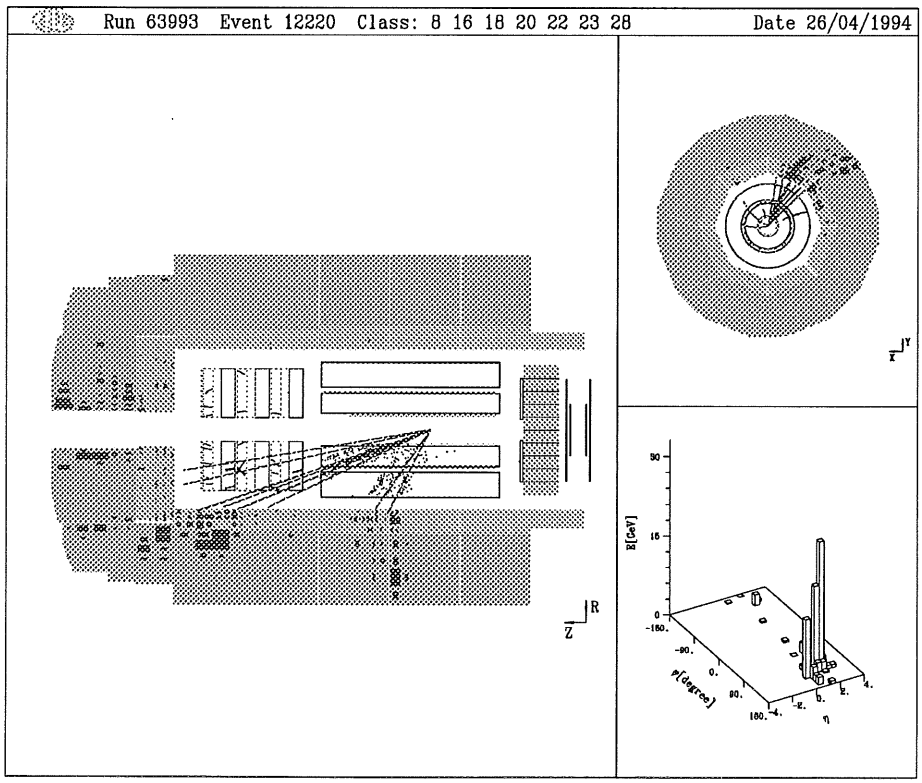


Figure 4.1: A charged current event observed in the H1 detector. The momentum imbalance is clearly seen in the radial view (top right).

Monte Carlo generated distributions of missing $P_\perp$ for the two processes are shown in figure 4.2, and can be seen to have very different moments (*ie.* mean, width, skew, etc.).

An additional variable that offers some discrimination between the processes is the "tranverse energy weighted mean pseudorapidity", $\overline{\eta}_{E_\perp}$. Pseudorapidity, $\eta$ of a particle is defined as

$$\eta = -ln\{tan(\frac{\theta}{2})\},$$

where $\theta$ is the polar angle. Pseudorapidity is often favoured for describing the angular distribution of particles and in the H1 detector has the range (approximately) $4 > \eta > -3$ ( positive $\eta$ in the forward direction). $\overline{\eta}_{E_\perp}$ is the mean pseudorapidity over all particles in the event, weighted by the transverse energy of each particle, *ie.*

$$\overline{\eta}_{E_\perp} = \frac{\sum_{i=1}^{N} \eta_i \, E_{\perp_i}}{\sum_{i=1}^{N} E_{\perp_i}},$$

for $N$ particles in the event. As can be seen in the lower plot of figure 4.2, the distribution of $\overline{\eta}_{E_\perp}$ for charged current events is over more forward values of pseudorapidity than for neutral current events, whose $\overline{\eta}_{E_\perp}$ distribution is influenced by the presence of the scattered electron usually in the backward detector region.

The moments of the variable distributions to which the fit is made are listed in table 4.1. The values are distinct, although $\overline{\eta}_{E_\perp}$ does lose discriminating power above the fifth moment.

| | Missing $P_\perp$ | | $\overline{\eta}_{E_\perp}$ | |
|---|---|---|---|---|
| Moment | Charged current | Neutral current | Charged current | Neutral current |
| 1 | 30.08662 | 2.144584 | 1.287443 | 0.3207602 |
| 2 | 450.9991 | 2.303722 | 0.648936 | 0.3606161 |
| 3 | 9360.926 | 10.97200 | 0.186099 | -0.9634137 |
| 4 | 781072.4 | 142.5457 | 1.082292 | 0.6841397 |
| 5 | 41061120. | 2068.241 | 0.7757519 | -0.6050935 |
| 6 | $2.9707 \times 10^9$ | 33027.66 | 2.705567 | 2.794519 |

Table 4.1: Moments of missing $P_\perp$ and $\overline{\eta}_{E_\perp}$ distributions for neutral and charged current processes.

The moments of the missing $P_\perp$ distribution have large values, whereas the $\overline{\eta}_{E_\perp}$ moments are distributed closely around zero. For stability in the matrix fitting

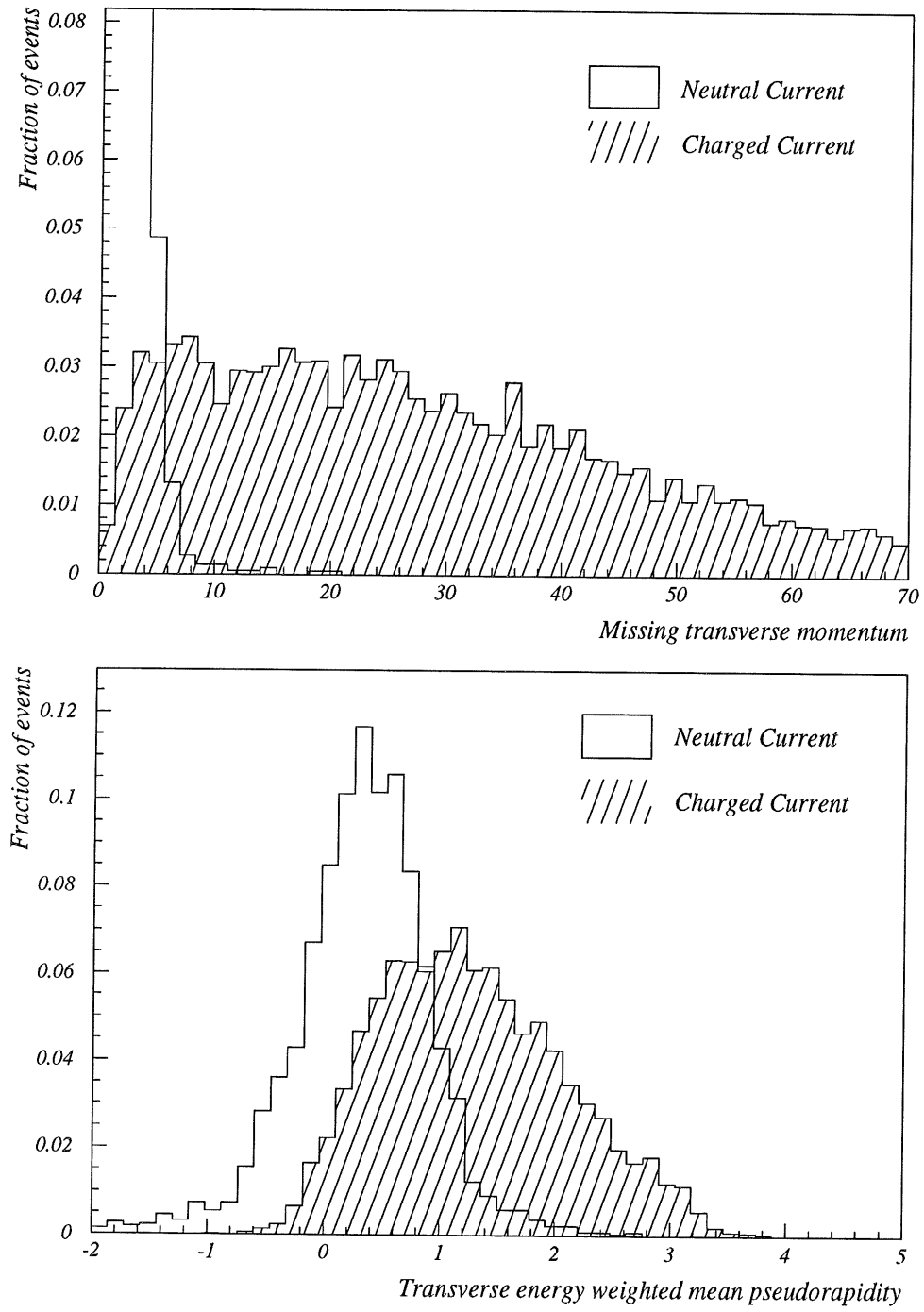


Figure 4.2: Missing transverse momentum (top) and tranverse energy-weighted mean pseudorapidity distributions for charged current and neutral current processes. These are Monte Carlo generated data using DJANGO with the MRSH proton structure function.

routine, it is preferable to work with numbers of similar order of magnitude: each missing $P_\perp$ measurement can be divided by the mean of the full data sample, reducing the size of the moments and also helping to reduce possible systematic errors in the measurements due to uncertainties in the calorimetric energy scales of the detector.

## 4.4 Event Selection

Pure samples of charged and neutral current events have been selected to test how well the matrix fitting routine can separate these processes.

For a charged current sample, the fourteen events identified in the H1 1993 data have been used. For these events, the charged current trigger is set (*ie.* they have missing transverse momentum above calorimeter thresholds and are in time with HERA bunch crossings), an interaction vertex is reconstructed and filters for cosmic or superimposed events are survived.

Neutral current events are selected in the coarse Level 5 classification by the presence of a candidate scattered electron in the detector. Additional cuts have been applied to ensure a good electron signature and a well-reconstructed $z$-vertex (the details of these data cuts can be found in the appendix): identical cuts are used for the Monte Carlo data sample so that the distributions for Monte Carlo and data are exactly comparable.

It is also known that the neutral current data include diffractive processes that are not described by existing Monte Carlo programs. It is therefore necessary to remove this component from the data for this fit. A distinctive signature of diffractive processes is a rapidity gap seen in the liquid argon calorimeter (see section 1.3), so a cut is introduced against events that exhibit such a gap. However the rapidity gap in a diffractive event may not necessarily extend into the calorimeter. In this case, the forward detectors of H1 can be used to recognise the lack of a proton remnant in the event: the plug calorimeter is usually filled by the proton remnant, while the forward muon system and the proton tagger detect secondary scattering from the remnant as it passes down the beampipe; a simultaneous lack of activity (above noise levels) in these three subdetectors implies that no proton remnant has been formed and this can be used as a cut against diffractive events (again, these cuts are detailed in the appendix).

The effect of removing diffractive events from the neutral current data sample is demonstrated for the $\overline{\eta}_{E_\perp}$ variable in figure 4.3. Events satisfying the diffractive selection criteria account for much of the low $\overline{\eta}_{E_\perp}$ shoulder of the distribution, and their exclusion will ensure a better matching of the Monte Carlo and data distributions for $\overline{\eta}_{E_\perp}$.

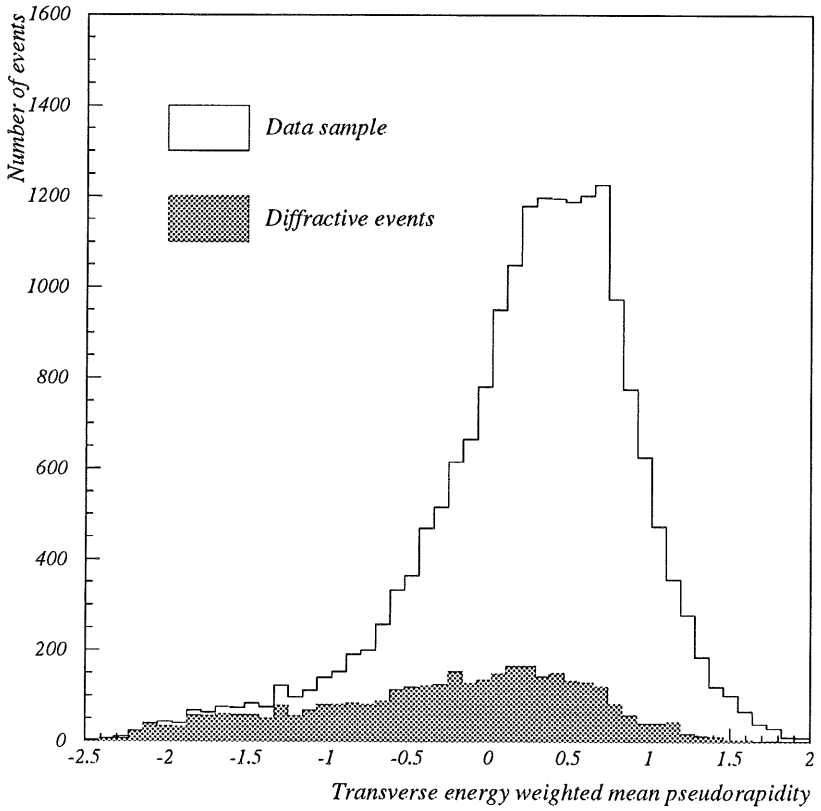


Figure 4.3: $\overline{\eta}_{E_\perp}$ distribution for the DIS data sample and for events satisfying diffractive event selection criteria.

## 4.5 Comparing Monte Carlo and H1 Data

To separate event samples using missing $P_\perp$ and $\overline{\eta}_{E_\perp}$, it is essential that the distributions of these variables as observed in H1 data are well described by Monte Carlo generated data, from which the moments for the fit will be calculated. Different models and structure functions are available for simulation of the scattering

process, as discussed in section 4.2, and so the Monte Carlo program that best describes H1 data should be selected.

Figure 4.4 compares the missing $P_\perp$ and $\overline{\eta}_{E_\perp}$ distributions of neutral current events for two Monte Carlo models. Events have been generated in the LEPTO framework using the colour dipole model (ARIADNE) and using the "matrix element + parton shower" approach (ME+PS). The distributions are compared to H1 1993 data (cuts to select neutral current and reject diffractive processes, as discussed above, have been applied to all distributions for fair comparison). Both Monte Carlo models give a reasonable description of the missing $P_\perp$ observed in neutral current events, but for $\overline{\eta}_{E_\perp}$ the ARIADNE program is in much better agreement, and so is favoured over ME+PS.

The effect of using different proton structure functions within the DJANGO (with ARIADNE) program is demonstrated in figure 4.5. The MRSD– structure function does not produce missing $P_\perp$ or $\overline{\eta}_{E_\perp}$ distributions consistent with H1 data – too much missing $P_\perp$ and a too forward $\overline{\eta}_{E_\perp}$ distribution are generated implying a poor description of the proton remnant and its fragmentation. However the MRSH structure function, actually calculated from H1 1993 data, is (not surprisingly!) in much better agreement.

Unfortunately, the charged current data sample is too small to make adequate comparisons with Monte Carlos for this process – it is assumed that the model that best describes the neutral current distributions will also give the best description of the charged current interaction. From the above comparisons, ARIADNE and the MRSH structure function within the DJANGO framework are favoured, so this Monte Carlo program has been used for all data generation.

## 4.6 Using the Fitting Routine

### 4.6.1 Monte Carlo Test

A Fortran routine has been written for the manipulation of the equations detailed in chapter 3. Matrix inversion is performed by the CERNLIB F010 routine [40], with all numbers used in double precision.

The fitting code can first be checked for errors by running a simple test: Monte

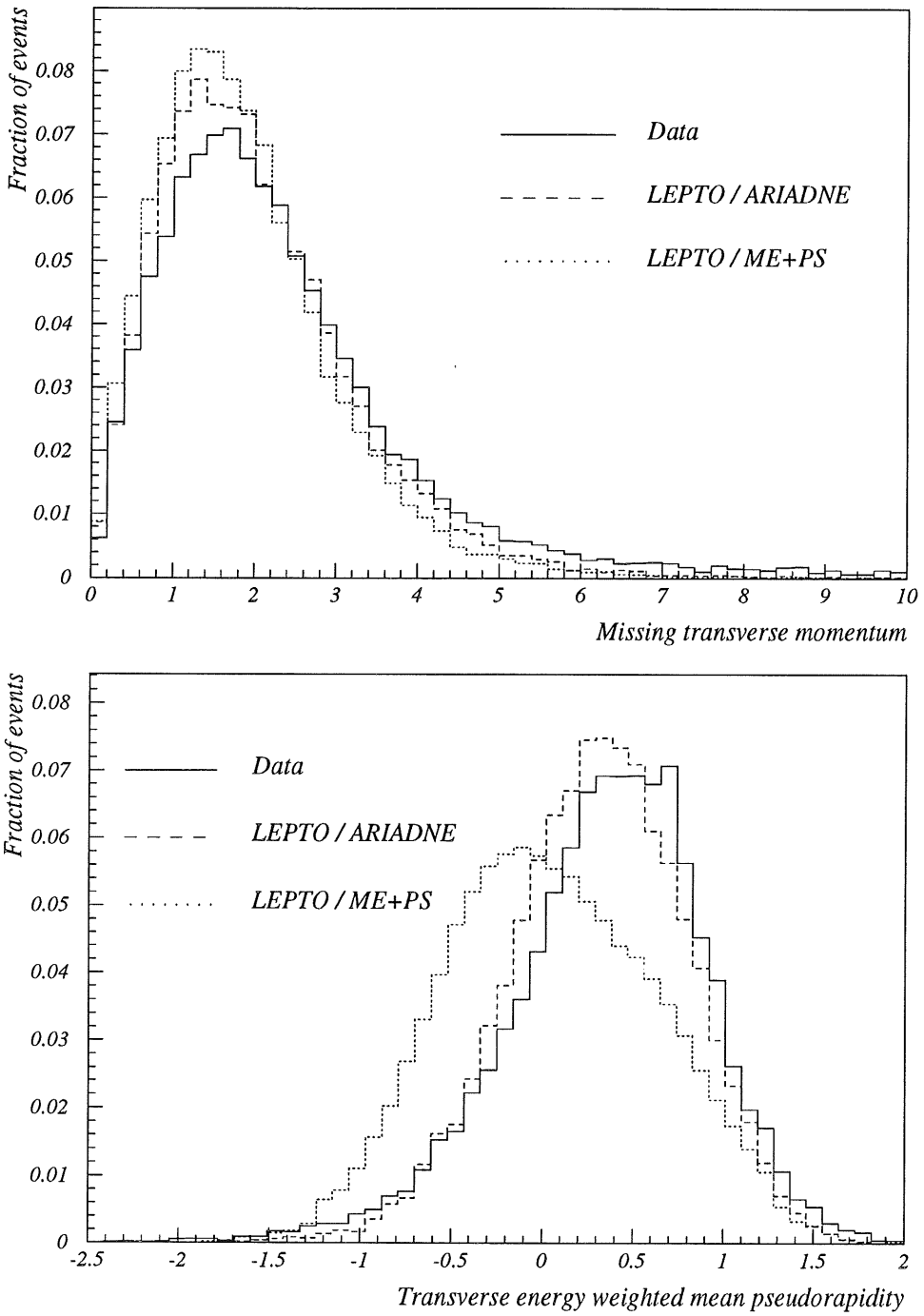


Figure 4.4: Missing transverse momentum (top) and tranverse energy-weighted mean pseudorapidity distributions for neutral current processes, comparing Monte Carlo models.

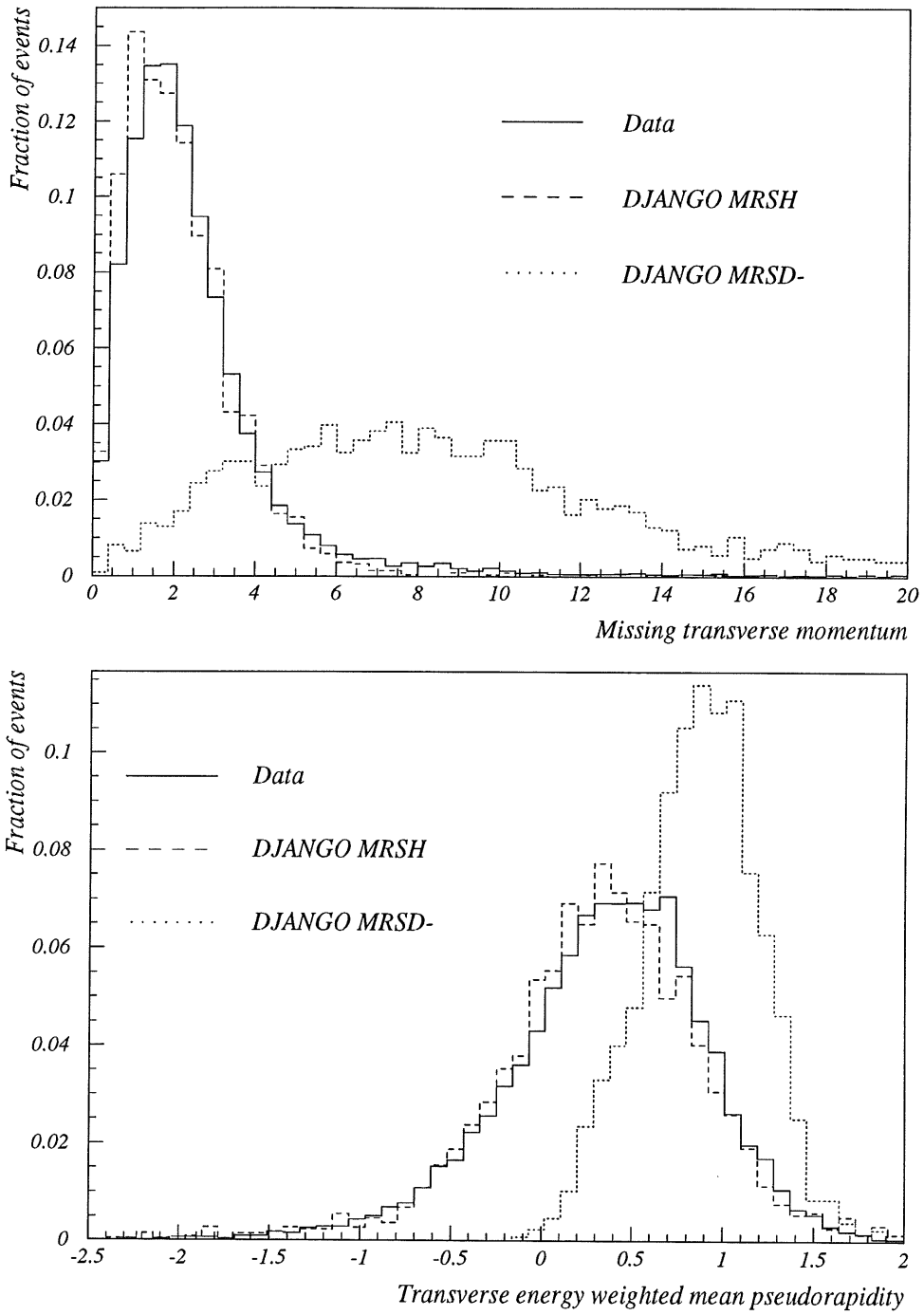


Figure 4.5: Missing transverse momentum (top) and tranverse energy-weighted mean pseudorapidity distributions for neutral current processes, comparing structure functions MRSD- and MRSDH within the DJANGO Monte Carlo program with the H1 data sample.

Carlo samples are used to calculate the moments to be used for the fit, then the *same* samples are fed into the routine for separation – the answers returned should be exactly the numbers of each process given to the routine, unless errors exist in the code.

A charged current sample of 4997 Monte Carlo events and a neutral current sample of 2200 Monte Carlo events were used to calibrate the routine. The entire sample was then fed to the separating algorithm, fitting to missing $P_\perp$ and $\overline{\eta}_{E_\perp}$. Correct answers were returned for the fraction of each class in the sample, proving that the routine is free of errors.

A few effects can be tested here, using the known Monte Carlo samples. Without using the total number of events as a constraint, a fit was performed to the first moment only of the missing $P_\perp$ and $\overline{\eta}_{E_\perp}$ distributions, giving the result

$$\begin{array}{lll} \text{CC} & 4997.022 \pm 81.965 & \\ \text{NC} & 2199.924 \pm 389.810 \qquad \text{with } \chi^2 & 1.788 \times 10^{-15}. \end{array} \tag{1}$$

The answers are almost precisely the numbers of Monte Carlo events given to the routine and the very low $\chi^2$ value is expected, compared with zero degrees of freedom for this fit (see section 3.5). If all values of missing $P_\perp$ are then normalised to the mean of the sample, the fit returns

$$\begin{array}{lll} \text{CC} & 4997.001 \pm 81.965 & \\ \text{NC} & 2200.007 \pm 389.809 \qquad \text{with } \chi^2 & 5.689 \times 10^{-20} \end{array} \tag{2}$$

– the precision of the answers improves and $\chi^2$ is even lower when smaller numbers (of order unity) are used in the matrices.

Similarly a fit can be performed using the first and second moments of the $\overline{\eta}_{E_\perp}$ distribution alone, still with zero degrees of freedom:

$$\begin{array}{lll} \text{CC} & 4997.004 \pm 75.646 & \\ \text{NC} & 2199.995 \pm 150.132 \qquad \text{with } \chi^2 & 1.748 \times 10^{-20}. \end{array} \tag{3}$$

Here, $\chi^2$ for the fit is even lower and the errors on the results have also improved. If the constraint on the total number of events is now introduced (for real data separation, it will be essential that the number of events is constrained) and the fit to two moments of $\overline{\eta}_{E_\perp}$ is repeated, the following result is obtained:

$$\begin{array}{lll} \text{CC} & 4997.002 \pm 47.647 & \\ \text{NC} & 2199.999 \pm 35.029 \qquad \text{with } \chi^2 & 3.247 \times 10^{-10}. \end{array} \tag{4}$$

Correct answers are once again returned, but notice that the errors on the results are significantly lower: there is now one degree of freedom for the fit and so it is expected that a better answer (*ie.* with smaller error margins) will be found by the routine.

Repeating the fit to missing $P_\perp$ (normalised) and $\overline{\eta}_{E_\perp}$, using two moments of each variable and including the number of events as a constraint, produces

$$\begin{array}{lll} \text{CC} & 4997.000 \pm 50.177 & \\ \text{NC} & 2200.002 \pm 77.166 \qquad \text{with } \chi^2 & 9.068 \times 10^{-9}. \end{array} \tag{5}$$

Three degrees of freedom exist for this fit and, with the additional information provided by the higher moments, a better result is obtained with reduced errors compared to the answers (2) quoted above.

### 4.6.2 Data Separation

The fitting algorithm is now applied to known samples of real H1 data, taken during the 1993 running period. Fourteen charged current events mixed with thirty neutral current events form the data sample to be separated (the selection criteria for both classes were discussed in section 4.4).

Fits have been performed to the two discriminating variables missing $P_\perp$ and $\overline{\eta}_{E_\perp}$, used individually or simultaneously, with missing $P_\perp$ always scaled by the mean of the data distribution, and the total number of events in the sample also included as a constraint. The number of variable moments used has been varied, beginning with a fit to the first moment only and then gradually extending the routine to include the first five moments of the distributions.

The results of these fits are shown graphically in figure 4.6. The input fractions of 68.2% neutral current and 31.8% charged current are marked for comparison with the values returned by the matrix fit. The error bars represent the errors calculated within the routine.

In each case, a reasonable fit has been performed using one or two moments of the variable distribution(s). However using more than two moments causes the fit to collapse – for three moments the calculated fractions begin to diverge and $\chi^2$ for the fit increases dramatically (for example, the fit to three moments of the missing $P_\perp$ and $\overline{\eta}_{E_\perp}$ distributions has a $\chi^2$ of 20.995, compared to 2 degrees of freedom); for four

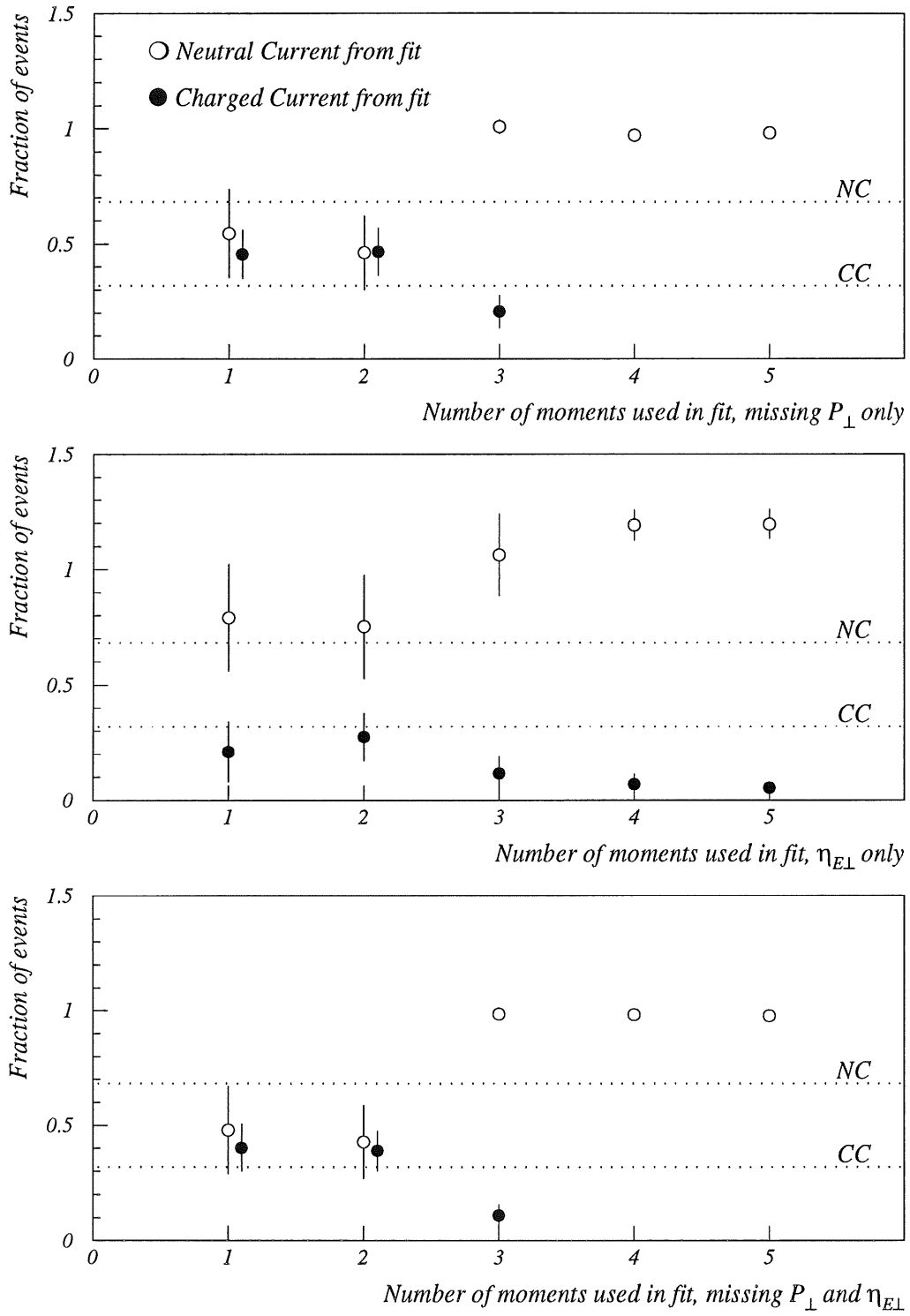


Figure 4.6: Fits to missing $P_\perp$ and $\overline{\eta}_{E_\perp}$, individually and simultaneously, using increasing numbers of moments. The dotted lines show the fractions of neutral current (NC) and charged current (CC) given as input to the routine.

moments and above, the entire sample is identified as neutral current. In fact, *more* than the entire sample is classified as neutral current: it should be remembered that the number of events in the sample is included in the fit just as any other variable – an adjustment ($\Delta$m) can be made to this total to ease the constraints on the fit; if the fit is then performed well, it is expected that this adjustment will be small, so that the sum of identified charged current and neutral current events is very close to the total number of events given to the routine.

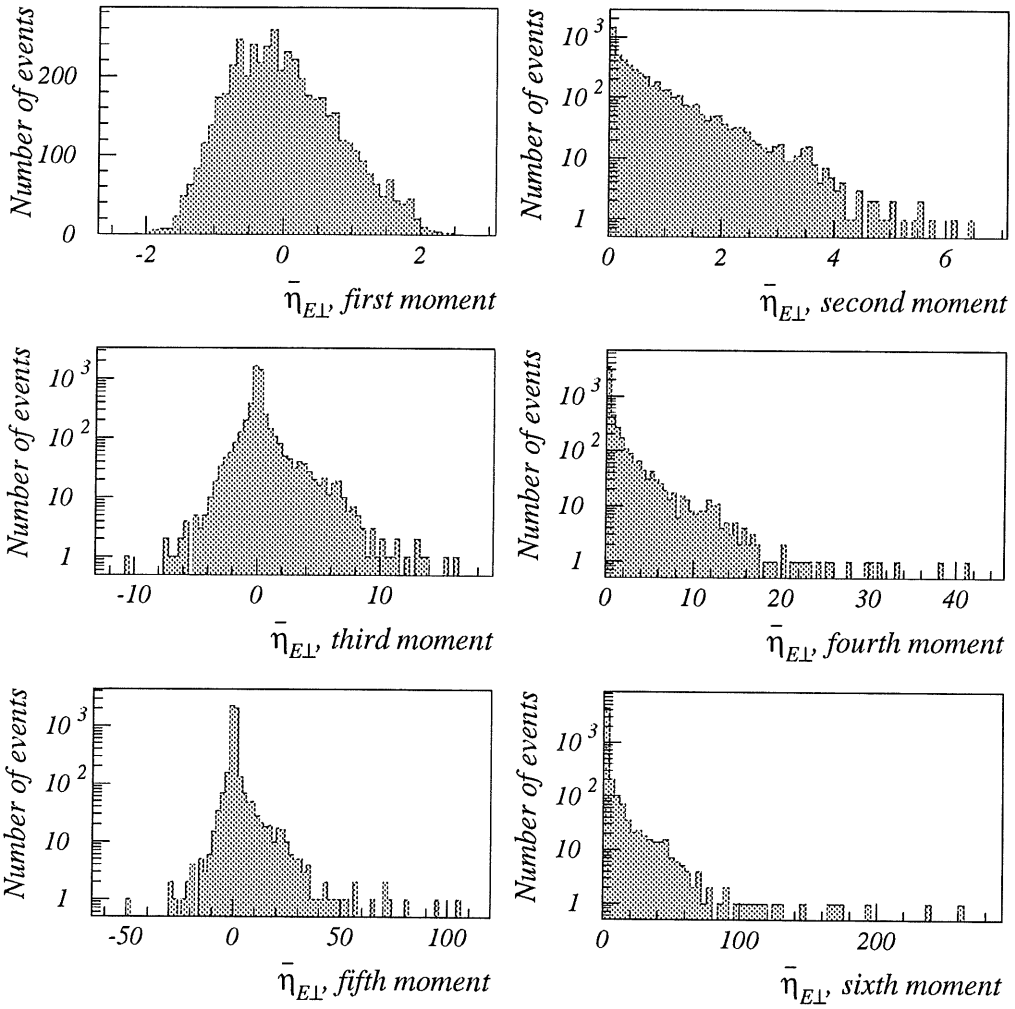


Figure 4.7: Distributions of components of successive moments of the $\overline{\eta}_{E_\perp}$ variable (for DJANGO generated data with MRSH structure function).

Figure 4.7 shows the distributions of the components summed to calculate the moments for a sample of $\overline{\eta}_{E_\perp}$ measurement: these components are the difference between the measured value and the sample mean. This difference may be large

for a value at the edge of the distribution of measurements and then raising it to ever higher powers (*ie.* calculating higher moments) will produce outlying values that distort the moment distributions, with particularly serious effect if statistics are limited. Values at significant distance from the main distribution can be seen for the third and higher moments in figure 4.7, and suggest that fits to these moments will not produce reliable results.

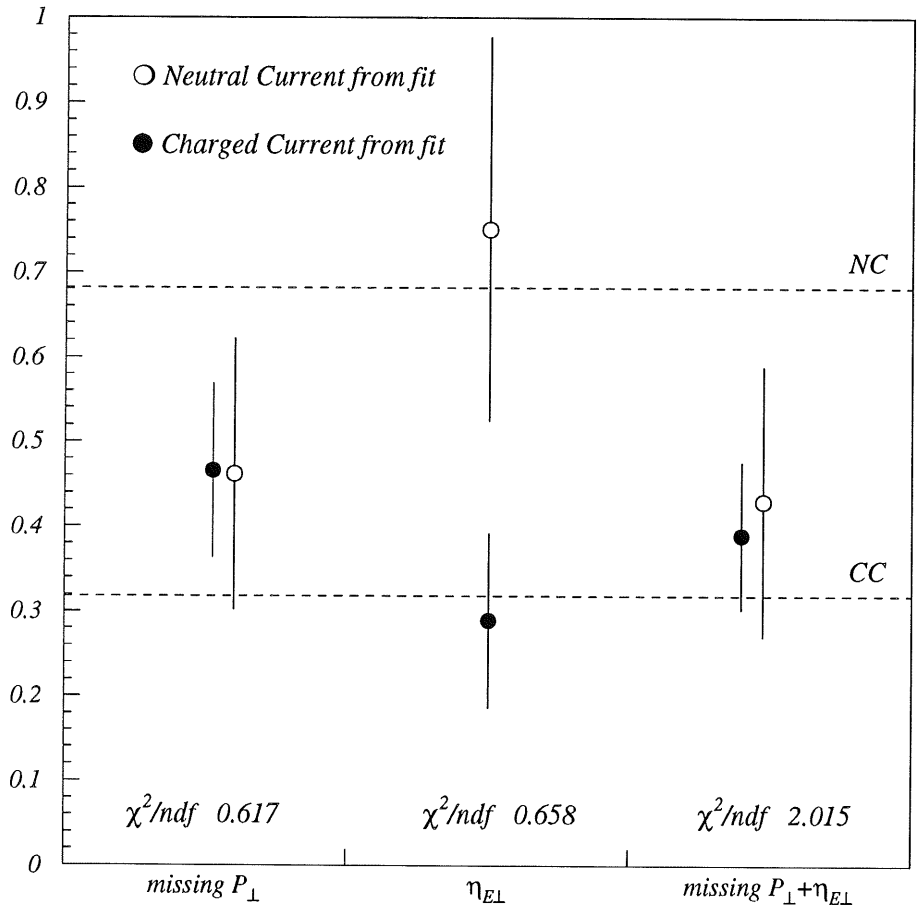


Figure 4.8: Fits to two moments only of the missing $P_\perp$ and $\overline{\eta}_{E_\perp}$ distributions, individually and simultaneously, compared to the NC/CC input (dotted lines).

Figure 4.8 offers a direct comparison of the results obtained from a fit to the first two moments of missing $P_\perp$ alone, $\overline{\eta}_{E_\perp}$ alone and then both variables simultaneously. The fit to missing $P_\perp$, although having a low $\chi^2$ per degree of freedom, is not successful: the answers are within 1.5 standard deviations of the true fractions, but

better results should be expected as the input to the routine were (pre-identified) pure samples of each class. Including two moments of $\overline{\eta}_{E_\perp}$ in this fit causes no improvement in the results and the $\chi^2$ per degree of freedom increases.

Fitting the data to two moments of the $\overline{\eta}_{E_\perp}$ distribution produces the most accurate answers, with a $\chi^2$ per degree of freedom of 0.658. Measured values of $\overline{\eta}_{E_\perp}$ must lie within the range of detector acceptance, whereas there is no upper bound on the missing $P_\perp$ measured in an event. Where statistics are limited, odd outlying vaues of missing $P_\perp$ will distort the distributions of even the low moments beyond usefulness. But as there can be no wildly outlying values of $\overline{\eta}_{E_\perp}$, the distributions of the low moments of this quantity will be more constrained and better defined. Hence $\overline{\eta}_{E_\perp}$ appears to be a more powerful variable for the discrimination of charged current processes.

# Chapter 5

# Separation of Charged Current Processes from Background

The matrix technique for statistical separation has been demonstrated, with some success, for known data samples. The method will now be applied to a "real-life" situation – the identification of charged current events in an H1 data sample, collected in the early part of the 1994 running period using electron beams.

A sample of charged current candidates exists, having passed the charged current trigger and meeting Level 5 requirements (see appendix). The missing $P_\perp$ requirement of the trigger has a very high efficiency ($94 \pm 3\,\%$ [41]) for the selection of charged current candidates if the measured missing $P_\perp$ is in excess of $25\,GeV$. Below this point, the trigger efficiency falls off steadily and so it is sensible to maintain the $25\,GeV$ cut-off in missing $P_\perp$ when handling the candidate sample.

## 5.1 Background to the Charged Current Process

Background to the charged current signal could be expected from the neutral current process, photoproduction, beamgas interactions and cosmic ray muons passing through the detector.

Monte Carlo distributions of missing $P_\perp$ for neutral current and photoproduction events were shown in figure 3.1 and are seen not to extend above $25\,GeV$, where the missing $P_\perp$ threshold for charged current candidates is set. Checking the same distributions for 1993 data, all photoproduction is certainly excluded by the $25\,GeV$

cut but some events from the neutral current sample do survive – however, they represent only 3% of the data and are believed to be consistent with contamination of the sample by beamgas events. Neutral current events are therefore considered to be excluded as a background to the charged current process, for missing $P_\perp > 25\,GeV$.

For a sample of charged current candidates above the $25\,GeV$ cut, the main background is due to beamgas interactions and cosmic ray muons: typical events are shown in figure 5.1. Beamgas interactions are caused by the presence of residual particles in the imperfect vacuum of the beampipe which may collide with beam particles, particularly protons. Showers of particles are produced from the collision and the $P_\perp$ imbalance may be sufficient to satisfy the charged current trigger. Similarly, cosmic muons entering the detector, perhaps inducing particle showers, may have a $P_\perp$ imbalance with respect to the HERA beamline that causes them to be selected as charged current candidate events.

No Monte Carlo simulations of these processes are available, but moments of distributions for use in the separation routine can be calculated from another source. For the 1994 running period, HERA is colliding 156 electron bunches with 156 proton bunches. In addition there are 12 electron bunches and 15 proton bunches in the accelerator ring that are not paired: for each unpaired electron bunch, there is no proton bunch timed to arrive at the interaction point simultaneously, and *vice versa* for the proton bunches. These are known as "pilot" bunches and should pass through the detector without colliding. However, beamgas interactions are likely to occur and so pilot bunches are useful for monitoring background levels in H1.

Triggers may be set during a pilot bunch crossing, for example if a large missing transverse energy is measured, the charged current trigger may be satisfied – events flagged as pilot bunch data do appear in the charged current candidate selection.

For some pilot bunch crossings, there is no beamgas interaction, but a cosmic muon passes through the detector in time with the crossing and so is recorded. Such events may satisfy the charged current trigger and are indeed seen in the candidate sample.

Pilot bunches account for $\sim 15\%$ of bunch crossings in H1, while $\sim 12\%$ of the events in the charged current selection have pilot bunch flags. This implies that the majority of the background to the charged current process is due to beamgas/cosmic events. The pilot bunch data will be used in place of a Monte Carlo sample as the best available description of the background.

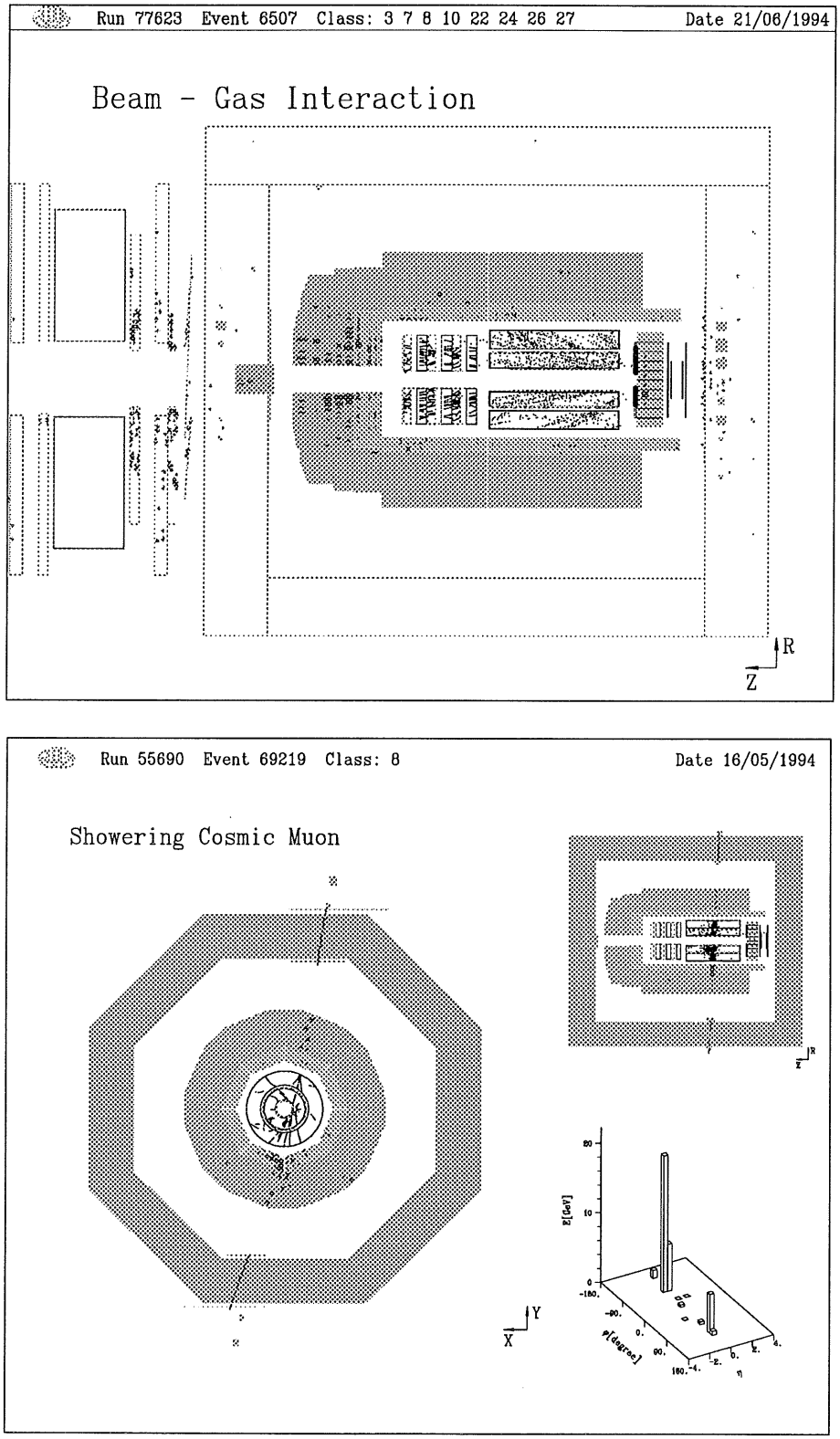


Figure 5.1: Interaction between proton and residual beamgas (top) and a cosmic ray muon seen in the H1 detector.

## 5.2 Data Selection

The sample of charged current candidates from the electron-proton running period of early 1994 numbers $\sim$ 15000 events. The number of real charged current events in this sample is expected to be small and the matrix fitting routine cannot be expected to isolate this fraction within such a large input data sample. The number of candidate events must be significantly reduced for the fit to work effectively, but if cuts are applied to the sample, it should be certain that no genuine charged current events are lost in doing so.

The first cut on the data sample is the requirement of missing $P_\perp$ for each event in excess of $25\,GeV$. Although charged current events will be lost, the cut is necessary because of trigger inefficiency below this level, but also eliminates other sources of background, such as photoproduction and neutral current events, from the sample. The remaining data are then grouped in bins of missing $P_\perp$, producing several smaller samples to each of which the separating algorithm can be applied.

The kinematic variable $y$, introduced in chapter 1, is a useful quantity for the reduction of the data samples. $y$ may be considered as the fraction of energy lost by the electron in the scattering process and can be calculated from the scattered electron itself or from the hadrons in the event: for charged current events with no scattered electron this quantity must obviously be calculated from the hadrons and is defined

$$y_{hadrons} = \frac{1}{2E_e} \sum_{hadrons} (E - P_z),$$

where $E$, $P_z$ are the energy and $z$-momentum of each hadron and $E_e$ is the electron beam energy. For DIS events, $y_{hadrons}$ is in the range $0 \rightarrow 1$, although the distribution of values is smeared slightly due to the intrinsic resolution of energy measurements.

Obviously, for non-DIS processes such as beamgas and cosmic events $y_{hadrons}$ can be calculated but has no meaningful interpretation. The value of $y_{hadrons}$ is not constrained to the $0 \rightarrow 1$ range. Figure 5.2 shows the distribution of $y_{hadrons}$ for charged current and background events. The range of values for the charged current process extends slightly above 1, while for background processes it extends very much higher. A cut-off at $y_{hadrons} = 1.5$ will safely exclude some background with no loss of charged current events.

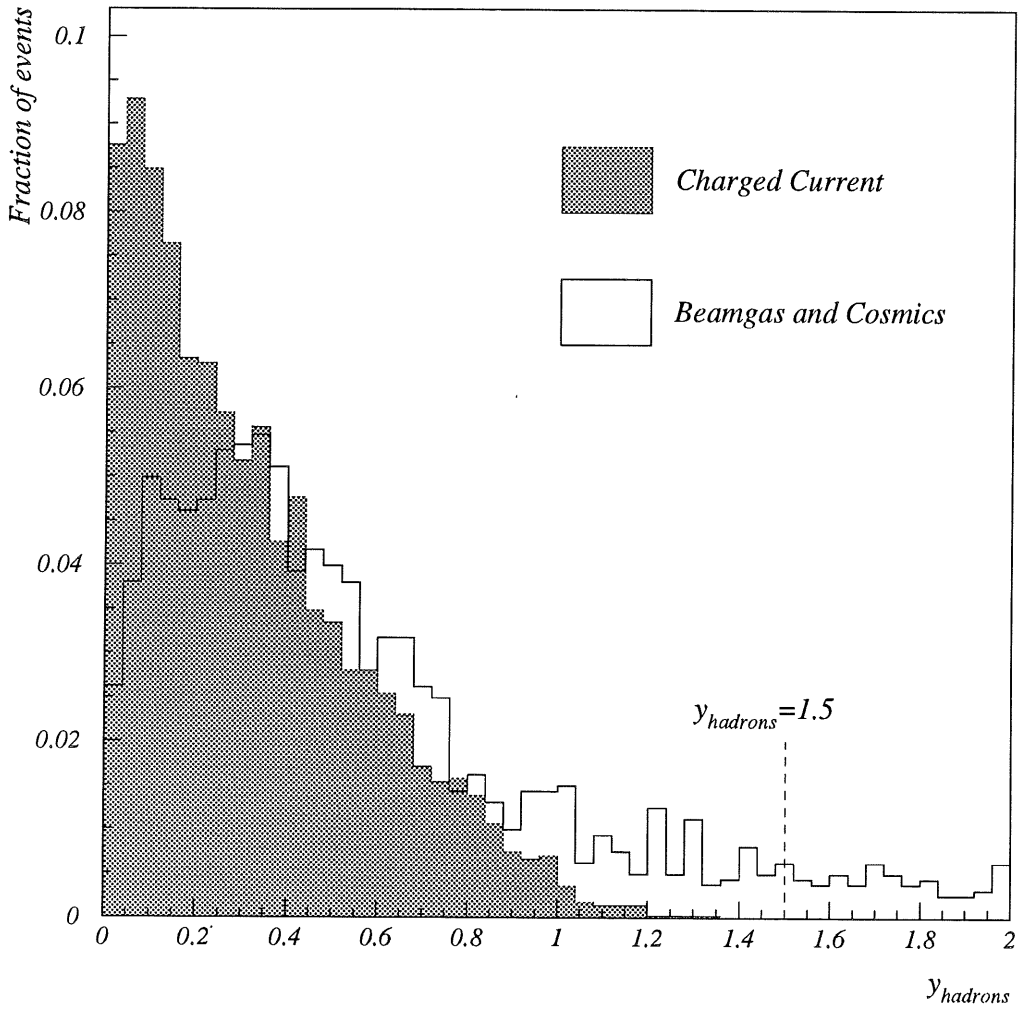


Figure 5.2: Distribution of $y_{hadrons}$ for charged current and background events.

A further effective cut against background processes can be made on the existence of a rapidity gap in the liquid argon calorimeter: this cut was used previously against diffractive events in the neutral current data sample (section 4.4). Rejecting events that exhibit a rapidity gap causes a significant reduction in the charged current candidate selection, although no effect is seen on a sample of charged current Monte Carlo events. The cut is likely to remove many cosmic events: the event shown in the lower part of figure 5.1 has the typical cosmic signature of a track passing completely through the detector and also exhibits a lack of activity in the forward region where the proton remnant would usually be seen.

The effect of the rapidity gap cut on the size of the data sample is shown, in bins of missing $P_\perp$, in figure 5.3: the sample is drastically reduced and is reduced still further by the application of the $y_{hadrons}$ cut. But neither cut rejects any charged current events from a Monte Carlo sample, and so can be confidently applied to the charged current candidate selection for the reduction of the background signal alone.

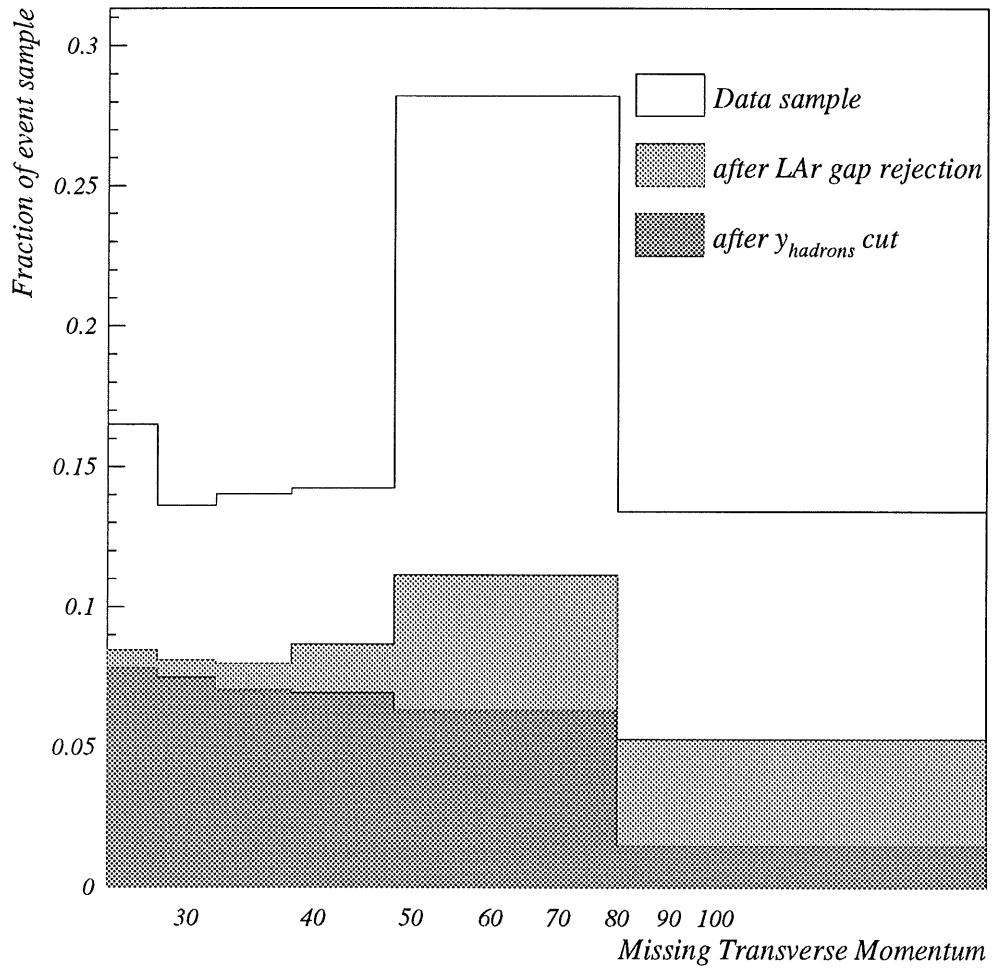


Figure 5.3: The reduction of the charged current candidate sample by application of the rapidity gap cut, then a cut on $y_{hadrons}$.

However, it should be remembered that the background "Monte Carlo" for calibration of the matrix routine is actually taken from pilot bunch events within this data sample – cutting the data reduces the statistics available to describe the back-

ground distributions. A comparison of the Monte Carlo statistics for charged current events and background processes (after cuts) is shown in figure 5.4: the background statistics are very low and may limit how well the matrix separation of processes can be performed.

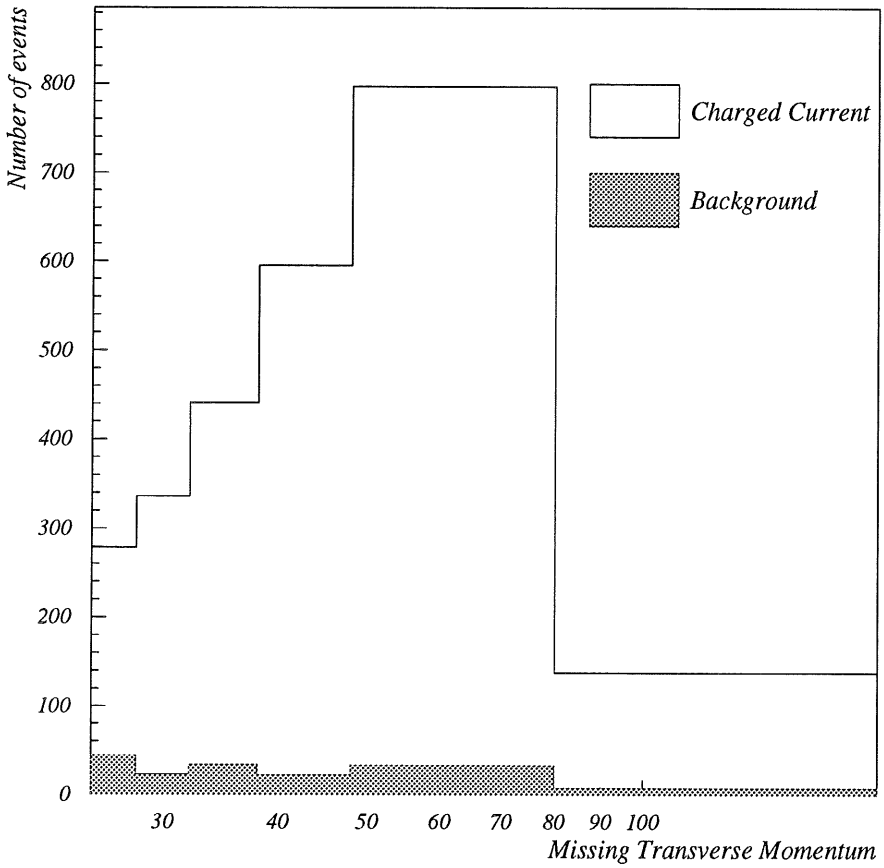


Figure 5.4: Monte Carlo events for the calibration of the matrix fitting routine, shown for charged current and background processes (the "Monte Carlo" data for background processes is actually pilot bunch information).

## 5.3 Variables and Moments

Missing $P_\perp$ is no longer available as a discriminating variable between charged current and background processes – after a cut is applied at missing $P_\perp = 25\,GeV$, the remaining data are binned in missing $P_\perp$, destroying the discriminating shape of the

distribution for each process.

The kinematic variable, $y_{hadrons}$ (distributions of which were shown in figure 5.2) is not a powerful discriminant between the processes – the distribution shapes are too similar and $y_{hadrons}$ is actually more effectively used as a cut against background processes which dominate the sample for $y_{hadrons} > 1.5$.

The quantity $\overline{\eta}_{E_\perp}$ has already been shown to be an effective discriminating variable between neutral and charged current events. The distributions of this variable for charged current and background processes (compared in figure 5.5) are also suitably distinct. The $\overline{\eta}_{E_\perp}$ distribution for the background sample is centred around $\overline{\eta}_{E_\perp} = 0$, tailing off into the forward region, reflecting the random distribution of particles produced in cosmic events and the only very slight forward bias of beamgas interactions. The collimated jet structure produced in the DIS process and dominated by the forward-going proton remnant causes $\overline{\eta}_{E_\perp}$ for charged current events to be distributed over more forward values.

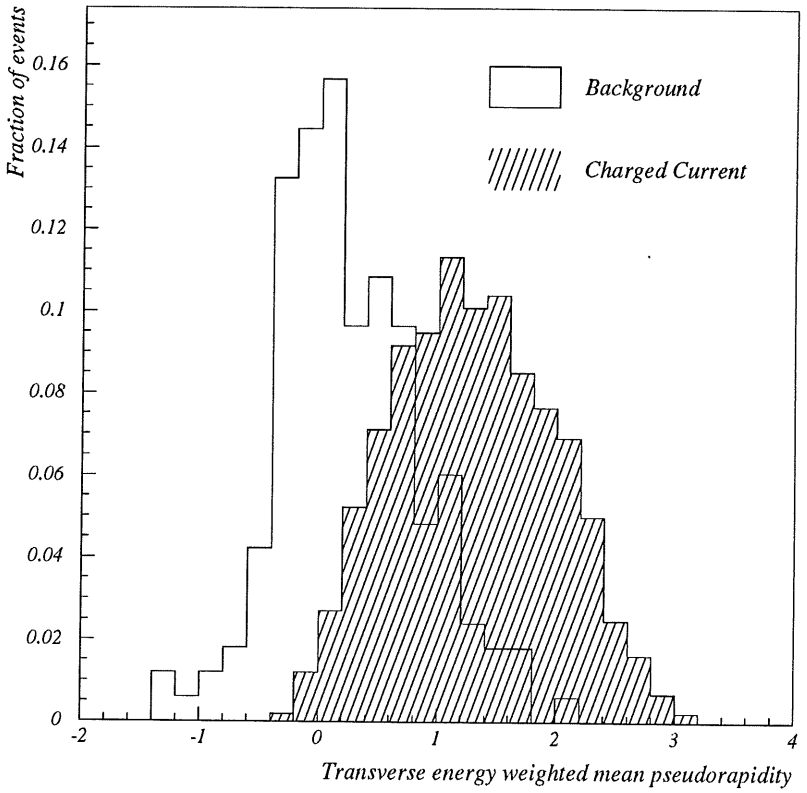


Figure 5.5: $\overline{\eta}_{E_\perp}$ distributions for the charged current and background processes.

As was seen in the separation of neutral and charged current samples (section 4.6.2), it is not feasible to fit to higher moments of the variable distributions. Particularly for this background separation, the Monte Carlo statistics are low and higher moments will not be well defined. Experience with the neutral/charged current separation indicates that a fit to two moments of the $\overline{\eta}_{E_\perp}$ variable distribution may produce the best results.

## 5.4 Result of Fit

The charged current candidate sample has been fitted, in bins of missing $P_\perp$, to the first and second moments of the $\overline{\eta}_{E_\perp}$ distributions for charged current and background processes. The results, with errors returned by the fit, are listed in table 5.1. The $\chi^2$ value for each fit is also given and should be compared to one degree of freedom.

| | Missing $P_\perp$ bins | Charged Current | Background | $\chi^2$ |
|---|---|---|---|---|
| 1 | $25 \leq$ missing $P_\perp < 28\,GeV$ | $57.989 \pm 10.273$ | $231.927 \pm 15.546$ | 11.539 |
| 2 | $28 \leq$ missing $P_\perp < 32\,GeV$ | $70.729 \pm 10.305$ | $223.167 \pm 14.789$ | 5.570 |
| 3 | $32 \leq$ missing $P_\perp < 38\,GeV$ | $18.591 \pm 11.250$ | $300.467 \pm 18.458$ | 0.0378 |
| 4 | $38 \leq$ missing $P_\perp < 48\,GeV$ | $69.384 \pm 9.581$ | $194.544 \pm 11.995$ | 7.336 |
| 5 | $48 \leq$ missing $P_\perp < 80\,GeV$ | $14.112 \pm 10.995$ | $252.298 \pm 14.441$ | 1.038 |
| 6 | $80 \leq$ missing $P_\perp < 180\,GeV$ | $38.651 \pm 3.068$ | $17.705 \pm 2.967$ | 1.718 |

Table 5.1: Results of fits in bins of missing $P_\perp$ to the first and second moments of the $\overline{\eta}_{E_\perp}$ distributions, separating charged current and background processes.

The results are also shown graphically in figure 5.6. Fits have been achieved in each bin, but the sum of events in each class is not very close to the actual event total given to the routine (*ie.* the $\Delta m$ adjustments made to the total number of events are quite large, sometimes up to 20% of the event total). The $\chi^2$ values of the fits vary considerably, reflecting an instability of the fit across the missing $P_\perp$ bins that is disappointing.

The results of a fit to three moments of the $\overline{\eta}_{E_\perp}$ distribution are given in table 5.2. The deterioration of each fit is obvious: in most bins the number of events in each class changes significantly and the $\chi^2$ values, though now compared to two degrees of freedom, are much larger. The lack of statistics to define the higher variable

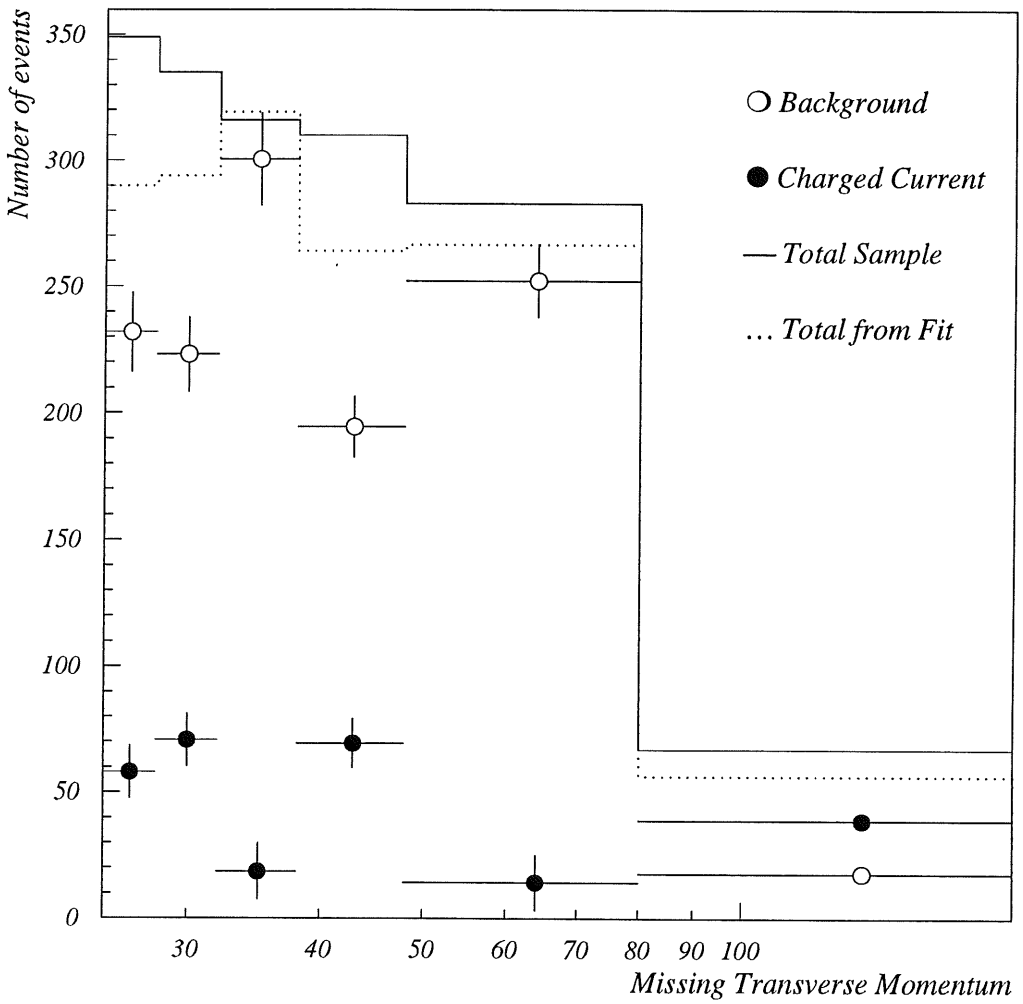


Figure 5.6: Charged current and background samples separated by the fitting algorithm using two moments of the $\overline{\eta}_{E_\perp}$ distribution. The total number of events given to the fit (solid line) and the sum of events in both classes returned by the fit (dotted line) are also indicated.

moments is indeed a strongly limiting factor in the efficacy of the matrix fitting method.

| | Missing $P_\perp$ bins | Charged Current | Background | $\chi^2$ |
|---|---|---|---|---|
| 1 | $25 \leq$ missing $P_\perp < 28\,GeV$ | $60.248 \pm 5.541$ | $228.737 \pm 9.613$ | 11.608 |
| 2 | $28 \leq$ missing $P_\perp < 32\,GeV$ | $91.879 \pm 5.561$ | $195.195 \pm 9.332$ | 11.695 |
| 3 | $32 \leq$ missing $P_\perp < 38\,GeV$ | $11.535 \pm 9.122$ | $311.651 \pm 15.226$ | 1.187 |
| 4 | $38 \leq$ missing $P_\perp < 48\,GeV$ | $98.406 \pm 6.484$ | $158.531 \pm 8.202$ | 24.265 |
| 5 | $48 \leq$ missing $P_\perp < 80\,GeV$ | $24.912 \pm 10.068$ | $241.531 \pm 13.753$ | 7.018 |
| 6 | $80 \leq$ missing $P_\perp < 180\,GeV$ | $48.559 \pm 1.450$ | $8.252 \pm 1.466$ | 15.154 |

Table 5.2: Results of fits in bins of missing $P_\perp$ to the first three moments of the $\overline{\eta}_{E_\perp}$ distributions.

In fact, for the statistics currently available, even the second moment for each class is not well-defined: for example, in the highest missing $P_\perp$ bin the background distribution is modelled by only eight events (see figure 5.4). So the best separation of the charged current sample can be expected from a fit to the first moment (mean) alone. Here there are no degrees of freedom so $\chi^2$ and the $\Delta m$ adjustments are necessarily zero. The results of this fit are given in table 5.3.

| | Missing $P_\perp$ bins | Charged Current | Background | $\chi^2$ |
|---|---|---|---|---|
| 1 | $25 \leq$ missing $P_\perp < 28\,GeV$ | $62.227 \pm 10.065$ | $286.773 \pm 22.984$ | 0. |
| 2 | $28 \leq$ missing $P_\perp < 32\,GeV$ | $57.360 \pm 11.075$ | $277.640 \pm 23.521$ | 0. |
| 3 | $32 \leq$ missing $P_\perp < 38\,GeV$ | $41.972 \pm 9.898$ | $274.028 \pm 22.691$ | 0. |
| 4 | $38 \leq$ missing $P_\perp < 48\,GeV$ | $59.710 \pm 10.067$ | $250.290 \pm 23.021$ | 0. |
| 5 | $48 \leq$ missing $P_\perp < 80\,GeV$ | $57.528 \pm 9.051$ | $225.472 \pm 122.955$ | 0. |
| 6 | $80 \leq$ missing $P_\perp < 180\,GeV$ | $24.939 \pm 7.521$ | $42.061 \pm 15.044$ | 0. |

Table 5.3: Results of fits in bins of missing $P_\perp$ to the first moment only of the $\overline{\eta}_{E_\perp}$ distributions.

Attempts were made to compensate for the lack of statistics by smoothing the means and variances of the distributions across the missing $P_\perp$ bins. From bin to bin the variance is expected to be approximately constant, whereas the mean value may show a gradual increase, reflecting the slight correlation between missing $P_\perp$ and $\overline{\eta}_{E_\perp}$. However, particularly for the background sample, quite dramatic variations in these moments occur. A straight line was fitted through these values by the least squares method and then new values for the means and variances taken from this line at each bin centre. However when fits were performed to one then two of these

smoothed moments the $\chi^2$ values and $\Delta m$ adjustments remain large – the statistics are too poor even to allow an improved description of each class by smoothing the moment variation.

To increase the statistics available, fits were also performed using fewer missing $P_\perp$ bins or across all the data simultaneously. Unfortunately the routine struggled to separate the genuine charged current events from the increased background sample: such large $\chi^2$ values were returned that these fits could not be accepted.

It is valuable to compare the results of the matrix fit with a charged current sample isolated by conventional methods of cutting and scanning. A sample of 20 charged current events exists for the 1994 electron data that has been identified by applying cuts in missing $P_\perp$ and against cosmic and beamgas events and then scanning the event pictures by eye to remove any residual background. The distributions of events in bins of missing $P_\perp$ found by the matrix method, fitting to a single moment, and by the cut/scan method are shown in figure 5.7. Note that the matrix fit method finds more charged current events than the cut/scan method – this is as expected, as genuine events may be lost in harsh data cuts.

The results are compared to the missing $P_\perp$ distribution of Monte Carlo generated events, in each case normalised to the total number of events found by the selection procedure. The distribution of identified charged current events should follow the overall shape of the Monte Carlo distribution. This is not true for the matrix fit results, but the sample isolated through cuts and scanning does reasonably reproduce the distribution, within the $\sqrt{N}$ errors placed on each point.

## 5.5 Discussion

The separation of charged current events from background has been performed, with best results produced by a fit to the first moment alone. When compared to the expected distribution of events in missing $P_\perp$ from Monte Carlo generated data, the results from the matrix fit are not fully consistent. But the usual selection procedure of cuts and scanning does reproduce the Monte Carlo distribution expected. However, it would be unfair to dismiss the matrix fitting technique at this point: its power is currently severely limited by the lack of statistics available for calibration of the routine and hence restricting the number of moments that can reasonably be used in the fit.

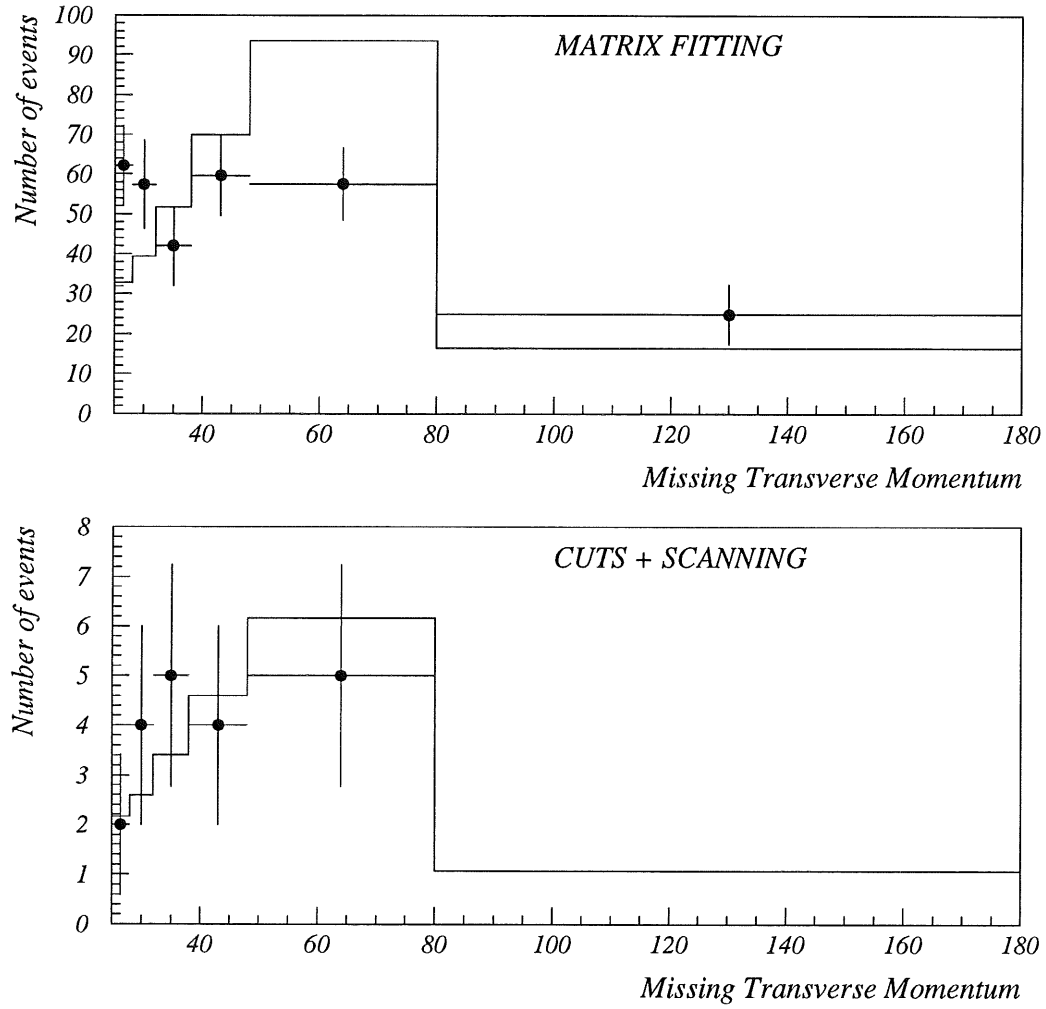


Figure 5.7: Comparison of number of CC events found by matrix fitting technique (upper plot) to number found by conventional cuts and scanning methods (lower plot). The solid line shows the normalised Monte Carlo distribution of events across the missing $P_\perp$ bins.

Also only one discriminating variable has been used to produce these results. Obviously more variables should be included but it is hard to find suitable quantities, whose distributions are distinct for the two classes to be separated. It would seem natural to go beyond pure energy flow measurements and perhaps apply jet-finding algorithms or boost to the hadronic centre of mass system (here defined with respect to the direction of the missing $P_\perp$ vector of the event rather than the scattered electron) to look for further discriminating variables. These extra levels of complication will however cause greater uncertainty in measurements made and jet algorithms or boosts applied to background processes are anyway physically meaningless.

In contrast, the matrix fitting technique has been applied successfully to the physics of electron-positron ($e^+e^-$) collisions – events where the annihilation results in the production of a $b\bar{b}$ quark pair were separated in bins across the polar angle ($\theta$) and a measurement of the forward-backward asymmetry for this quark flavour could be made [29]. The collision of two fundamental, point-like particles ($e^+, e^-$) is much "cleaner" physics than that seen in $ep$ collisions and so the different physics processes may be more easily discriminated.

The fits to measure the $b\bar{b}$ asymmetry also utilised additional constraints: some backgrounds to the process have symmetric distributions across the polar angle $\theta$, centred at $\theta = 90°$. The number of events of such a class found by the separation in the bin at $\theta = 0°$ should then be equal to the number of events found in the bin at $\theta = 180°$, and similarly for all opposite bins throughout the $\theta$ range: this information can be used as constraints for the fit (the exact procedure for incorporation of these constraints is detailed in reference [29]).

In $ep$ physics, similar symmetry constraints could be applied to the separation of boson gluon fusion events (see section 1.2): a sample of 2+1 jet events will contain a significant background to the this process due to QCD Compton events, where the quark involved in the scattering radiates a gluon and two jets are formed in the final state. When viewed in the hadronic centre of mass system, the distribution in $\phi$ of the two back-to-back jets for both processes is not uniform, an "azimuthal asymmetry" exists [42]. The quark and antiquark jets produced by boson gluon fusion follow a $cos2\phi$ distribution, while the Compton quark and gluon jets follow a $cos\phi$ distribution. So constraints could be imposed to ensure that the event fractions separated by the routine do reproduce these $\phi$ distributions. However, as yet the $\phi$ asymmetry (and hence the boson gluon fusion and QCD Compton processes) is not correctly described in the DIS Monte Carlo generators, and attempts to discrimi-

nate boson gluon fusion from background by the matrix fitting technique have been unsuccessful.

Although only very limited success of the classification method for $ep$ physics can be reported, the HERA experiments are as yet at an early stage: throughout the subsequent data-taking periods a better understanding of the H1 detector will develop, Monte Carlo modelling of the interactions will improve and, of course, the statistics available for all physics studies will greatly increase.

# Chapter 6

# The Resistive Plate Chamber

## 6.1 Introduction

In this final chapter, the development of a Resistive Plate Chamber (RPC) at the University of Manchester is reported. The RPC is a particle detector capable of very fast time resolution and is proposed as a muon triggering device for experiments at CERN's Large Hadron Collider (LHC).

The LHC, due to come into operation around the turn of the century, will collide two proton beams at a centre of mass energy of almost $16\,TeV$. It will be built in the existing LEP tunnel ($27\,km$ in circumference), thereby reducing expenditure, but requiring the latest superconducting magnet technology to achieve the design proton energies. The LHC is expected to operate at very high luminosities ($\sim 1.7 \times 10^{34} cm^{-2} s^{-1}$, compared to the HERA design luminosity of $1.5 \times 10^{31} cm^{-2} s^{-1}$), so effective triggering for physics processes is essential.

The physics potential of the LHC is high: in particular, the Higgs boson, if it is sufficiently massive to escape detection at LEP, may be found there; although the Higgs mechanism is a vital component of the Standard Model, no predictions are made about the mass or number of Higgs bosons (the simplest model of the Higgs sector has a single boson, H). Possible muon signatures of the Higgs boson are:

$$H \rightarrow Z\,Z^* \rightarrow e\,e\,\mu\,\mu \;\; \underline{or} \;\; \mu\,\mu\,\mu\,\mu, \quad for \;\; 130\,GeV < m_H < 2m_Z,$$

$$H \rightarrow Z\,Z \rightarrow \mu\,\mu\,\nu\,\overline{\nu}, \quad for \;\; 2m_Z < m_H < 800\,GeV,$$

$$H \rightarrow W\,W, Z\,Z \rightarrow \mu\,\mu\,\nu\,\overline{\nu} \;\; \underline{or} \;\; \mu\,\overline{\nu} + 2\;jets, \quad for \;\; m_H \leq 1TeV,$$

where $m_H$ and $m_Z$ are the Higgs and $Z$ boson masses, respectively.

Following its discovery at the Tevatron accelerator [43], further studies of the top quark will also be possible at the LHC. A distinctive muon signature of top quark production is

$$t\bar{t} \rightarrow W\,b\,W\,b \rightarrow e\,\nu\,\mu\,\nu \quad \underline{or} \quad \mu\,\mu\,\nu\,\nu.$$

Two experiments have been designed for the LHC: the CMS and ATLAS detectors [44, 45] both include planes of RPC detectors for muon triggering, mainly in the central (barrel) region of each detector where high efficiency can be maintained in particle fluxes of up to $100\,Hz\,cm^{-2}$.

## 6.2 Chamber Design and Operation

The RPC consists of two parallel plates of resistive material, usually Bakelite. A cross-section of the chamber is shown in figure 6.1. The plates are separated by a narrow gap of the order of $1-2\,mm$, which is maintained by the insertion of several small PVC spacers. With the edges of the chamber sealed, gas at atmospheric pressure is allowed to flow between the plates.

The outside surface of each bakelite plate is coated with a layer of graphite. A high voltage supply is connected across the two conductive layers to provide the electric field across the chamber. An insulating layer of PVC is placed over the graphite and above this are the metallic readout strips, usually copper or aluminium. The parallel strips above the chamber are orthogonal to the ones below to allow $xy$ resolution.

The RPC operates as a normal drift chamber: charged particles crossing the chamber cause ionisation of the gas and an electron avalanche develops in the direction of the anode plate; charge is displaced in the metal readout strips and the signal is registered.

The gas mixture inside the chamber is chosen to have the properties of high gain, fast recovery and low field operation [46]. Avalanche multiplication occurs in noble gases at much lower fields than other gases and so argon is often chosen as the principal component of the chamber gas. Quenching agents are also needed: a positive argon ion at the cathode can extract an electron from the surface, these recom-

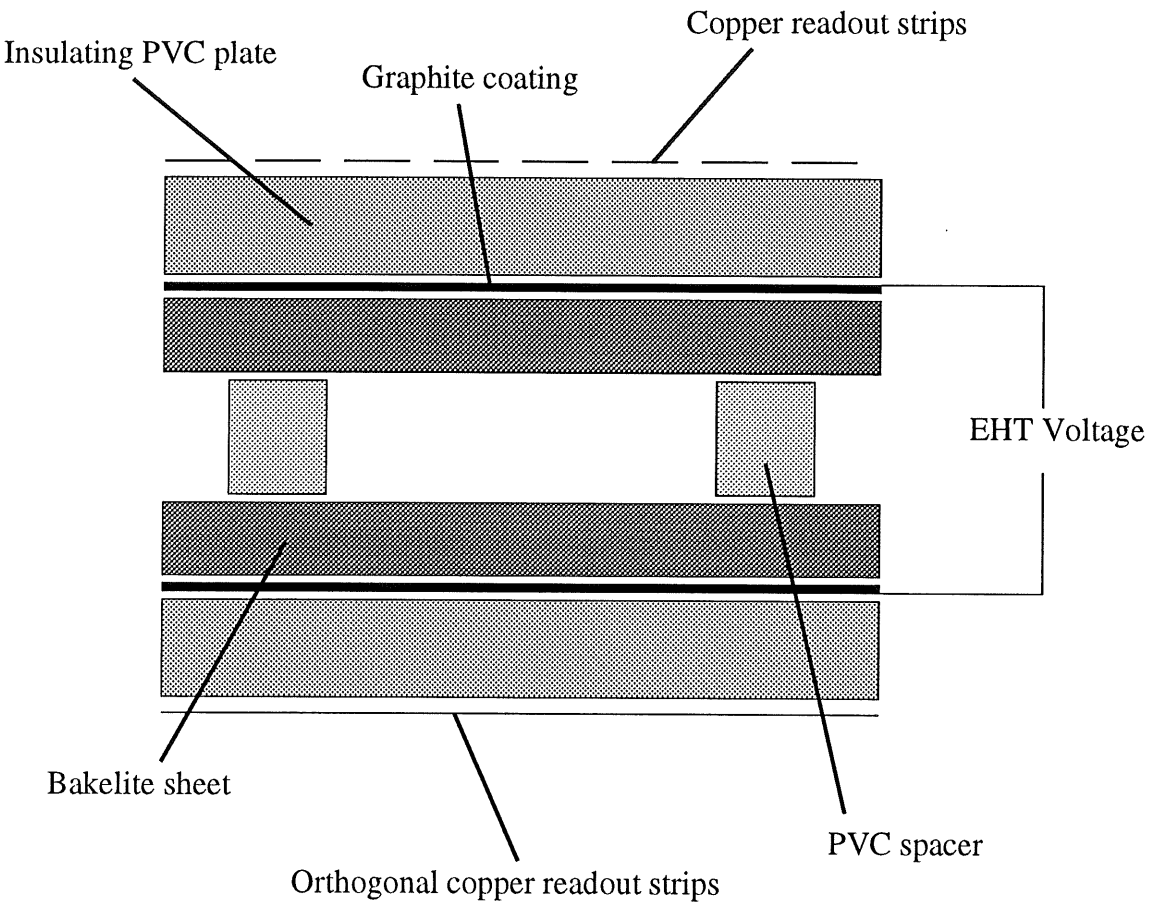


Figure 6.1: Cross-section of the Resistive Plate Chamber.

bine and a photon is emitted of sufficient energy to extract a second electron from the cathode surface; the photoelectron can then initiate a spurious avalanche. Many such avalanches may occur and the chamber will discharge continuously. Polyatomic molecules are introduced which absorb photons over a wide energy range to form non-radiative excited states, whose energy can be dissipated either by collision or dissociation. Isobutane is a common choice of quenching agent as it absorbs photons over an energy range that includes the photons emitted by argon molecules.

Small quantities of electronegative gas are also added, to achieve the highest possible gain before saturation, and offering additional photon quenching. In particular, such a gas can capture free electrons from the periphery of an avalanche, reducing its transverse size and improving the chamber resolution. The negative ions formed cannot induce avalanches at normal field values. For the RPC, the electronegative gas Freon 13B1 ($CBrF_3$) has been included in the mixture, but its use has since

been banned by the Montreal convention for the protection of the ozone layer [47].

The RPC may also operate in limited streamer mode [48]. Here, the electron avalanche develops in the usual way, but the electron number grows to such an extent that a significant space charge concentration is produced. The space charge field is large and partially cancels the applied electric field. The electrons are now in a region of low field and radiative recombinations of argon ions and electrons may occur. The energetic photons can reach outside the space charge cloud and produce electrons from the surrounding gas. These drift back and multiply at the tip of the positive ion cone, where the field is highest. The streamer grows in the direction of the cathode. Charge is drawn out of the anode, but, as this is a resistive plate, only a limited amount of charge is drawn. A signal is registered, but no spark is generated so the rest of the chamber around the streamer remains sensitive to any new avalanches.

Evidence of limited streamer operation may be seen in the very fast risetime of the chamber signal, and in the size of the pulse: at lower applied voltages, the chamber operates in proportional mode, but as the voltage is increased the chamber enters limited streamer mode and a marked increase in the pulse size is seen. This distinctive transition is sought as a signature of limited streamer operation.

The suitability of the RPC as a muon trigger in a high-rate experiment is easily seen: the large, fast-developing pulse from the chamber can be read out using simple electronics with no need for amplification, so the chamber signal is registered very quickly; and as only a small area of the detector around the streamer is disabled, the chamber has minimal deadtime.

RPC development began in the early 1980s and a $1\,ns$ time resolution and 97% efficiency were reported [49]. Limited streamer operation was first achieved in 1988 using an argon/butane gas mixture (2/3 : 1/3) with a small amount of freon and an electric field strength of $40-45\,kV\,cm^{-1}$ [50]. After the arrival of a limited streamer, a dead time of $10\,ms$ over an area $0.1\,cm^2$ was measured.

The response of the RPC at high flux has been studied, with a view to its use in LHC experiments. Tests in a pion beam at CERN have maintained an efficiency of 85% up to a beam flux of $100\,Hz\,cm^{-2}$ [51]. The E771 experiment at FNAL first used the RPC as a muon trigger. With limited streamer operation, an efficiency of 90% up to $140\,Hz\,cm^{-2}$ in a proton beam was achieved [52].

The most recently reported tests of the RPC as a muon trigger are by the RD5 experiment at CERN. Here, chambers of dimensions $2\,m \times 2\,m$ have been constructed, with 64 aluminium readout strips of $31\,mm$ pitch. The $2\,mm$ gas gap is filled with 58% argon, 38% isobutane and 4% freon. At an operating voltage of $7.1\,kV$, an efficiency of 96% is claimed, with an *rms* space resolution of $8\,mm$ [53]. Also an efficiency greater than 90% has been maintained up to $100\,Hz\,cm^{-2}$ in a muon beam.

## 6.3 RPC Development at Manchester

### 6.3.1 The RPC

The chamber used in these studies was made with two sheets of bakelite, each $1.46\,mm$ thick. Printed circuit board spacers of $\sim 1\,cm$ diameter maintain the gas gap at $1.57\,mm$, while the edges of the chamber are sealed with silicon rubber. The chamber has dimensions $40\,cm \times 40\,cm$. Copper readout strips are etched on the top surface only, covering an area $28\,cm \times 28\,cm$. The strip width is $8\,mm$, with a $2\,mm$ gap between neighbouring strips, *ie.* the pitch is $1\,cm$. Eight strips only were used in experimental work, forming an active area of $28\,cm \times 8\,cm$.

A gas mixture of 60.6% argon, 30.3% isobutane and 9.1% freon 13B1 at atmospheric pressure was used.

### 6.3.2 Readout System

The RPC was set up in a basement laboratory for testing in the cosmic muon flux [54]. An electronic readout system was established: its design is shown schematically in figure 6.2.

To study chamber response, a triggering system for the RPC readout was needed. Two plastic scintillators each of area $30\,cm \times 10\,cm$ (approximately matching the active area of the chamber) were positioned one above and one below the chamber – then a coincidence of signals from these scintillators implies that an ionising particle has traversed the RPC and a signal should be expected.

The scintillators were "plateau-ed" before tests began, to achieve steady counting rates. Once in operation, cosmic muon signals from the scintillators were passed first

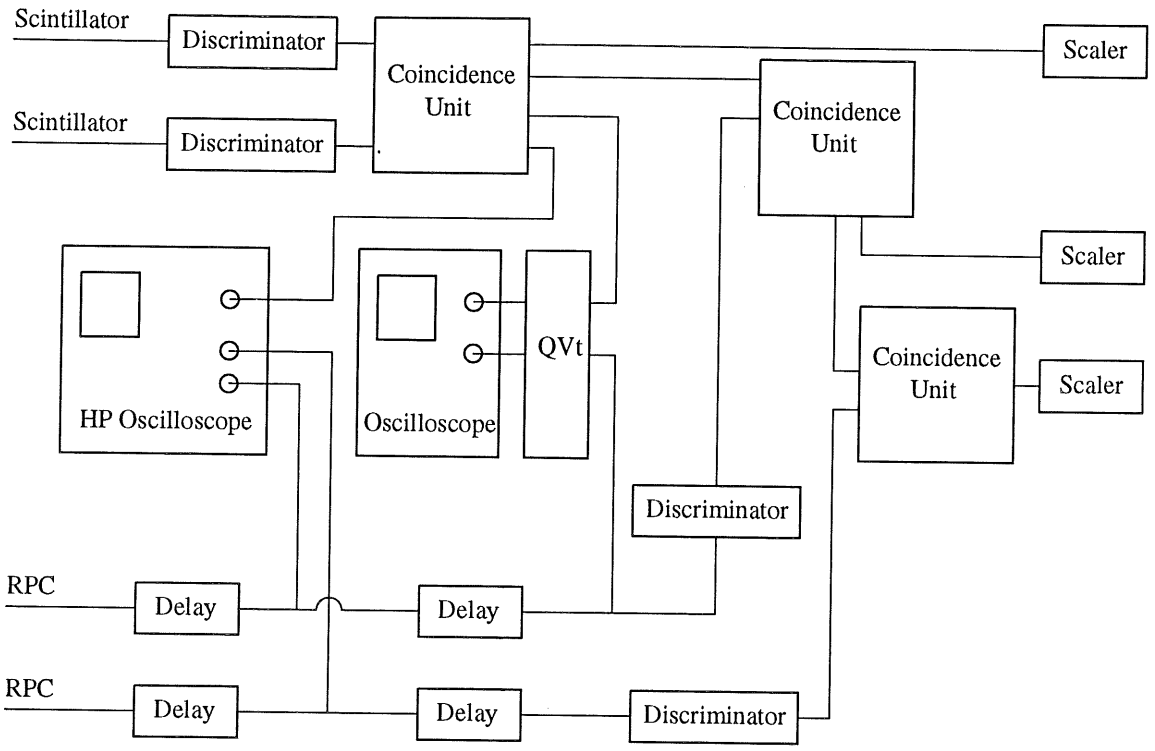


Figure 6.2: Electronic readout system for the RPC.

to a discriminator for conversion to square logic pulses, and then to a coincidence unit which generates output whenever two input signals arrive simultaneously. The coincidence of scintillator signals was counted by a scaler.

The RPC signal was handled in a similar manner. Initially all copper readout strips on the chamber surface were connected together via a resistor chain to form one large readout area. Signals from this area were discriminated, and then the coincidence of RPC signals with scintillator signals was counted via a coincidence unit and scaler: comparison of RPC and scintillator coincidences and just scintillator coincidences indicates the efficiency of operation of the chamber.

Extreme care was necessary in the handling of these signals: when dealing with coincident information, it is vital that the signal timing is preserved, however far it is processed. Delay boxes and delay lines were included in the system to ensure that chamber pulses coincident with scintillator pulses would be recognised as such, despite the different processing routine of these signals.

RPC signals, before discrimination, were also fed to the display channels of a

Hewlett Packard 54510A digitising oscilloscope. Pulse shapes could then be studied with a timebase resolution of $1\,ns$ and a voltage resolution of $10\,mV$. A pulse height analyser (QVt) also received the RPC signal and performed integration over a $80\,ns$ time window (triggered by a scintillator coincidence signal) to measure the charge deposited by the chamber avalanche. The pulse charge distribution was displayed on an additional oscilloscope.

Further studies were performed with the eight copper readout strips of the RPC connected individually to the readout system. An additional coincidence of signals from the two RPC strips was introduced. First two adjacent strips were read out and then the separation of the strips was gradually increased until strips at either edge of the chamber's active area were being read out - the degree of coincidence of individual strip signals has important consequences for the position resolution of the RPC.

### 6.3.3 Experimental Studies

**Pulse shape** The RPC response begins above $40\,kV cm^{-1}$ and the signal shape is shown in figure 6.3: typically a large pulse is followed (or occasionally preceded) by a smaller pulse. This phenomenon is known as "afterpulsing".

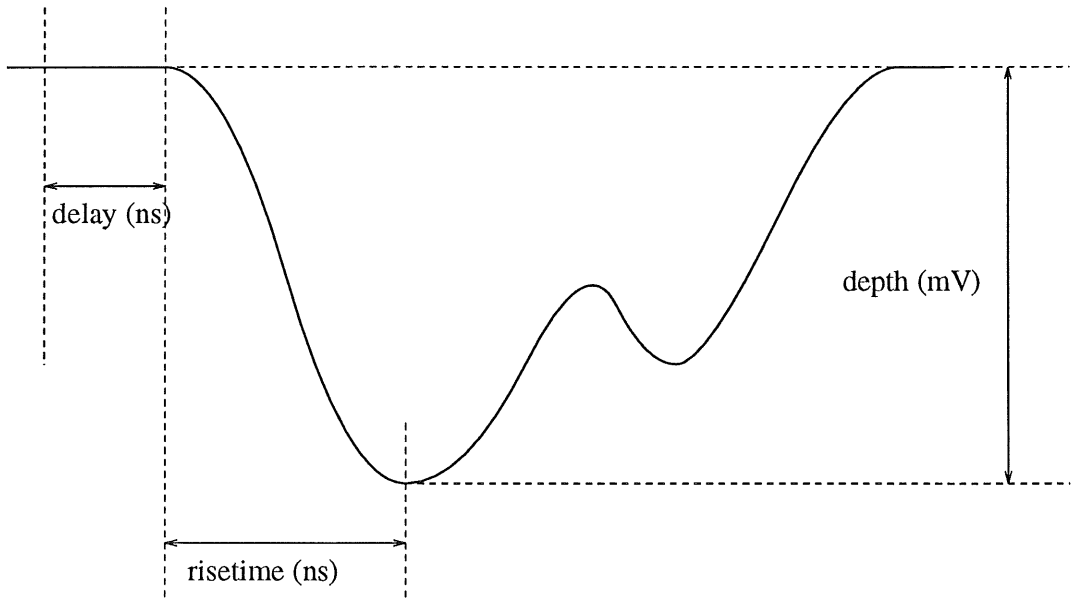


Figure 6.3: Shape of pulse generated by the RPC.

Afterpulsing could be explained by the migration of positive argon ions to the cathode where they draw electrons from the surface. Recombination of argon ions and electrons produces photons that may then induce further electron emission from the cathode, initiating a spurious avalanche in the detector. However, the afterpulse was observed to arrive always within $100\,ns$ of the scintillator coincidence trigger, whereas the mobility of argon ions in the chamber conditions is such that the drift time of the ions across the chamber is of the order of $3\,\mu s$ [46]. Such a mechanism for the afterpulse is then excluded.

In fact, the electron drift time across the chamber is itself of the order of tens of nanoseconds, so a fast generation mechanism for the second avalanche is implied. Photons in the initial avalanche could ionise the surrounding gas to produce a second avalanche, or, again, cause photoemission at the cathode, in which case the afterpulse would be expected to arrive after a certain, constant time interval due to the electron drift time from cathode to anode. The data suggest an approximately constant time delay: figure 6.4 shows a histogram of delay times fitted with a gaussian of mean $\sim 70\,ns$. But unfortunately the limited statistics are inconclusive.

These mechanisms also fail to explain the occasional occurence of a small first pulse followed by a large afterpulse. At this stage, the afterpulsing mechanism was not understood.

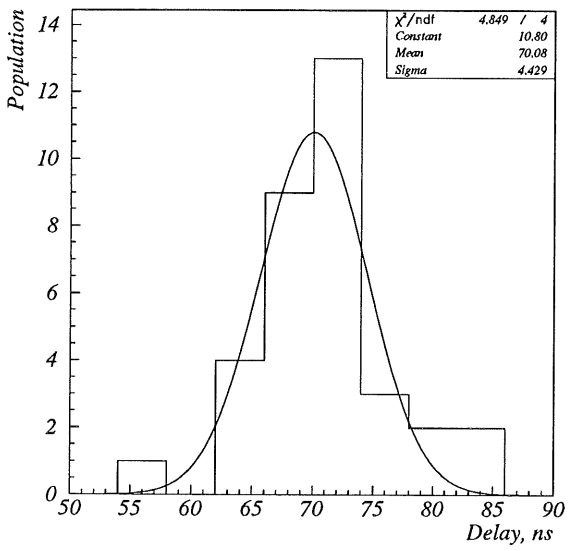


Figure 6.4: Distribution of afterpulse delay times.

**Limited streamer operation** The size of the pulse generated by the RPC was studied as a function of the electric field applied to the chamber: a distinct transition in pulse size is expected as the chamber operation moves from the proportional region to the limited streamer region.

All readout strips were connected together to form a large readout area and thereby increase the count rate of the chamber. The applied electric field strength was varied between $40\,kVcm^{-1}$ and $55\,kVcm^{-1}$, above which signals become distorted. An initial study was performed taking measurements of pulse size by hand from the HP oscilloscope. The results are shown in figure 6.5, and some suggestion of a transition is seen around $44\,kVcm^{-1}$ (*nb.* the measurement error for the pulse voltage was $\pm 10\,mV$ — in the figure, the error bars are smaller than the marker used for each data point).

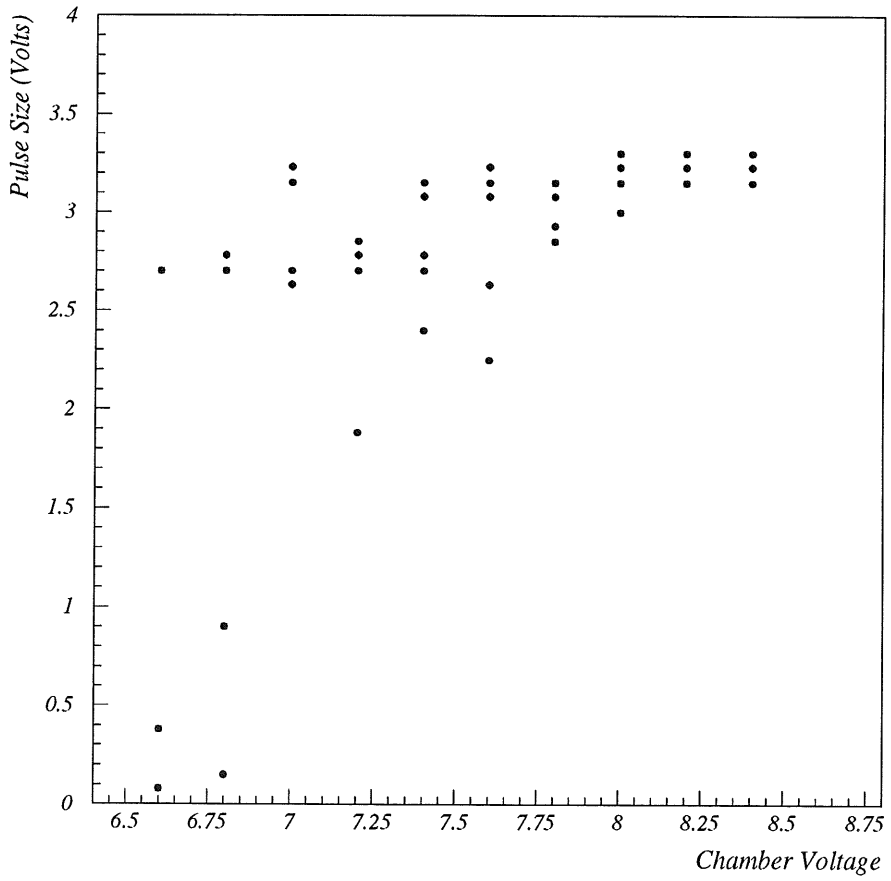


Figure 6.5: Variation of chamber pulse size with applied voltage.

The study was repeated using the QVt analyser to produce a pulse size histogram at each chamber voltage setting with increased statistics. Two populations in the histograms could be seen, one at low charge (small pulse), the other at higher charge (large pulse). However the low charge population was consistent with noise from the chamber. No conclusive evidence of limited streamer operation was observed.

It was concluded that the freon component of the gas mixture was too large, at 9% of the gas volume (compared to a 4% component quoted in the existing literature). As an electromagnetic gas, the excessive freon component may prevent the build-up of electrons and thus of sufficient space charge to initiate a streamer. Further tests of the chamber would be performed with a reduced freon gas fraction.

**Timing of pulses** It was observed that the RPC pulses suffered a variable time delay with respect to the scintillator coincidence signal ("delay" is defined in figure 6.3). In general, pulses with lower gradients (defined as depth divided by risetime – see figure 6.3) suffer greatest delay, often up to $20\,ns$, but the variation will be a problem when timing is required from an RPC trigger.

Risetimes of the chamber signal were observed up to $30\,ns$, again excluding limited streamer operation where the risetimes are expected to be less than $5\,ns$.

**Signal Sharing** When an electron avalanche or streamer reaches the anode plate of the RPC, charge displacement can occur in more than one readout strip to generate the signal. An algorithm would then be applied to find the point of maximum charge displacement and thus the position of the avalanche. The resolution of the detector would be best if this signal sharing could be minimised.

The degree of signal sharing between readout strips was studied via the observed coincidence of signals from individual strips. Initially two adjacent strips were connected to the readout system, and the coincidence rate measured as the chamber voltage was varied. The procedure was then repeated, reading out two non-adjacent strips separated by a single strip, and then gradually increasing the separation until strips at either edge of the chamber active area were being read out.

Signal sharing was observed to decrease as the separation between the strips was increased, but also to increase with increasing chamber voltage: for an applied field of $45\,kVcm^{-1}$, the coincidence rate of signals from adjacent strips was 60%, while for strips with maximum separation (*ie.* at either edge of the active area) the coincidence rate was zero; when the field was increased to $55\,kVcm^{-1}$, the coincidence

rate between adjacent strips rose to 80% and for the most separated strips to 30%.

For position resolution, this study would suggest that the lowest possible operating voltage should be applied to the chamber.

**Efficiency** The efficiency of the RPC for the detection of cosmic muons was tested using the rate of coincidence between RPC and scintillator signals compared to the rate of coincidence between the scintillators alone. The efficiency is good and increases with applied field from, for example, around 80% at $43\,kVcm^{-1}$ to over 90% at $45\,kVcm^{-1}$.

However, high operating voltages have an adverse effect on the pulse shape and position resolution of the chamber, so lower voltages are favourable and the efficiency of the chamber is still suitably high.

**Noise** Intrinsic chamber noise was monitored in the RPC by measuring the current flowing between the graphite layers, across the chamber. This "dark current" was small (of the order of a few microamps) but increased with the voltage applied to the chamber. However, a depletion of the dark current was observed over a five-month period: the variation of dark current with chamber voltage recorded in November 1991 and April 1992 is displayed in figure 6.6.

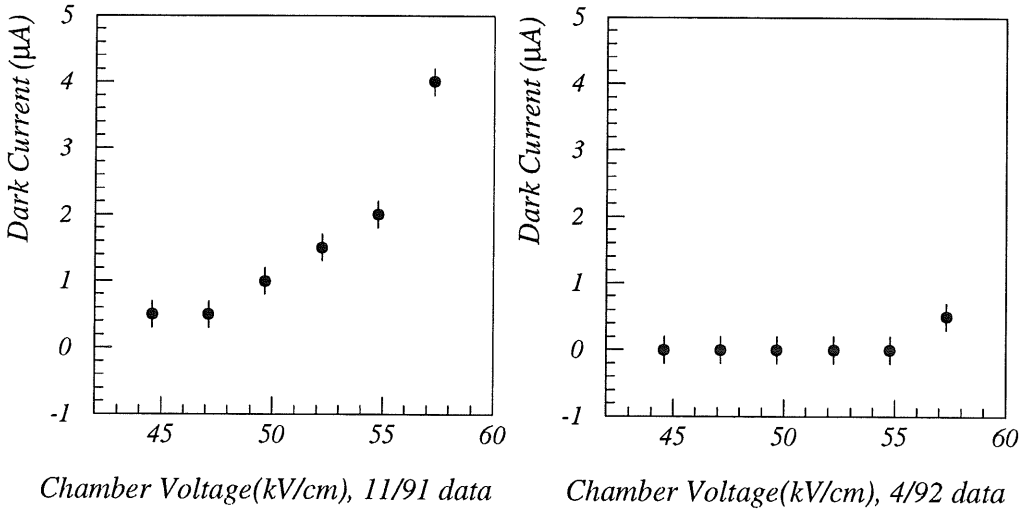


Figure 6.6: Decrease of dark current observed over five-month period.

The dark current may be a consequence of irregularities in the surface of the bakelite plate. The electric field at the surface is then non-uniform - this will affect the resolution of the chamber as electron avalanches will be drawn astray to the points of highest electric field. But if the concentration of field lines is particularly high, electrons could be drawn out of the surface (field emission) and, as they move from cathode to anode, constitute a dark current within the chamber.

After repeated application of electric field over several months, irregularities in the bakelite surface will have been "burned off" and so a depletion in the dark current could be expected, and is indeed seen.

The bakelite surfaces in the RPC should be as smooth as possible at the time of construction to minimise the dark current. Thin coatings, such as linseed oil, could be used to improve the smoothness of the surface.

**Relaxation** A momentary increase in the gas flow out of the chamber was observed as high voltage was applied, suggesting that the resistive plates move together under the influence of the field. A similar "relaxation" effect was seen when the field was removed – an increase in chamber volume as the plates move apart causes a temporary reduction in the gas flow.

Such effects must be considered, especially in the design of larger chambers - the chamber size may be restricted and spacers should be correctly positioned.

## 6.4 Subsequent Development

In the subsequent development of the RPC at Manchester University, limited streamer operation has been achieved with a gas mixture of 58% argon, 38% isobutane and only 4% freon [55]. For streamer pulse delays greater than a few nanoseconds, a small prepulse has been observed, believed to be a proportional pulse, which arrives with constant delay and is therefore more useful for trigger timing than the streamer pulse. It may be preferable to operate the chamber in the proportional region, but as yet its efficiency in this mode is unknown and amplification may be needed for the signal.

# Summary and Conclusion

A method for the statistical classification of events using moments of variable distributions has been applied to some of the physics processes observed at the HERA collider. After initial tests of the routine on known data samples, the separation of the charged current process from the dominant beamgas/cosmic background was attempted. Fits performed in bins across the missing $P_\perp$ distribution had varied success, measured in terms of the $\chi^2$ values achieved. When the results were compared to the distribution of events in missing $P_\perp$ predicted by the Monte Carlo generator for the process, the matrix method did not offer any improvement on results obtained by conventional selection methods of cutting and scanning.

However the efficacy of the matrix technique was severely limited in this study by the lack of statistics available for the description of the event classes, particularly for the background processes. As more data is collected at the HERA experiments and Monte Carlo modelling techniques improve, this classification method may well be used to greater effect for the identification of physics processes, although its success in $e^+e^-$ physics may never be matched.

The initial stages of the development of the Resistive Plate Chamber have also been reported here. A fully-operational chamber with readout system was established and the behaviour of the chamber was studied in the cosmic muon flux. Although limited streamer operation was not achieved in the course of this work, the experience gained paved the way for further development of the chamber into a viable muon trigger for the next generation of physics experiments at the Large Hadron Collider.

# Appendix

## Details of Data Selection

Data passing the four levels of the H1 trigger system is then subject to the "Level 5" classification procedure. This gives a very basic classification of events using simple and well-measured quantities, *eg.* transverse energy measured by the LAC. Events are tagged as candidates for a certain physics process.

Neutral current candidates are selected at Level 5 by the following criteria:

- there is a cluster in the BEMC of energy $> 4\,GeV$ (*ie.* a candidate scattered electron);
- a $z$-vertex can be reconstructed within the volume of the H1 detector;
- and from TOF information, it is known that the event occurred in time with a HERA bunch crossing.

Additional cuts have then been applied to this data, ensuring a clean sample of neutral current events by demanding a more definite electron signature and restricting the $z$-vertex position:

- a $z$-vertex reconstructed within $+35/-25\,cm$ of the nominal interaction point;
- a BEMC cluster of energy $> 10\,GeV$;
- the $x$ or $y$ position of the BEMC cluster further than $14\,cm$ from the beam axis – this excludes a region of triangular BEMC stacks adjacent to the beampipe whose behaviour is not well understood;
- a BPC signal registered within $15\,cm$ of the cluster to exclude events where the BEMC shower is due to a neutral particle, such as a $\pi^0$ or photon;

- the BPC hit also within $60\,cm$ of the beam axis;
- and the scattering angle ($\theta$) of the electron, calculated from the $z$-vertex position and the BPC hit closest to it, $< 173°$.

Diffractive processes can be removed from the neutral current sample by cutting on the rapidity gap characteristic of such events. A diffractive event is identified either by the rapidity gap in the LAC or by the lack of a proton remnant in the forward detectors. Specifically

- the most forward particle in the LAC has a pseudorapidity, $\eta \leq 1.8$; OR
- the energy deposited in the plug calorimeter is $< 1\,GeV$,
- the number of paired hits in the forward muon system is $\leq 1$
- and the number of hits in the proton tagger is zero.

Charged current candidates are selected at Level 5 on the following basis:

- again, the event is in time with a HERA bunch crossing;
- a $z$-vertex is reconstructed;
- missing transverse energy measured in the LAC $> 10\,GeV$;
- and at least one "good" track is reconstructed, either in the forward tracker where a planar segment is required, or in the central tracker where the criteria are:
  - $z$-vertex of the track within $\pm 100\,cm$;
  - the track begins within a $30\,cm$ radius of the beam axis;
  - the track ends at a radius more than $10\,cm$ greater than the radius of the track start;
  - the number of hits seen in the CJC $> 0$;
  - and the track approaches within $5\,cm$ of the reconstructed event vertex.

# References

[1] B.H.Wiik, *HERA Status.*
Proceedings of the HERA Workshop Vol.1, Hamburg Oct. 29-30 1991, p.1, ed. W.Buchmüller, G.Ingelman.

[2] G.Wolf, *HERA Physics.*
DESY Preprint, DESY 94-022, Hamburg (1994).

[3] M.Duren, K.Rith, *Polarised Electron Nucleon Scattering at HERA: the HERMES Experiment.*
Proceedings of the HERA Workshop Vol.1, Hamburg Oct. 29-30 1991, p.427, ed. W.Buchmüller, G.Ingelman.

[4] P.D.B.Collins, A.D.Martin, E.J.Squires, *Particle Physics and Cosmology.*
John Wiley & Sons (1989).

[5] UA1 Collaboration, Phys.Lett.B122(1983) 103 and Phys.Lett.B126 (1983) 398.
UA2 Collaboration, Phys.Lett.B122(1983) 476 and Phys.Lett.B129(1983) 130.

[6] CTEQ Collaboration, *Handbook of Perturbative QCD.*
April 1993.

[7] B.Andersson, G.Gustafson, G.Ingelman, T.Sjöstrand, Phys.Rep.97(1993) 31.

[8] EMC Collaboration, Nucl.Phys.B259(1985) 189.
EMC Collaboration, Nucl.Phys.B293(1987) 740.

[9] BCDMS Collaboration, Phys.Lett.B223(1989) 485.
BCDMS Collaboration, Phys.Lett.B237(1990) 592.

[10] H1 Collaboration, Phys.Lett.B297(1992) 205.

[11] H1 Collaboration, Phys.Lett.B299(1993) 374.

[12] H1 Collaboration, Nucl.Phys.B407(1993) 515.

[13] H1 Collaboration, Phys.Lett.B321(1993) 161.

[14] L.Jönsson, H.Küster, M.Nyberg-Werther, J.Stier, *A Measurement of the Gluon Density in the Proton at Low x.*
H1 Note (in preparation), DESY, Hamburg.

[15] T.Greenshaw, M.Hapke, R.Prosi, K.Müller, *New Results from the H1 Experiment at HERA on Jets, the Proton Structure Function, Rapidity Gap Events, Charged Current Cross-section and Searches for New Particles.*
DESY Preprint, DESY 94-112, Hamburg (1994).

[16] H1 Collaboration, Nucl.Phys.B396(1993) 3-23.

[17] ZEUS Collaboration, *Observation of events with a large rapidity gap in deep inelastic scattering at HERA.*
Phys.Lett.B315 (1993) 481-493.

[18] H1 Collaboration, *Deep inelastic scattering events with a large rapidity gap at HERA.*
To be submitted to Nucl.Phys.B.

[19] D.Haidt, H.Pietschmann, *Electroweak Interactions*
Landolt-Boernstein. New Series. 1/10 p.212, Springer (1988).

[20] H1 Collaboration, Phys.Lett.B324 (1994) 241.

[21] H1 Collaboration, *The H1 Detector at HERA.*
DESY Preprint, DESY 93-103, Hamburg (1993). Submitted to Nucl. Inst. & Meth.

[22] R.Fernow, *Introduction to Experimental Particle Physics.*
Cambridge University Press (1986).

[23] M.Aguilar-Benitez et al., *Review of Particle Properties.*
Phys. Rev. D45 (1992).

[24] H1 Calorimeter Group, *Results from Pion Calibration Runs for the H1 Liquid Argon Calorimeter and Comparisons with Simulations.*
DESY Preprint, DESY 93-047, Hamburg (1993).

[25] V.Shekelyan, *Simulation and Reconstruction in H1 Liquid Argon Calorimetry.*
H1 Note, H1-04/93-288, DESY, Hamburg (1993).

[26] M.Goldberg, *Energy Calibration and Resolution in BEMC.*
H1 Note, H1-05/93-292, DESY, Hamburg (1993).

[27] A.Mehta, *private communication.*

[28] R.Barlow, *Statistics.*
John Wiley & Sons (1989).

[29] R.Marshall, *The Classification of Events via Analysis of Means, Variance and Higher Moments.*
Submitted to Zeit.f.Phys.C.

[30] G.Grindhammer, *Monte Carlo Generators for ep Physics.*
Proceedings of the HERA Workshop Vol.3, Hamburg Oct. 29-30 1991, p.1153, ed. W.Buchmüller, G.Ingelman.

[31] J.Meyer (Ed.), *Guide to Simulation program H1SIM.*
DESY IBM, HERA01.H1SIM.GUIDE (1991).

[32] G.Ingelman, *LEPTO 6.1 - The Lund Monte Carlo for Deep Inelastic Lepton-Nucleon Scattering.*
Proceedings of the HERA Workshop Vol.3, Hamburg Oct. 29-30 1991, p.1366, ed. W.Buchmüller, G.Ingelman.

[33] T.Sjöstrand, *PYTHIA 5.7 and JETSET 7.4 Physics and Manual.*
CERN Preprint, CERN-TH.7112/93, Geneva (1993).

[34] L.Lönnblad, Comp.Phys.Comm.71(1992) 15.

[35] G.A.Schuler, H.Spiesberger, *DJANGO 1.0 The interface for the event generators HERACLES and LEPTO.*
Proceedings of the HERA Workshop Vol.3, Hamburg Oct. 29-30 1991, p.1419, ed. W.Buchmüller, G.Ingelman.

[36] A.Kwiatkowski, H.Spiesberger, H.-J.Möhring, *HERACLES 4.1 An event generator for ep interactions at HERA including radiative processes.*
Proceedings of the HERA Workshop Vol.3, Hamburg Oct. 29-30 1991, p.1294, ed. W.Buchmüller, G.Ingelman.

[37] H1 Collaboration, *Energy Flow and Charged Particle Spectra in Deep Inelastic Scattering at HERA.*
DESY Preprint, DESY 94-033, Hamburg (1994). Submitted to Zeit.f.Phys.C.

[38] A.D.Martin, W.J.Stirling, R.G.Roberts, Phys.Rev.D47(1993) 867.

[39] A.D.Martin, W.J.Stirling, R.G.Roberts, *Parton Distributions of the Proton.* RAL Preprint, RAL-94-055, Rutherford (1994).

[40] CERN Program Library, *CERNLIB.* CERN, Geneva (May 1993).

[41] M.Hapke, *Messung des Wirkungsquerschnittes geladener Ströme in tiefinelastischer Elektron Proton Streuung.* DESY Report, DESY FH1K-94-05, Hamburg(1994).

[42] V.Hedberg, G.Ingelman, C.Jacobsson, L.Jönsson, *Asymmetries in Jet Azimuthal Angle Distributions as a Test of QCD.* Proceedings of the HERA Workshop Vol.1, Hamburg Oct. 29-30 1991, p.331, ed. W.Buchmüller, G.Ingelman.

[43] CDF Collaboration, *Evidence for Top Quark Production in $p\overline{p}$ Collisions at $\sqrt{s} = 1.8 TeV$.* Fermilab Preprint, FERMILAB-PUB-94/097-E, Batavia (1994).

[44] CMS Collaboration, *Letter of Intent for a General Purpose Detector at the LHC.* CERN Preprint, CERN/LHCC/92-3, Geneva (1992).

[45] ATLAS Collaboration, *Letter of Intent for a General Purpose pp Experiment at the Large Hadron Collider at CERN.* CERN Preprint, CERN/LHCC/92-4, Geneva (1992).

[46] F.Sauli, *Principles of Operation of Multiwire Proportional and Drift Chambers.* CERN Preprint, CERN 77-09, Geneva (1977).

[47] I.Crotty et al., *Further Studies of Avalanche Mode Operation of Resistive Parallel Plate Chambers.* CERN Preprint, CERN/LAA-MC(draft), submitted to Nucl. Inst. & Meth.

[48] M.Atac, A.V.Tollestrup, D.Potter, *Self-quenching Streamers.* Nucl. Inst. & Meth. 200 (1982) 345-354.

[49] R.Santonico, R.Cardarelli, *Development of Resistive Plate Counters.* Nucl. Inst. & Meth. 187 (1981) 377-380.

[50] R.Cardarelli et al., *Progress in Resistive Plate Counters.*
Nucl. Inst. & Meth. A263 (1988) 20.

[51] M.Bertino et al., *Performance of Resistive Plate Counters at Beam Flux up to* $140 Hz cm^{-2}$.
Nucl. Inst. & Meth. A283 (1989) 654-657.

[52] F.Grancagnolo, *The RPC as a Muon Detector: The E771 Experience.*
SSC Detector Conference, Dallas, October 1990.

[53] A.Böhrer et al., *Status Report of the RD5 Experiment.*
CERN Preprint, CERN/DRDC/91-53, Geneva (1992).

[54] A.E.Wright, *Report on the Development of the Resistive Plate Chamber.*
University of Manchester (1992).

[55] I.Duerdoth et al., *The transition from proportional to streamer mode in a resistive plate chamber.*
Nucl. Inst. & Meth. A348 (1994) 303-306.

# Acknowledgements

Thanks to...

Chris Hilton, Phill Biddulph, Andrew Mehta, Roland Martin, Lynn Johnson, Julian Phillips, Christoph Hoeger and Professor John Dainton;

Achim Braemer, Joachim Stier, Michael Hapke and lots of other nice, friendly, approachable DESY folk;

back in Manchester: Ian Duerdoth, Ray Thompson and Dave Mercer;

and to Professor Robin Marshall, my supervisor and the SERC/PPARC for funding my studies.

Thanks also to...

absolutely everybody in Manchester and Hamburg whose friendship and support I have enjoyed: particularly, Alison Snell, Julie Eckersley, Alison Hammond, Louise Hammond, Ania Davidson, Paul Newman, Andrew Mehta and Lizz Tonks (who deserves a *very* particular mention).

And finally thanks to...

Jonathan Wilson, who was there for quite a while; and the two people who are always there: Gwen and Bill Wright, my mum and dad.